



**POLARIMETRIC CALIBRATION AND CHARACTERIZATION OF THE  
TELOPS FIELD PORTABLE POLARIMETRIC-HYPERSPECTRAL IMAGER  
IN THE LONG WAVE INFRARED**

**THESIS**

**Joel G. Holder, Captain, USAF**

**AFIT-ENP-14-M-14**

**DEPARTMENT OF THE AIR FORCE  
AIR UNIVERSITY**

***AIR FORCE INSTITUTE OF TECHNOLOGY***

---

**Wright-Patterson Air Force Base, Ohio**

**DISTRIBUTION STATEMENT A.  
APPROVED FOR PUBLIC RELEASE; DISTRIBUTION UNLIMITED**

The views expressed in this thesis are those of the author and do not reflect the official policy or position of the United States Air Force, Department of Defense, or the United States Government. This material is declared a work of the U.S. Government and is not subject to copyright protection in the United States.

AFIT-ENP-14-M-14

**POLARIMETRIC CALIBRATION AND CHARACTERIZATION OF THE  
TELOPS FIELD PORTABLE POLARIMETRIC-HYPERSPECTRAL IMAGER  
IN THE LONG WAVE INFRARED**

THESIS

Presented to the Faculty

Department of Engineering Physics

Graduate School of Engineering and Management

Air Force Institute of Technology

Air University

Air Education and Training Command

In Partial Fulfillment of the Requirements for the

Degree of Master of Science in Applied Physics

Joel G. Holder, MS

Captain, USAF

March 2014

DISTRIBUTION STATEMENT A.  
APPROVED FOR PUBLIC RELEASE; DISTRIBUTION UNLIMITED

**POLARIMETRIC CALIBRATION AND CHARACTERIZATION OF THE  
TELOPS FIELD PORTABLE POLARIMETRIC-HYPERSPECTRAL IMAGER  
IN THE LONG WAVE INFRARED**

Joel G. Holder, MS  
Captain, USAF

Approved:

//signed//  
\_\_\_\_\_  
Dr. Kevin Gross (Chair)

04-Mar-2014  
Date

//signed//  
\_\_\_\_\_  
Dr. Michael Hawks (Member)

04-Mar-2014  
Date

//signed//  
\_\_\_\_\_  
Dr. Michael Marciniak (Member)

04-Mar-2014  
Date

## **Abstract**

Polarimetric-hyperspectral remote sensing is a promising field that brings two traditionally independent modalities together to enhance scene characterization capabilities. The Telops polarimetric-hyperspectral imager (P-HSI) combines these technologies and provides a combined imaging and spectral capability that is considered state-of-the art. The Defense Threat Reduction Agency (DTRA) funded research at AFIT to leverage this capability to better inform radiation transport models that will allow for more effective location of ionizing radiation sources within the scene.

The desire for highly accurate data requires careful calibration of the instrument. This thesis develops a mathematical calibration framework that links standard Fourier transform spectrometer (FTS) calibration with standard polarimetric calibration in a simple, straightforward manner. Building this framework was key for two reasons. First, it was essential for ensuring the calibration methodology was sound and it provided a framework for understanding the influence of various instrument parameters (both ideal and non-ideal) on ultimate calibration performance. Second, this development makes it easy for both FTS and polarimetric experts to understand, and paves the way for use of this method for similar instruments in the future.

This framework is then utilized to quantify the non-idealities of the system and to characterize the performance of the spectro-polarimetric calibration. The calibration was first performed under the assumption of an ideal polarizer, and then an additional correction was made for the non-ideal nature of the polarizer. The results showed that the

calibration was accurate to within 1.18% and accounting for the non-ideal nature of the polarizer provided an additional 0.56% correction in the measured degree of linear polarization (DoLP). It was determined that the residual error in the measured DoLP was primarily due to a bias in the data caused by the thermal instability of one of the blackbody sources and not because of the calibration itself. Other sources of residual error included noise, detector non-linearity, and other experimental setup limitations. The band-averaged noise equivalent spectral DoLP (NESDoLP) was determined to be 0.39% at  $16\text{ cm}^{-1}$  resolution with a  $200\text{ }\mu\text{s}$  integration time and flood illumination from a  $55\text{ }^{\circ}\text{C}$  blackbody. This represents the limit in the accuracy of the calibration that should be achieved after the bias is removed. The band-averaged noise equivalent spectral radiance (NESR) values were  $30.6\text{ nW}/(\text{cm}^2\text{ sr cm}^{-1})$ ,  $33.6\text{ nW}/(\text{cm}^2\text{ sr cm}^{-1})$ ,  $33.6\text{ nW}/(\text{cm}^2\text{ sr cm}^{-1})$ , and  $36.9\text{ nW}/(\text{cm}^2\text{ sr cm}^{-1})$  for the  $0^{\circ}$ ,  $45^{\circ}$ ,  $135^{\circ}$ , and  $90^{\circ}$  polarizer measurements respectively. This represents the limit in the accuracy of the radiometric calibration. The diattenuation of the hyperspectral imaging system, excluding the polarizer, was determined to be 0.43 which corresponds to an extinction ratio of 2.51. This is small compared with the polarizer's extinction ratio of 400; however, it must be calibrated out to achieve the most accurate data from the instrument. This thesis demonstrated the capability to perform radiometric, spectral, and polarimetric calibration in order to achieve highly accurate data from the Telops instrument. This will enable more accurate scene characterization, which will better inform the radiation models developed under DTRA sponsorship.

## **Acknowledgments**

I would like to express my sincere appreciation to my faculty advisor, Dr. Kevin Gross, for his guidance and support throughout the course of this thesis effort. The insight and experience was certainly appreciated. I would also like to thank the P-HSI research group, namely, Jake Martin, Peter Borton, Seth Swift, and Jeremy Pitz for the full gamut of support they supplied throughout the effort as well as my committee members Dr. Mike Hawks and Dr. Mike Marciniak. Most importantly, I would like to thank my wife for her steadfast support and tolerance during this demanding program.

Joel G. Holder

## Table of Contents

	Page
Abstract .....	iv
Acknowledgments.....	vi
Table of Contents .....	vii
List of Figures .....	ix
List of Tables .....	xiv
 I. Introduction .....	 1
Overview .....	1
Organization of Thesis .....	2
Benefits of Study.....	3
 II. Background and Theory .....	 6
Introduction to Hyperspectral Imaging .....	6
Fourier Transform Spectrometer.....	8
Polarimetric Imaging in the LWIR .....	14
<i>Introduction</i> .....	14
<i>Stokes Vector Representation of Polarized Light</i> .....	15
<i>Mueller Matrix Representation</i> .....	19
Instrumentation .....	20
Previous Work Related to Spectro-Polarimetric Performance and Calibration .....	23
 III. Standard HSI Calibration .....	 27
FPA Non-uniformity and Radiometric Calibration.....	27
Off-Axis Spectral Calibration .....	34
 IV. Polarimetric-HSI Calibration.....	 45
Polarimetric System Model.....	46
Polarimetric Calibration under the Ideal Polarizer Assumption .....	51
Polarimetric Calibration Without the Ideal Polarizer Assumption .....	53
<i>Methodology Overview</i> .....	54
<i>Experimental Setup</i> .....	58



Analysis of Results.....	68
<i>Evaluation of System Matrices</i> .....	68
<i>Calibration Verification on an Unpolarized Source</i> .....	77
<i>Calibration Verification on Polarized Sources</i> .....	80
<i>Noise and Error Analysis</i> .....	89
NESR and NESDoLP of an Unpolarized Source.....	92
NESR and NESDoLP of a Polarized Source .....	98
V. Polarimetric Performance Modeling .....	101
<i>Simulation of Polarimetric Performance with non-ideal Polarizer</i> .....	103
<i>Determination of the HSI System Diattenuation</i> .....	110
VI. Conclusions.....	113
Future Recommendations .....	117
References .....	120

## List of Figures

	Page
Figure 1. Flow chart outlining some of the benefits of each technology and the enhanced capability enabled by the combination of the technologies.....	5
Figure 2. Illustration of the hyperspectral imaging data cube. Each layer represents a picture of the scene for a given spectral band. For a typical color image this would contain three layers, one for red, green, and blue. For a hyperspectral image, this contains hundreds of layers. Each pixel contains a spectrum that can be used to identify the material present in the pixel. (Image adapted with permission from Ref [1])......	7
Figure 3. Typical FTS layout. Light enters the system from the scene on the right and then is split by the beam splitter. Each path then is reflected back to the beam splitter off of the retro reflectors and therefore recombined before hitting the detector. As one of the mirrors moves the phase difference between the recombined light causes an interference pattern called an interferogram. ....	10
Figure 4. The picture on the left is the frequency spectrum of the incoming light showing two different wavelengths. On the right is the interferogram produced by this bi-chromatic light. The higher frequency lower intensity wave is added to the lower frequency higher intensity wave to produce the resultant interferogram which is a superposition of the two individual waves. ....	10
Figure 5. A broad-band interferogram generated by the Telops Hypercam. ....	11
Figure 6. Normalized Stokes vectors used to represent the polarization state of light. ....	17
Figure 7. The Telops P-HSI system. The picture on the bottom-middle shows the interferometer module and the picture on the bottom-right shows the polarization module. (Image courtesy of Telops, Inc.). ....	22
Figure 8. The complex raw spectrum (top), complex gain (middle), and complex offset (bottom) for the data collection. ....	30
Figure 9. Visible imagery taken of the scene with a camera mounted on top of the Telops. The blue box roughly outlines the area of the scene collected by the infrared camera in the FTIR. ....	31
Figure 10. On the right, a raw band-averaged interferogram image is shown along with an interferogram from a random pixel. On the left a band-averaged image is shown after having been converted from raw interferograms to raw spectra. The raw spectrum from a pixel is shown on the bottom. ....	32
Figure 11. Calibrated band-averaged radiance image (left) and a spectrum (right) for one pixel looking at the sky above the building. Several water absorption features are coarsely resolved as well as the ozone feature at $1043\text{ cm}^{-1}$ .....	33

Figure 12. Calibrated and processed band-averaged image of the scene. The bad pixels have been removed, the image has been oriented properly, and a more natural color map is used. ....	33
Figure 13. Imagery of the same scene with a $0.5 \text{ cm}^{-1}$ spectra resolution. Shows the results of an end member analysis that utilizes the k-means algorithm with correlation as the distance parameter. The top right image groups the end-members by color and the bottom plot shows the spectrum of each end-member on a brightness temperature scale. The concentric rings are a result of off-axis spectral scaling which has not been compensated for in post processing. ....	38
Figure 14. Setup for generating known spectral features in the LWIR for use during off-axis spectral calibration.....	39
Figure 15. Polystyrene spectra of several pixels at varying locations on the FPA before the off-axis spectral correction is applied. The zoomed in box shows that the spectral features do not perfectly line up for each pixel. ...	40
Figure 16. Polystyrene spectra of several pixels at varying locations on the FPA after the off-axis spectral correction is applied. The zoomed in box shows that the spectral features now align almost perfectly along the spectral axis. ....	41
Figure 17. Results of the end member analysis after the spectral axis scaling has been corrected. Now, all spectral features line up correctly and there are no concentric rings due to off-axis scaling. What is visible, is the fringe pattern created by the interferometer itself. This is an artifact of forcing 10 end members when there are only four true end-members. The light and dark rings are separated by a temperature difference of less than 0.5 K which is close to the NEDT of the instrument. ....	43
Figure 18. End member analysis before spectral axis correction using five end members. The concentric rings are still visible in the sky region and the road is incorrectly grouped together with another end-member. ....	44
Figure 19. End member analysis after spectral axis correction using five end-members. The sky is now appropriately grouped by altitude and the road is properly identified as its own end member. ....	44
Figure 20. Simplified P-HSI system where an input Stokes vector from the scene travels through the system getting modified by each optical component in the system. After passing through the system, a Stokes vector reaches the detector which is a function of the system Mueller matrix and the instrument offset Stokes vector. ....	47
Figure 21. Experimental setup showing blackbody radiation passing through a linear polarizer and reaching the Telops Hypercam. Illustrates the self-emitted and reflected components that also reach the instrument making it difficult to determine the transmitted component.....	54
Figure 22. Experimental setup used for polarimetric calibration. Two different target source temperatures are used for differencing and the reference source is placed at the specular angle and kept at a constant temperature. ....	55

Figure 23.	Band-averaged image of the polarizer with the 65 °C blackbody in the background. Note the active area of the blackbody overfills the polarizer but not the entire rotation stage. The baffle can be seen on the left side of the image. ....	61
Figure 24.	Data collected from the external polarizer as it was rotated through 180°. The angle of the external polarizer at which maximum signal was received corresponds to the best alignment between the external and internal polarizer. The solid line is the best fit $\cos^2$ curve. ....	61
Figure 25.	Stokes images of the scene with the target blackbody at 65 °C. The background scene is visible in the $s_0$ Stokes image, whereas it is not visible in the $s_1$ and $s_2$ Stokes images indicating that there was very little thermal drift in the scene during the collection. ....	62
Figure 26.	$s_0$ image after differencing the hot and cold data. The dark background scene indicates that the thermal drift between collection of the hot and cold data was small. ....	63
Figure 27.	Visualization of the channel matrix where each column is a channel vector corresponding to an input Stokes vector. ....	64
Figure 28.	Circular mask to remove all scene data other than the circular region within the polarizer. ....	64
Figure 29.	Images showing the effect on the Stokes elements and DoLP of differencing the high and low temperature data sets. The external and internal polarizers are aligned horizontally which should result in a value of $s_1$ close to one and $s_2$ close to zero with a DoLP close to 100%. In the differenced data this is true whereas in the undifferenced data this is far from true due to the reflected and emitted components. ....	67
Figure 30.	Spectral plots of the system matrix elements for each of the four pixels discussed above. The elements of $W$ for each individual pixel are spectrally flat other than the random noise seen in the plots. The lines are color coded as a visual aid. Blue lines correspond to elements with a value near one, black lines are near zero, and red lines are near negative one. ....	75
Figure 31.	Spectral plot of the system matrix, $W$ , after spatial averaging. The standard deviation is represented with the shaded bands around measured values. Since this is a spatial average, the noise is reduced considerably. The scale on this plot is zoomed in to allow better visualization of the noise in the measurements. ....	76
Figure 32.	Each element of the band-averaged Mueller deviation matrix is plotted for each pixel. The diagonal elements are all close to one and the off-diagonal elements are all close to zero as expected. The checkerboard pattern in the off-diagonal elements is believed to be due to non-linear effects in the read out integrated circuitry (ROIC) and represents a current limit on data accuracy. ....	77

Figure 33.	Histogram of $s_1$ and $s_2$ Stokes elements for 200 measurements of blackbody radiation. The histograms are fitted with a normal distribution curve. In the ideal case, the mean of $s_1$ and $s_2$ would be zero. This shows that there is a small bias in the measurements, possibly to unstable blackbody sources or the non-linearity of the detector.....	79
Figure 34.	Temperature stability of the 6-inch blackbody over a period of just more than 6 minutes. This verifies that the temperature is oscillating approximately 0.5 °C with a period of less than 1.5 minutes. ....	80
Figure 35.	Comparison of the measures Stokes values for the corrected and uncorrected data for a.) $s_1$ and b.) $s_2$ . The solid line is the input Stokes values with a shaded band representing the uncertainty in the external polarizer orientation. ....	82
Figure 36.	Shows the spectral nature of each of the 12 measurements for a single pixel (left) and for 317 spatially averaged pixels (right). The top plots are $s_1$ and the bottom plots are $s_2$ . ....	83
Figure 37.	a.) Error between the measured data and the input data both before and after correction at the 12 calibration points. b.) Error for the data collected in-between the calibration points.....	85
Figure 38.	Error of the measured data for an individual pixel at a.) near the center of the bandwidth and b.) near the edge of the bandwidth where detector sensitivity is slightly decreased.....	87
Figure 39.	Shows the measured spectral error for one pixel for a.) $s_1$ and b.) $s_2$ for each of the 12 input Stokes vectors. The label to the right of each plot indicates the orientation of the external polarizer. ....	88
Figure 40.	Shows the measured spectral error of 317 spatially averaged pixels for a.) $s_1$ and b.) $s_2$ for each of the 12 input Stokes vectors. The label to the right of each plot indicates the orientation of the external polarizer. ....	89
Figure 41.	Spectrally resolved noise of the $s_1$ and $s_2$ measurements when viewing horizontally polarized light. The noise was determined by taking the standard deviation of the mean for the 64 frames acquired at each band.....	92
Figure 42.	Measured NESR of the Telops instrument at each polarizer angle.....	93
Figure 43.	Measured radiance when viewing an unpolarized blackbody source at each instrument polarizer angle after calibration.....	94
Figure 44.	Noise equivalent spectral DoLP of the Telops instrument. ....	97
Figure 45.	DoLP and NESDoLP plotted together. The DoLP error is approximately 0.12% larger than predicted by the NESDoLP. ....	98
Figure 46.	Measured NESR for horizontally polarized light at each instrument polarizer angle.....	99
Figure 47.	Measured radiance at each instrument polarizer angle for a horizontally polarized source. ....	100

Figure 48.	Measured DoLP before and after correction for horizontally polarized light. This time the correction improves the measurement by 0.56% on average. ....	100
Figure 49.	a.) Simulation of the measured $s_{1m}$ Stokes value when horizontally polarized light is incident on the system and $m'_{01}$ is allowed to range from -1 to 1. b.) Simulation of the measured $s_{2m}$ Stokes values when $m'_{01}$ and $m'_{02}$ are allowed to range from -0.7 to 0.7. The extinction ratio of the instrument polarizer is set to 400. ....	106
Figure 50.	Same simulation for a.) $s_{1m}$ and b.) $s_{2m}$ as in Figure 49, except using the Modified Pickering method for calculation of the measured $s_{1m}$ and $s_{2m}$ . Notice that the value of the measured $s_1$ can possibly exceed one using this method. ....	107
Figure 51.	Measured value of $s_{1m}$ when the input Stokes values are allowed to range from 0 to 1 for a.) $m_{01}$ and $m_{02}$ equal to 0.05 and b.) $m_{01}$ and $m_{02}$ equal to 0.5.....	108
Figure 52.	Shows the dependence of the measured $s_{1m}$ values on the extinction ratio of the instrument polarizer. The values of $q$ and $r$ are allowed to vary from 0 to 1. The input Stokes parameters are $s_1 = 1$ and $s_2 = 0$ and $m_{01}$ and $m_{01}$ are both equal to 0.05.....	109
Figure 53.	The measured values of $s_{1m}$ and $s_{2m}$ for the 12 input Stokes vectors are plotted with circles and the calculated values for $s_{1m}$ and $s_{2m}$ are plotted with squares. The input curve is plotted as a dashed line. ....	112

## List of Tables

	Page
Table 1. Telops P-HSI system parameters .....	22
Table 2. Experimental Setup Parameters .....	59

# **Polarimetric Calibration and Characterization of the Telops Field Portable Polarimetric-Hyperspectral Imager in the Long Wave Infrared**

## **I. Introduction**

### **Overview**

Polarimetric-hyperspectral remote sensing is a promising field that brings two traditionally independent modalities together to enhance scene characterization capabilities. The Telops polarimetric-hyperspectral imager (P-HSI) combines these technologies and provides a combined imaging and spectral capability that is considered state-of-the art. The Defense Threat Reduction Agency (DTRA) funded research at AFIT to leverage this scene characterization capability to provide better information to radiation transport models that will allow for more effective location of radiation sources within a region of interest. As a baseline, the models require as much information about the region of interest as possible, including the materials in the scene and the orientation of objects within the scene. Combining the hyperspectral and spectro-polarimetric data sets in a system with high spatial and spectral resolution provides a more robust scene characterization capability that will be utilized in the radiation models.

To support the objectives of the DTRA effort, there is a requirement for highly accurate radiometric, polarimetric, and spectral data on a pixel-by-pixel basis. The complex nature of the Telops instrument combined with working in the thermal IR waveband makes achieving this accuracy a challenge. Because of this, great care must be taken to develop a sound calibration methodology. This thesis develops and



demonstrates the ability to perform calibration in all three domains. That is, radiometric calibration, off-axis spectral calibration, and polarimetric calibration are now successfully implemented. This means that highly accurate radiometric, spectral, and polarimetric data can be generated with the Telops instrument. This will enable more accurate scene characterization, which will better inform the radiation models developed under DTRA sponsorship.

Additionally, this thesis develops a mathematical calibration framework that links standard Fourier transform spectrometer (FTS) calibration with standard polarimetric calibration in a simple, straightforward manner. Building this framework was key for two reasons. First, it was essential for ensuring the calibration methodology was sound and it provided a framework for understanding the influence of various instrument parameters (both ideal and non-ideal) on ultimate calibration performance. Second, this development makes it easy for both FTS and polarimetric experts to understand, and paves the way for use of this method for similar instruments in the future.

## **Organization of Thesis**

Chapter II of this thesis starts off by providing an overview of the basic theory and concepts required to understand the technology that comprises the Telops instrument as well as the methodology described in later chapters. Next, Chapter III covers in some detail the radiometric calibration and off-axis spectral calibration that are required whether the polarizer is there or not, and provides results which demonstrate the effect that these calibrations have on the quality of the data. This chapter is a useful primer for the full spectro-polarimetric calibration that is developed in Chapter IV. Chapter IV is

considered the primary chapter of this thesis. It develops the full spectro-polarimetric calibration of the instrument, providing a mathematical framework that outlines the calibration methodology. This methodology is then used to quantify the non-idealities of the system and to characterize the performance of the spectro-polarimetric calibration on experimental data. Additionally, the noise equivalent spectral radiance (NESR) and noise equivalent spectral degree of linear polarization (NESDoLP) are determined for the dataset, which indicates the fundamental limit of performance achieved with the system. In Chapter V, the polarimetric system model is then used to simulate the effect that changing various system parameters has on the measured data and is used to estimate the diattenuation and extinction ratio of the hyperspectral imager itself (not including the polarizer). Finally, Chapter V provides the conclusions and future recommendations. These recommendations provide useful ways to improve the accuracy of the calibration.

### **Benefits of Study**

Beyond the benefits mentioned above, this research provides broad benefits to the Department of Defense (DoD) and intelligence community (IC) in general. Figure 1 outlines some of the benefits of each technology. Target detection/material identification, anomaly detection, change detection, and buried improvised explosive device (IED) detection are all capabilities of high interest to the DoD and IC. Furthermore, the ability to do so in day or night when the target is camouflaged or hidden within a natural background and potentially occupying very few pixels within the scene is a high priority. Hyperspectral, polarimetric, and long-wave infrared (LWIR) imaging all provide a unique capability to discriminate a target from background scenery.

Hyperspectral imaging is useful for characterization of materials within the scene. This allows the possibility of discriminating a target based on its spectral characteristics.

Polarimetric imaging is useful for detecting manmade objects in a natural background since manmade objects tend to have different polarimetric characteristics than natural objects. It has also been shown to provide a capability for disturbed earth detection and therefore buried mine/IED detection. LWIR imaging is useful for detecting objects in both day and night that are uncharacteristically warm or cool with respect to the surrounding environment whether the object is concealed/camouflaged or not. The combination of these technologies provides an enhanced dataset that contains the traditional hyperspectral signatures as well as spectrally resolved polarimetric signatures. This combination enables a more robust knowledge of the complex index of refraction, which is a fundamental material property that governs light propagation, reflection, and absorption within the material. This results in an improved ability to characterize the scene and provide the capabilities listed in Figure 1.

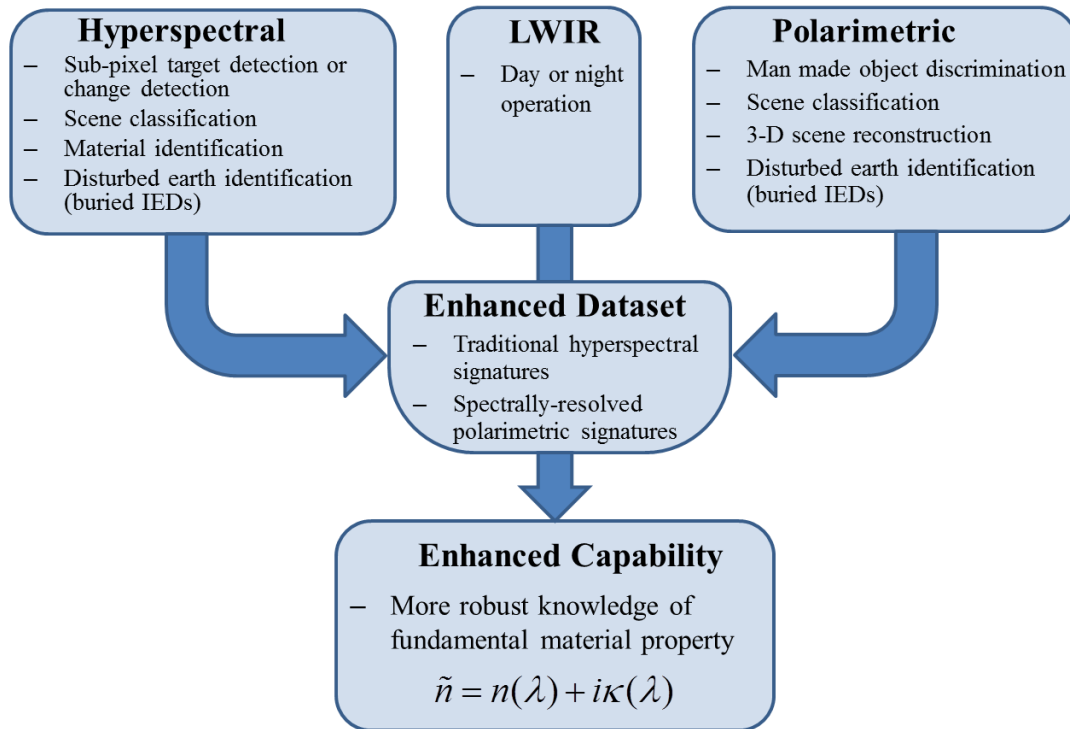


**Figure 1. Flow chart outlining some of the benefits of each technology and the enhanced capability enabled by the combination of the technologies.**

## **II. Background and Theory**

In order to understand how the P-HSI instrument works, it is useful to understand how each component technology works. This section is a review of the basic concepts associated with each major technology used in the Telops imager.

### **Introduction to Hyperspectral Imaging**

Hyperspectral imaging has a wide range of commercial applications including agriculture, environmental monitoring, and mineral exploration. The DoD/IC also use hyperspectral imaging in a variety of ways including characterization of effluents coming from facilities, background classification, target detection, anomaly detection, and change detection using overhead airborne or space-based platforms. Hyperspectral imaging involves a combination of imaging and spectroscopy technologies. Imagery technology allows the measurement of light intensity over a given spatial domain. Spectroscopic technology allows the measurement of light intensity as a function of wavelength. Combining the two technologies enables a measurement of light intensity with respect to both the spatial dimension and the spectral dimension. Therefore each pixel of the camera contains not just intensity, but intensity as a function of wavelength. This concept is summarized in Figure 2.

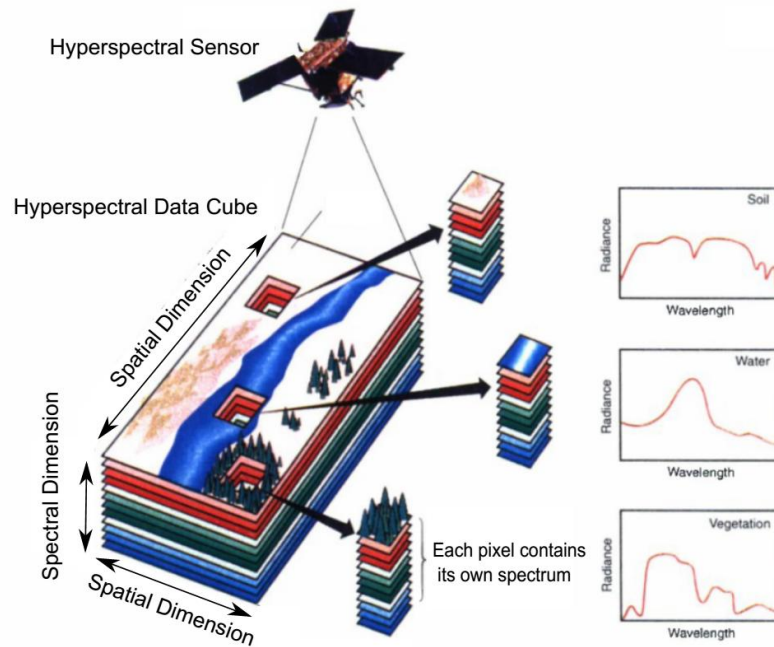


**Figure 2. Illustration of the hyperspectral imaging data cube. Each layer represents a picture of the scene for a given spectral band. For a typical color image this would contain three layers, one for red, green, and blue. For a hyperspectral image, this contains hundreds of layers. Each pixel contains a spectrum that can be used to identify the material present in the pixel. (Image adapted with permission from Ref [1]).**

As Figure 2 demonstrates, the result of a collection of hyperspectral images is typically represented as a data cube. This data cube contains the spatial information in the x-y plane and the spectral information in the z-direction. Since each pixel contains hyperspectral information, it is possible to identify a target of interest even when that target only occupies one pixel. With the use of proper post processing, this provides a great target detection capability that is not achieved with standard color imagery. One of the challenges with this is the large amount of data produced by high resolution hyperspectral imagery. Modern technology has enabled the ability to process such large data sets efficiently and thus enabled its use in military remote sensing applications where in the past it was not feasible.

The capability to do material identification with hyperspectral remote sensing is made possible by the quantum mechanical nature of the interaction of light with matter. All matter consists of atoms and molecules and it is the atomic and molecular spectroscopy derived from quantum mechanics that give the matter its optical and spectral properties. These properties result in spectral features that are observed during hyperspectral remote sensing that can potentially act as a finger print for the material being observed. A physical parameter that defines the interaction of radiation with matter is the complex index of refraction, given by

$$\tilde{n} = n + i\kappa \quad (1)$$

where the real part,  $n$ , determines the phase propagation in the material and the imaginary part,  $\kappa$ , determines the absorptive properties of the material. It is the spectral dependence of this intrinsic material property that determines the spectral signatures observed in hyperspectral remote sensing. More specifically, it is  $\kappa$  that governs the spectral absorption and emission features of the material, and therefore, its spectral signature observed in traditional hyperspectral remote sensing. With the addition of spectrally resolved polarimetric data, more information about the complex index of refraction can be determined as well through the Fresnel equations and the proper polarimetric bi-directional reflectivity distribution (pBRDF) modeling.

### **Fourier Transform Spectrometer**

The instrument that captures the spectral information for the image is the Fourier Transform Spectrometer (FTS). The FTS in the Telops is a Michelson interferometer that uses corner cubes rather than parallel mirrors. In the Michelson interferometer, a beam

splitter is used to divide the light into two beams. After the two beams have each reflected off of a different mirror, the two beams are recombined by the same beam splitter and sent to the detector. One of the mirrors is fixed and one is movable. This allows the instrument to change the optical path difference (OPD) between the two beams. Figure 3 shows a schematic of a typical FTS. When the fixed and movable mirrors are an equal distance from the beam splitter, the OPD is zero and therefore constructive interference will occur. As the mirror moves and the OPD changes, the two beams will move in and out of phase causing constructive and destructive interference patterns. In this way, an interferogram can be constructed that contains the light intensity as a function of OPD. For monochromatic light this is simply a sinusoid. If multiple frequencies are contained in the incoming light, then an interferogram that is a summation of each individual interferogram for each individual wavelength is produced. The easiest way to visualize this is by looking at bi-chromatic light. In Figure 4, two discrete wavelengths are incident upon the interferometer each producing its own interferogram. Adding the two individual interferograms together gives the actual interferogram output from the interferometer.



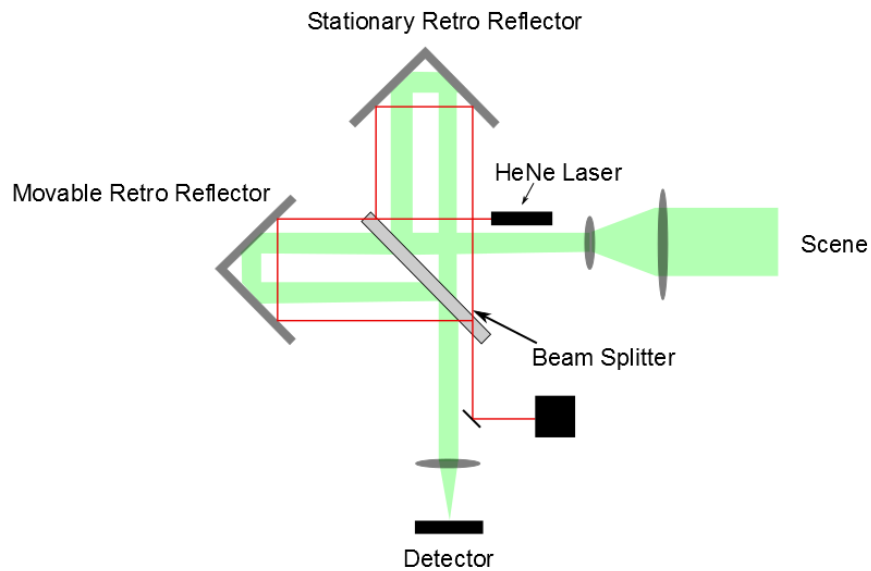


**Figure 3. Typical FTS layout. Light enters the system from the scene on the right and then is split by the beam splitter. Each path then is reflected back to the beam splitter off of the retro reflectors and therefore recombined before hitting the detector. As one of the mirrors moves the phase difference between the recombined light causes an interference pattern called an interferogram.**

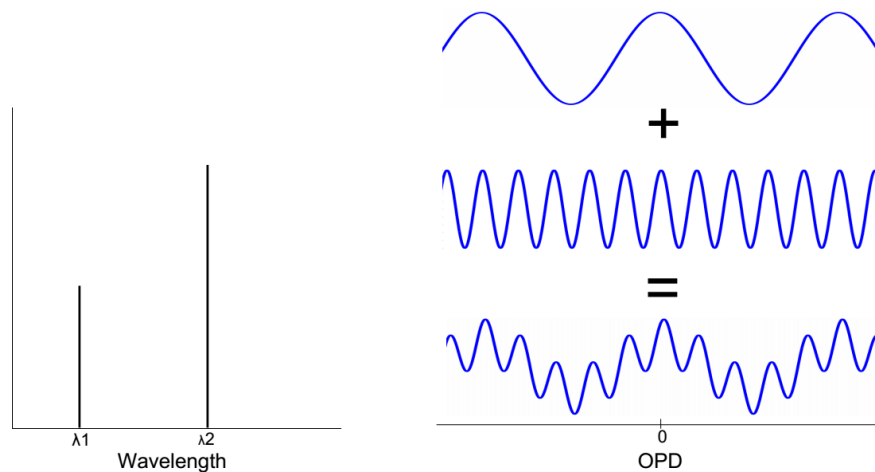


**Figure 4. The picture on the left is the frequency spectrum of the incoming light showing two different wavelengths. On the right is the interferogram produced by this bi-chromatic light. The higher frequency lower intensity wave is added to the lower frequency higher intensity wave to produce the resultant interferogram which is a superposition of the two individual waves.**

The same thing holds true for a broad-band spectrum. Each spectral component of the light source produces its own interferogram with its characteristic period, and whose amplitude is weighted by the relative spectral intensity. An interferogram such as

this is shown in Figure 5. At zero path difference (ZPD) all wavelengths constructively interfere which causes the characteristic center burst shown. At maximum path difference (MPD) the interference largely cancels out the signal.

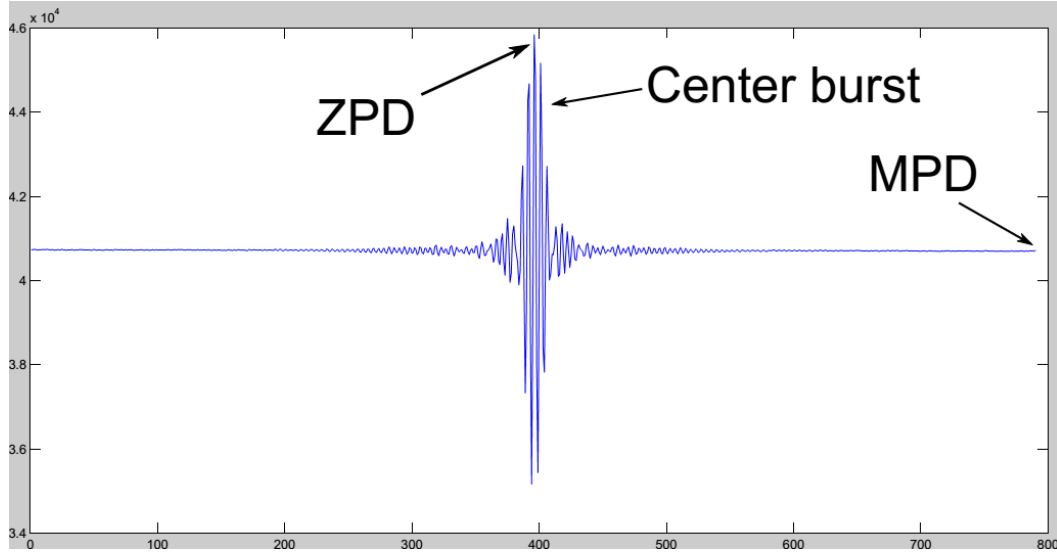


**Figure 5. A broad-band interferogram generated by the Telops Hypercam.**

One nice thing about an FTS is that the spectral resolution is proportional to MPD. It is common to define the spectral resolution of an FTS as

$$\delta\sigma = \frac{1}{4d} \quad (2)$$

and the resolving power as

$$R = \frac{\sigma}{\delta\sigma} = \frac{4d}{\sigma} \quad (3)$$

where  $d$  is the total displacement of the mirror from ZPD [2]. This allows the user to tailor the spectral resolution to the application.

In the ideal case, to produce a spectrum from the measured interferogram one must compute the inverse cosine Fourier transform of the intensity. The superposition of waves in the interferogram with the mean value subtracted out is given by

$$I(x) = \int_{-\infty}^{\infty} B(\sigma) \cos(2\pi\sigma x) d\sigma \quad (4)$$

where  $I(x)$  is the intensity of the interferogram as a function of OPD,  $x$ , and  $B(\sigma)$  is the intensity of the light as a function of wavenumber,  $\sigma$ . The spectrum can then be recovered by the inverse Fourier transform given by

$$B(\sigma) = \int_{-\infty}^{\infty} I(x) \cos(2\pi\sigma x) dx. \quad (5)$$

In reality, the limits of the integration in Equations (4) and (5) are determined by the physical constraint on the distance the mirror can travel and will be some finite value. Additionally, the cosine transform is used in the ideal case because the symmetry of the interferograms results in a real-valued Fourier transform. In real world measurements, the interferograms are not exactly symmetric and some phase shifts result in a complex interferogram and therefore a complex Fourier transform and a complex spectrum. The interferogram is also measured in discrete increments and therefore requires the use of a discrete Fourier transform (DFT) as opposed to a continuous one. Taking these factors into consideration, Equation (5) becomes

$$B(\sigma) = \frac{1}{N} \sum_{j=1}^N I(x_j) e^{i2\pi\sigma x_j} \quad (6)$$

where  $N$  is the number of discrete samples and  $x_j$  is the distance of the mirror from ZPD at those sample points. In the case of the Telops, the distance between sampling points is determined by the HeNe laser shown in Figure 3. Since the HeNe laser is a monochromatic light source, its interferogram is a sinusoid whose wavelength is the wavelength of the HeNe laser light. The interferogram is sampled every three HeNe

wavelengths. In order to meet the Nyquist sampling criteria for the irradiance spectrum, the irradiance spectrum must be band limited to a maximum wavenumber of

$$\sigma_{\max} = \frac{1}{4\Delta} \quad (7)$$

or a minimum wavelength of

$$\lambda_{\min} = 4\Delta \quad (8)$$

where  $\Delta$  is the distance between sampling points. Since the HeNe wavelength is 632.8 nm, that gives a sampling distance of  $\Delta = 1.898 \times 10^{-4}$  cm which gives  $\sigma_{\max} = 1317 \text{ cm}^{-1}$  or  $\lambda_{\min} = 7.6 \text{ }\mu\text{m}$ . The detector itself has good sensitivity over the 8–12  $\mu\text{m}$  band [3].

There are advantages and disadvantages to using an FTS. In atomic spectroscopy the line intensities often vary by orders of magnitude from line to line. The ratio between the strongest and weakest lines distinguishable by the instrument is called its dynamic range. The FTS is typically superior at measuring both absolute and relative line intensities. For an FTS, observing dynamic ranges of 1000 is routine and with care a dynamic range of 30,000 can be achieved [4]. As mentioned above, spectral resolution for an FTS is determined by the maximum OPD. This is advantageous because the user can control this parameter and therefore can control the spectral resolution. This prevents unnecessary oversampling and reduction in the signal-to-noise ratio (SNR). The FTS also benefits from the multiplex advantage, that is, it collects all wavelengths at once on every pixel as opposed to spatially splitting the signal into spectral bands. This provides an SNR boost compared with dispersive spectrometers although this is offset by the fact that shot noise is also captured for the entire spectral band as well. A disadvantage for FTS based remote sensing lies in the fact that it takes time to move the mirror through its

complete range of OPDs. This is problematic for observing scenes that are very dynamic. Additionally, there can be issues if the FTS is mounted on a moving/vibrating platform since it is sensitive to any misalignments.

## **Polarimetric Imaging in the LWIR**

### ***Introduction***

Polarimetric imaging measures the polarization state of light coming from the scene being imaged. This information can help classify materials and identify objects of interest for remote sensing and military applications. At wavelengths shorter than  $3\text{ }\mu\text{m}$ , the polarization signature of objects in the scene is dominated by surface reflections and scattering. In the LWIR band, however, objects in the scene are self-emitting measurable radiation proportional to the objects temperature and emissivity. This self-emitted radiation from the material can become partially polarized upon transmission across the surface boundary [5]. In the LWIR, it is therefore common to have contributions from both the reflected and emitted radiance from an object. This poses a difficulty since the reflected polarization component is orthogonal to the emitted polarization component. These two orthogonal polarization states add incoherently and result in a reduced apparent degree of polarization [6]. For this reason, the atmospheric conditions play a large role in polarimetric remote sensing applications in the LWIR. For a good polarimetric signature, there needs to be thermal contrast between the surrounding atmosphere which is reflecting off of the target and the target itself. If these two contributions are equal, then the apparent degree of polarization goes to zero. These effects were demonstrated by Felton *et al.* [7] who studied polarimetric imagery during a

multi-day diurnal cycle. They found that in the LWIR, cloud cover reduced the polarimetric contrast observed from their target, which was the hull of a tank. In the LWIR, clouds are similar to blackbodies that are warm in comparison to the background of a clear sky where the cold upper atmosphere is visible. They showed that the contrast was reduced to the noise level during totally overcast conditions. It is noted that the tank's engine was not running so the hull was allowed to drift with atmospheric temperature. It is also interesting to note that under the same conditions, polarimetric contrast increased in the MWIR, which indicates the increased self-emission component in the LWIR versus the reflected component in the MWIR.

### ***Stokes Vector Representation of Polarized Light***

It is convenient to represent the polarization state of light as a Stokes vector. In 1852, Stokes showed that fully polarized light can be represented as [8]

$$(\varepsilon_{0x}^2 + \varepsilon_{0y}^2)^2 = (\varepsilon_{0x}^2 - \varepsilon_{0y}^2)^2 + (2\varepsilon_{0x}\varepsilon_{0y} \cos \phi)^2 + (2\varepsilon_{0x}\varepsilon_{0y} \sin \phi)^2 \quad (9)$$

where  $\varepsilon_{0x}$  and  $\varepsilon_{0y}$  are the amplitudes of the  $x$  and  $y$  components of the electric field and  $\phi$  is the phase difference between the  $x$  and  $y$  components of the electric field.

The Stokes parameters are then defined based on this formulation where

$$\begin{aligned} s_0 &= \varepsilon_{0x}^2 + \varepsilon_{0y}^2 \\ s_1 &= \varepsilon_{0x}^2 - \varepsilon_{0y}^2 \\ s_2 &= 2\varepsilon_{0x}\varepsilon_{0y} \cos \phi \\ s_3 &= 2\varepsilon_{0x}\varepsilon_{0y} \sin \phi \end{aligned} \quad (10)$$

and

$$s_0^2 = s_1^2 + s_2^2 + s_3^2. \quad (11)$$

The Stokes parameters are real observable quantities that can be measured by a detector in the form of optical intensities or radiometric energies. The  $s_0$  term describes the total energy in the field. The  $s_1$  term describes the amount of horizontal or vertical linear polarization. The  $s_2$  term describes the amount of  $\pm 45$  degree linear polarization and the  $s_3$  term describes the amount of left or right handed circular polarization. In terms of the total scene radiance,  $L_s$ , these Stokes parameters can be arranged into a column vector such that

$$\vec{S} = \begin{pmatrix} L_s \\ L_H - L_V \\ L_{45} - L_{135} \\ L_{RCP} - L_{LCP} \end{pmatrix}. \quad (12)$$

where  $L_H$  and  $L_V$  are the horizontal and vertical components,  $L_{45}$  and  $L_{135}$  are the 45 degree and 135 degree components, and  $L_{RCP}$  and  $L_{LCP}$  are the right-handed and left-handed circular polarization components. The Stokes vector is often normalized by dividing each term by the  $s_0$  element so that

$$\vec{S} = \begin{pmatrix} s_0 = 1 \\ s_1 \\ s_2 \\ s_3 \end{pmatrix} L_s \quad (13)$$

where each term now represents the normalized Stokes parameter. In this form  $s_1$ ,  $s_2$ , and  $s_3$  range from -1 to 1 with the constraint that  $s_0 \geq \sqrt{s_1^2 + s_2^2 + s_3^2}$ . Positive values indicate horizontal,  $+45^\circ$ , or RCP, whereas negative values indicate vertical,  $135^\circ$ , or

LCP. This gives a simple way to represent the polarization state of a beam as illustrated in Figure 6.

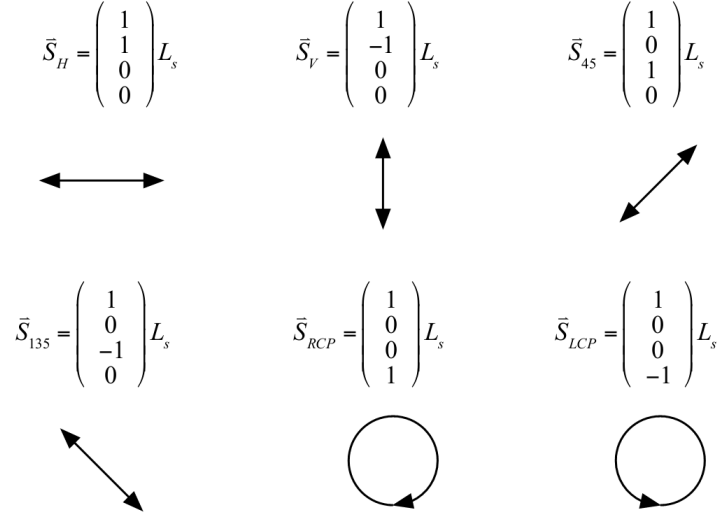


**Figure 6. Normalized Stokes vectors used to represent the polarization state of light.**

Measuring the Stokes parameters involves imaging the scene with the polarizer oriented at various angles. Since the Telops implements a division of time method for collecting at different polarizer angles, it is important that the lighting conditions and positioning of objects in the scene and the position of the instrument remain as constant as possible for a given set of polarized images. A common method of determining the Stokes parameters for linearly polarized light is known as the Modified Pickering Method. With this method, the incoming light is measured with the polarizer oriented at 0, 45, 90, and 135 degrees. The Stokes parameters are then

$$\vec{S} = \begin{pmatrix} \frac{(L_0 + L_{45} + L_{90} + L_{135})}{2} \\ L_0 - L_{90} \\ L_{45} - L_{135} \end{pmatrix}. \quad (14)$$



Once the Stokes parameters are measured, they can then be used to calculate the degree of linear polarization (DoLP) and the angle of polarization (AoP) as follows:

$$\text{DoLP} = \frac{\sqrt{s_1^2 + s_2^2}}{s_0} \quad (15)$$

$$\text{AoP} = \frac{1}{2} \tan^{-1} \left( \frac{s_2}{s_1} \right) \quad (16)$$

It should be noted that in passive remote sensing,  $s_3$  is usually close to zero so it is only important to characterize the linear polarization state of the beam [9]. Since the polarizer on the Telops is a linear polarizer, this will be the case for this research. Some nice features of the Stokes vectors are that they work for partially polarized light and they are additive in nature as long as the radiation is incoherent. The combined radiance and polarization from multiple sources of arbitrary polarization is simply the addition of their Stokes vectors. For example, the combination of horizontally and vertically polarized light is given by

$$\vec{S} = \vec{S}_H + \vec{S}_V = \begin{pmatrix} 1 \\ 1 \\ 0 \end{pmatrix} L_s + \begin{pmatrix} 1 \\ -1 \\ 0 \end{pmatrix} L_s = \begin{pmatrix} 1 \\ 0 \\ 0 \end{pmatrix} 2L_s$$

so that the result is unpolarized light. The combination of horizontal and 45 degree polarized light is

$$\vec{S} = \vec{S}_H + \vec{S}_{45} = \begin{pmatrix} 1 \\ 1 \\ 0 \end{pmatrix} L_s + \begin{pmatrix} 1 \\ 0 \\ 1 \end{pmatrix} L_s = \begin{pmatrix} 1 \\ 0.5 \\ 0.5 \end{pmatrix} 2L_s .$$

### ***Mueller Matrix Representation***

The interaction of Stokes vectors with their environment is modeled with Mueller matrices. A Mueller matrix converts an input Stokes vector into an output Stokes vector, *i.e.*

$$\vec{S}_{out} = \mathbf{M} \cdot \vec{S}_{in} = \begin{pmatrix} m_{00} & m_{01} & m_{02} & m_{03} \\ m_{10} & m_{11} & m_{12} & m_{13} \\ m_{20} & m_{21} & m_{22} & m_{23} \\ m_{30} & m_{31} & m_{32} & m_{33} \end{pmatrix} \cdot \begin{pmatrix} S_0 \\ S_1 \\ S_2 \\ S_3 \end{pmatrix}. \quad (17)$$

Any optical element can be represented by its Mueller matrix. For light traveling through an optical system consisting of many optical elements, a combined system Mueller matrix can be found through the matrix multiplication of each of the individual elements' Mueller matrices. In this case the output Stokes vector is given by

$$\vec{S}_{out} = \mathbf{M}_n \cdots \mathbf{M}_2 \mathbf{M}_1 \cdot \vec{S}_{in} \quad (18)$$

where  $\mathbf{M}_1$  is the first optical element with which the incoming Stokes vector interacts and  $\mathbf{M}_n$  is the last. The Mueller matrix of an ideal polarizer oriented at an angle,  $\theta_p$ , measured positive when rotating counterclockwise from the  $x$ -axis looking into the beam is given by

$$\mathbf{M}(\theta_p) = \frac{1}{2} \begin{pmatrix} 1 & \cos 2\theta_p & \sin 2\theta_p & 0 \\ \cos 2\theta_p & \cos^2 2\theta_p & \sin 2\theta_p \cos 2\theta_p & 0 \\ \sin 2\theta_p & \sin 2\theta_p \cos 2\theta_p & \sin^2 2\theta_p & 0 \\ 0 & 0 & 0 & 0 \end{pmatrix}. \quad (19)$$

No polarizer is perfectly ideal and there are two common metrics that characterize how close to ideal a linear polarizer is. These are the extinction ratio given by

$$ER = \frac{\tau_{\max}}{\tau_{\min}} \quad (20)$$

where  $\tau_{\max}$  and  $\tau_{\min}$  are the maximum and minimum transmission of linearly polarized light through the polarizer, and the diattenuation which is given by

$$D = \frac{\tau_{\max} - \tau_{\min}}{\tau_{\max} + \tau_{\min}}. \quad (21)$$

Diattenuation has the benefit of ranging from 1 for an ideal polarizer to 0 for a non-polarizing element. Taking diattenuation into consideration, the Mueller matrix for a linear polarizer becomes

$$\frac{1}{2} \begin{pmatrix} q+r & (q-r)\cos 2\theta_p & (q-r)\sin 2\theta_p & 0 \\ (q-r)\cos 2\theta_p & (q+r)\cos^2 2\theta_p + 2\sqrt{qr}\sin^2 2\theta_p & (q+r-2\sqrt{qr})\sin 2\theta_p \cos 2\theta_p & 0 \\ (q-r)\sin 2\theta_p & (q+r-2\sqrt{qr})\sin 2\theta_p \cos 2\theta_p & (q+r)\sin^2 2\theta_p + 2\sqrt{qr}\cos^2 2\theta_p & 0 \\ 0 & 0 & 0 & 2\sqrt{qr} \end{pmatrix} \quad (22)$$

where  $q = \tau_{\max}$  and  $r = \tau_{\min}$ . The Stokes vector and Mueller matrix approach will be used heavily in this thesis when developing the polarimetric system model and calibration methodology.

## Instrumentation

The instrument used for this research, shown in Figure 7, is an LWIR Field Portable Imaging Spectrometer (FIRST) developed by Telops, Inc. known as a Hypercam. It has been modified with a rotatable zinc selenide (ZnSe) linear wire-grid polarizer on the front end to add the polarimetric capability. The spectrometer inside the instrument is essentially a Michelson interferometer that uses corner-cubes instead of flat mirrors to reduce the effect of mechanical vibrations as the mirror is scanning. The

imaging capability is made possible by a  $320 \times 256$  photovoltaic focal plane array (FPA) made of Mercury Cadmium Telluride (HgCdTe) with a detector pitch of  $30 \mu\text{m}$ . The spectral resolution can be tuned by adjusting the distance the scan mirror travels. This provides a spectral resolution ranging from  $0.25 \text{ cm}^{-1}$  to  $150 \text{ cm}^{-1}$ . The field of view (FOV) of the instrument can also be controlled electronically by windowing down to any sub-region of the array. The time it takes to collect a full interferogram is proportional to the spectral resolution and the frame rate is proportional to the FOV, so the ability to adjust both of these parameters allows more flexibility in achieving collection goals. The maximum frame rate at full window is 300 fps and for a  $128 \times 128$  sub-region it increases to 1400 fps. At 1400 fps the instrument can collect a full data cube at  $4 \text{ cm}^{-1}$  resolution every two seconds. The ZnSe wire grid polarizer is housed in a rotation stage that allows  $\pm 180^\circ$  rotation and achieves an orientation accuracy of less than  $0.1^\circ$  and an orientation stability of less than  $0.01^\circ$ . Additional parameters are provided in Table 1.

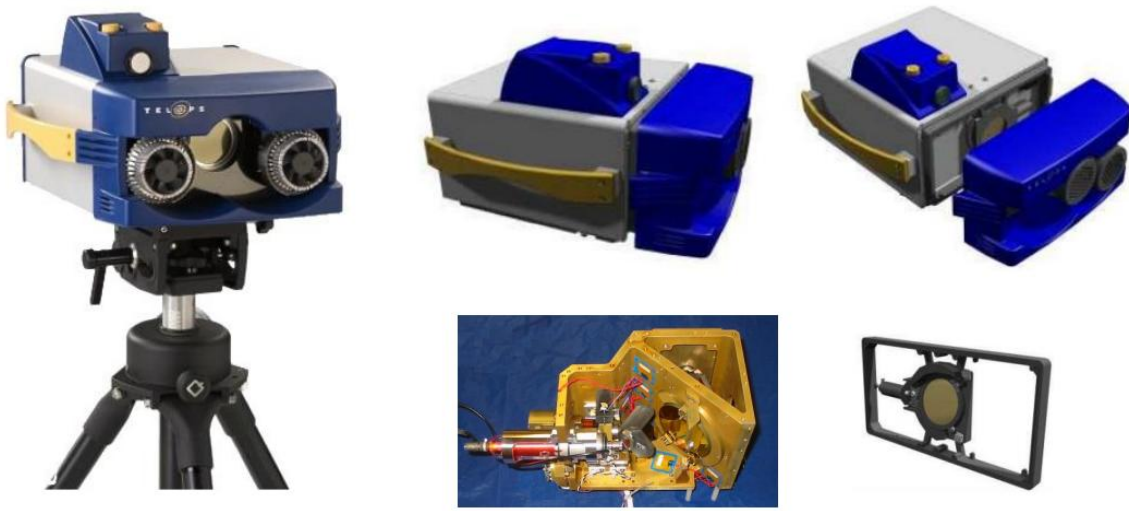


Figure 7. The Telops P-HSI system. The picture on the bottom-middle shows the interferometer module and the picture on the bottom-right shows the polarization module. (Image courtesy of Telops, Inc.).

Table 1. Telops P-HSI system parameters

<i>Parameter</i>	<i>Specification</i>
Effective focal length	8.6 cm
Aperture diameter	4.3 cm
F/#	2.0
Detector array size	$320 \times 256$
Detector pitch	$30 \mu\text{m}$
IFOV	0.35 mrad
FOV	$5.1 \times 6.4$ degrees
Spectral range	$8\text{-}12 \mu\text{m}$
Spectral resolution	$0.25\text{-}150 \text{ cm}^{-1}$
Number of spectral channels	3 to 1600
Maximum frame rate	300 Hz ( $320 \times 256$ ) 1400 Hz ( $128 \times 128$ )
Polarizer type	Wire-grid (linear)
Polarizer material	ZnSe

<b>Polarizer orientation accuracy</b>	$< 0.1^\circ$
<b>Polarizer orientation stability</b>	$< 0.01^\circ$

---

## **Previous Work Related to Spectro-Polarimetric Performance and Calibration**

This section will introduce several previous works that are relevant to this thesis. As described above, the Telops instrument is composed of many different technologies which could each have their own section. This section, however, will focus on the polarimetric aspect and the calibration aspect in general.

This section would not be complete without the mention of Sir George Stokes and Hans Mueller. In 1852, Stokes published a paper called “On the composition and resolution of streams of polarized light from different sources” [8] which was published by the Cambridge Philosophical Society. This paper was foundational to the way polarized light is represented today with so called Stokes vectors. How to describe the interaction of this polarized light, in Stokes vector representation, with the surrounding world was developed by Hans Mueller in 1943. In [10], he describes a  $4 \times 4$  matrix which converts an input Stokes vector to an output Stokes vector after having been reflected or transmitted through a material. The principles pioneered by these two scientists are used heavily in this thesis. Much of the theory and applications of polarized light, Stokes vectors, and the Mueller calculus was later covered in the texts written by Collet, Goldstein, Chipman, and Hecht [11, 12, 13, 14, 15]. An important aspect of polarimetry in the LWIR is the concept of emission polarization. The background

required to understand the phenomenon of emission polarization is provided by Sandus in his 1965 journal article in Applied Optics [5].

The use of polarized light in remote sensing and imagery applications started to gain ground as early as the 1980s with works such as “Polarization Imagery” by Walgraven [16] and “Polarization Imaging” by Solomon [17] both published in 1981. The field has continued to grow ever since. More recent work used by the author to develop an understanding of polarimetry in remote sensing applications was Schott’s books, “Fundamentals of Polarimetric Remote Sensing” and “Remote Sensing, the Image Chain Approach” [9, 18]. With regards to hyperspectral remote sensing, Eismann’s book titled “Hyperspectral Remote Sensing” was very useful; in particular the chapters, “Fourier Transform Spectrometer Design and Analysis” [2] and “Spectrometer Calibration” [19] were quite useful for this work.

For the specific application of polarimetric calibration, there are many useful sources in which to turn. The work that is the basis of the experimental polarimetric calibration effort completed in this thesis was written by Persons *et al.* and is titled “A proposed standard method for polarimetric calibration and verification” [20]. In their work, they describe a method for using linear combinations of Stokes vectors to generate highly accurate input states. From these input states and the measurement of the calibrated instrument response, the data reduction matrix can be generated. Furthermore, they describe how to present the data in such a way that is useful in understanding the non-ideal effects of the system. According to them, the method described, which allows direct measurement of the system effects, is an improvement over other methods which rely on comparing modeled calibration parameters with measured data since it is difficult

to model higher order effects. Kudenov, Pezzaniti, and Gerhart utilize similar methods and provide further mathematical detail and modeling as well as experimental validation in their 2009 paper on their microbolometer-infrared imaging Stokes polarimeter [21].

The papers written by Smith *et al.* [22] in 2000 and Blumer *et al.* [23] in 2002 both discuss the calibration of the Multispectral Infrared Stokes Imaging Polarimeter. The first paper discusses calibration in the MWIR and the later paper discusses calibration in the LWIR. In both cases, the authors found that there was a variation in instrument response as a function of retarder orientation. In the first paper, the problem was reduced by an order of magnitude by tilting the polarizer angle slightly to reduce the narcissus effect. The effect, however, was never fully calibrated out. In the second paper, a different method that involves performing a non-uniformity correction (NUC) at each retarder angle was used to achieve much better results. The current calibration method for the Telops also involves calibration at each polarizer angle. It will be shown in the Polarimetric Calibration chapter that this removes any polarimetric biases of the system to the extent that the instrument polarizer is ideal.

A more recent development for LWIR imaging polarimeters includes the micro-grid polarizer array. This involves dividing the FPA into a grid of super-pixels where each super-pixel consists of four pixels, each with a polarizing element placed in front of it at 0, 45°, 90°, and 135° respectively. By using a division of focal plane (DoFP) scheme rather than a division of time instrument such as the Telops, the user gets near real-time polarization imagery with no thermal drift in-between measurements. Any errors in the NUC, however, will cause false polarization signatures similar to thermal drift in a division of time instrument. The papers by Bowers et al in 2006 [24] and 2008 [25]



discuss the NUC of the instrument and provide useful insight into the effect these have on the polarimetric results, while Hubbs *et al.* [26] discuss the radiometric and polarization characteristics of the micro-grid FPA in their 2006 paper.

A couple of papers provided useful information with regards to determining and understanding the noise-equivalent spectral radiance (NESR) and the noise-equivalent spectral degree of linear polarization (NESDoLP). The first is a paper written by Telops Inc. in 2006, which describes a model to predict the NESR of the Telops instrument and compares this to experimental results [3]. The experimentally determined NESR in the paper is consistent with the results found in this thesis. The second paper, written by Jones and Persons [27] in 2007, develops a model to predict the performance of micro-grid polarimeters. The polarimetric performance is described in terms of the noise-equivalent DoLP (NEDoLP). The results of the model provide insight into how various system parameters affect the NEDoLP, and hence, provide a better understanding of the results obtained in this thesis.

Many of the papers referenced in this thesis and the techniques that are derived from them are done on a broadband imaging basis and not a hyperspectral basis. Despite this, it was not too difficult to extrapolate the techniques obtained from these papers to the hyperspectral case by treating each waveband as an individual image. Thus, for example, rather than obtaining a 2-D array of data reduction matrices (one for each pixel), a 3-D cube was generated with the data reduction matrix for each pixel at each waveband.

### **III. Standard HSI Calibration**

This chapter discusses the calibration procedures which must be accomplished for the Telops HSI instrument whether the polarization module is present or not. Both sections discuss the theory that supports the calibration procedures and then provide experimental data demonstrating the effectiveness of the calibrations. The insight developed in the first section, which discusses FPA non-uniformity and radiometric calibration, will be particularly useful later on when discussing the polarimetric calibration.

#### **FPA Non-uniformity and Radiometric Calibration**

When collecting radiometric data, the measured signal at the detector includes a contribution from both the scene as well as an offset radiance generated from the instrument itself. This is particularly evident in the thermal IR where optical components in the system as well as electronics are all thermally emitting photons. This signal, consisting of scene photons and instrument photons, is then subjected to transmission losses in the optical system as a function of wavelength as well as the spectral response of the detector elements. The photons must then generate electrons to be stored by the pixel elements, read out by the detector electronics and then ultimately converted to digital numbers. These digital numbers must then be converted to useful radiometric units through a radiometric calibration process. Due to pixel nonuniformity, this radiometric calibration must be accomplished on a pixel-by-pixel basis. If this is not done, fixed pattern noise from array nonuniformity will dominate the signal rendering it useless as will be shown below. To remove this nonuniformity, a two point calibration is

performed. It should be noted that the two point calibration assumes that the focal plane array (FPA) exhibits a linear response. Any level of FPA response nonlinearity will result in residual spatial nonuniformity even after the two-point radiometric calibration [19]. In general, however, good results have been achieved with the Telops using a two point calibration.

The two point calibration utilizes a spatially uniform calibration source of known radiance that is first set to a low temperature and then to a high temperature during measurement. The two temperatures are set so that they bracket the expected radiance that will exist in the scene. It is important that the calibration source overfills the field of view (FOV) of the instrument during calibration so that spatially uniform light is incident upon all pixels of the array. The linear equation used to relate digital counts to scene radiance for a particular pixel is given by

$$Y_m(\lambda) = G(\lambda)L_s(\lambda) + O(\lambda), \quad (23)$$

where  $Y_m(\lambda)$  is the measured signal in digital numbers as a function of wavelength,  $G(\lambda)$  is the instrument gain as a function of wavelength,  $L_s(\lambda)$  is the spectral radiance of the calibration source, and  $O(\lambda)$  is the instrument offset as a function of wavelength in digital numbers. Using calibration sources at two different temperatures gives a system of two equations with two unknowns which can then be solved for. The Telops has two on-board black body calibration sources that can be set to different temperatures to streamline the data collection process. For a standard camera, this is a straightforward process, but due to the nature of the FTS, there are some additional steps that must take place before the gain and offset are solved for. This has to do with the fact that the FTS

produces a discrete complex raw interferogram at each pixel rather than a real raw spectrum. The imaginary part is a result of phase errors introduced by asymmetries in the interferogram [4] and the discrete part is a result of sampling. The discrete complex raw interferograms must then be transformed to spectra using the complex discrete Fourier transform (DFT) given by

$$\tilde{Y}(\lambda) = \frac{1}{N} \sum_{j=1}^N W(x_j) I(x_j) e^{i2\pi\lambda x_j}, \quad (24)$$

where  $I(x_j)$  is the raw interferogram,  $x$  is the optical path difference, and  $W(x_j)$  is an optional apodization function to reduce ringing in the spectrum. The complex offset and gain can then be solved for using the complex version of equation (23) for the two different black body measurements. This gives:

$$\tilde{G}(\lambda) = \frac{\tilde{Y}_2(\lambda) - \tilde{Y}_1(\lambda)}{L_2(\lambda) - L_1(\lambda)}, \quad (25)$$

and

$$\tilde{O}(\lambda) = \frac{L_2(\lambda)\tilde{Y}_1(\lambda) - L_1(\lambda)\tilde{Y}_2(\lambda)}{L_2(\lambda) - L_1(\lambda)}. \quad (26)$$

The imaginary part of the raw spectrum, gain, and offset is an indication of noise and can be used as a quick upfront diagnostic of the quality of the data. For example, Figure 8 shows the real and imaginary parts for the data set that will be discussed below. Notice that the imaginary part of each curve is close to zero and the real part is much higher. This is an early indication that there is a good SNR.

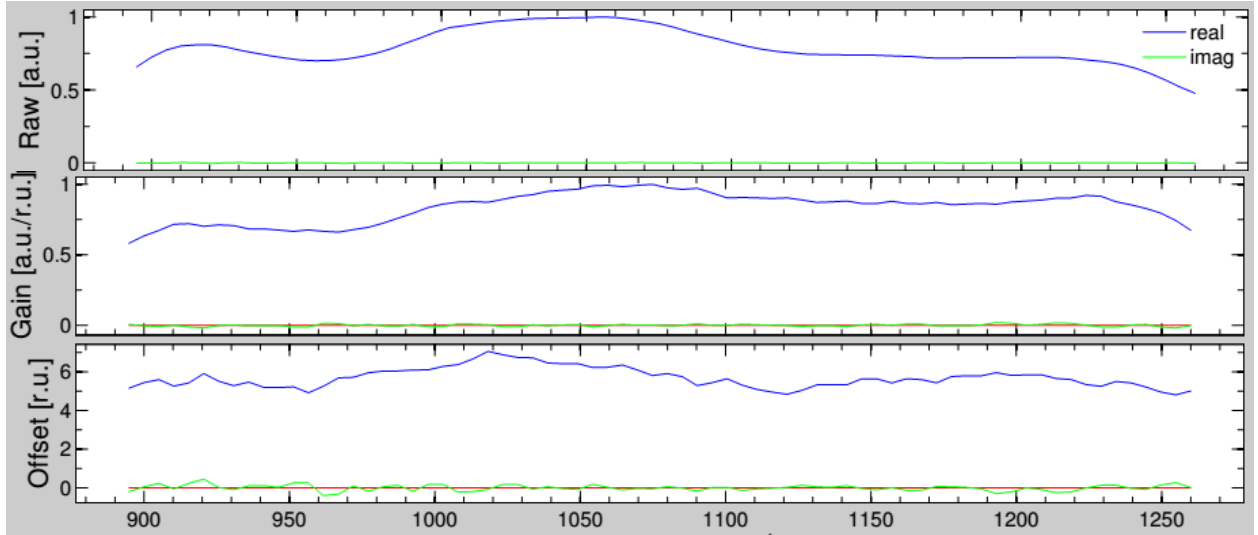


**Figure 8. The complex raw spectrum (top), complex gain (middle), and complex offset (bottom) for the data collection.**

A series of images will now be presented that walk through the process described above to go from a raw interferogram data cube to a calibrated spectral data cube. Figure 9 shows the scene that was captured with the Telops that will be used for this section. The image was taken by a visible camera mounted to the top of the Telops that is bore sighted with the infrared camera in the FTIR. The blue box roughly outlines the scene, although it needs to be shifted up and to the right several pixels to represent the true scene.



**Figure 9. Visible imagery taken of the scene with a camera mounted on top of the Telops. The blue box roughly outlines the area of the scene collected by the infrared camera in the FTIR.**

Figure 10 shows the raw band-averaged image as well as the spectral information contained within an arbitrary pixel before and after they are converted from raw interferograms to raw spectra. The figure demonstrates the importance of the nonuniformity correction. The fixed pattern noise of the array, before correction, overwhelms the signal and washes out the image as well as any resolvable spectral features. To have a useful image, the two point calibration discussed above must be implemented to remove gain and offset.

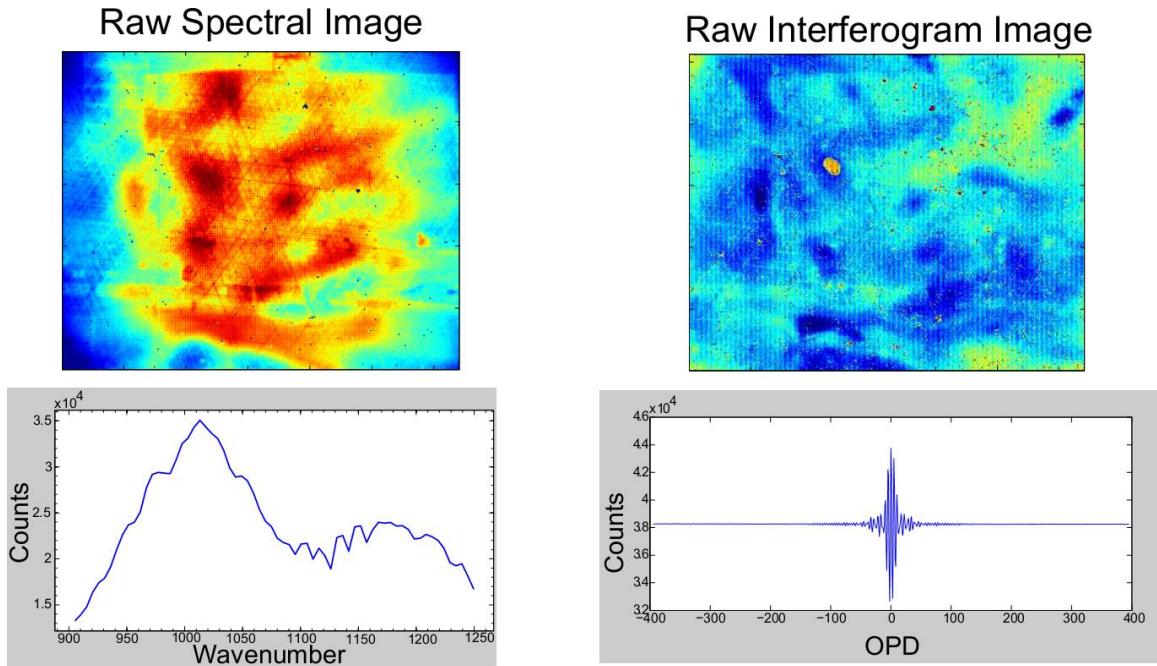


**Figure 10.** On the right, a raw band-averaged interferogram image is shown along with an interferogram from a random pixel. On the left a band-averaged image is shown after having been converted from raw interferograms to raw spectra. The raw spectrum from a pixel is shown on the bottom.

Figure 11 shows the result of applying the radiometric calibration. The spectrum for the same pixel is displayed next to the band-averaged image. For this data set the resolution was approximately  $8 \text{ cm}^{-1}$ . At this resolution, several water absorption features as well as the ozone absorption feature at  $1043 \text{ cm}^{-1}$  are now coarsely resolved revealing that this pixel is one of the sky pixels above the building. While this is a calibrated image, it is still unprocessed and many bad pixels can be seen. The image is also flipped about the vertical axis. Figure 12 shows the fully calibrated and processed band-averaged image. Here, the bad pixels have been removed, the image has been oriented properly, and a different color map is used. With an image that contains a high dynamic range such as this one, any residual FPN is negligible and can no longer be distinguished in the

image. The radiometric calibration principles discussed in this section will be useful in understanding the full polarimetric calibration which will be discussed later.

**Calibrated Unprocessed Radiance Image**

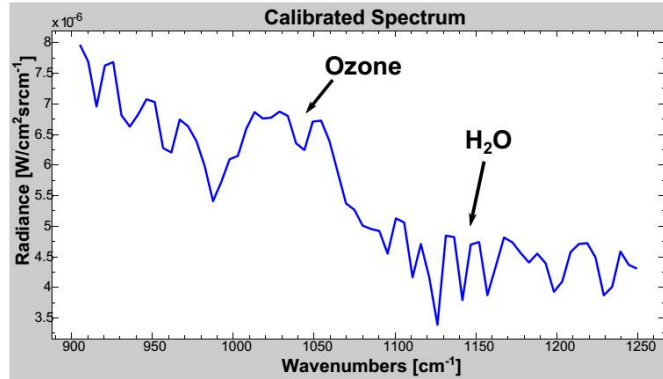
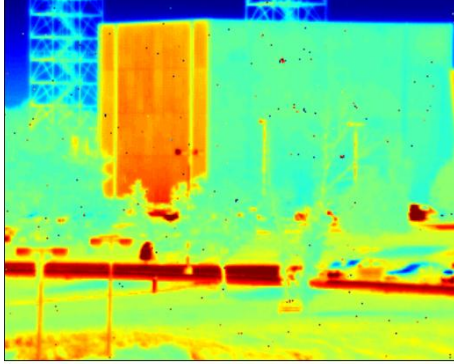


**Figure 11.** Calibrated band-averaged radiance image (left) and a spectrum (right) for one pixel looking at the sky above the building. Several water absorption features are coarsely resolved as well as the ozone feature at  $1043 \text{ cm}^{-1}$ .



**Figure 12.** Calibrated and processed band-averaged image of the scene. The bad pixels have been removed, the image has been oriented properly, and a more natural color map is used.



## Off-Axis Spectral Calibration

Spectral calibration of the Telops FTS is made possible with the use of a HeNe laser. The HeNe laser provides a monochromatic source at 632.816 nm that results in a sinusoidal interferogram. If the zero optical path difference location is known, the phase of the HeNe interferogram can be used to precisely measure the optical path difference as the mirror position changes, which in turn allows for the precise measurement of spectral features when performing the FFT. This method only works precisely, however, when the light from the scene travels the exact path through the instrument as the HeNe laser light travels. For a pixel that is off-axis with respect to the HeNe laser, the optical path difference traveled by light reaching that pixel is slightly different than that of the HeNe laser. Because of this, the spectral axis for pixels that are off-axis from the HeNe laser is scaled with respect to the true values. This results in the necessity for an off-axis spectral calibration when highly accurate spectral feature measurement is desired for all pixels. The effect is small since the off-axis angles spanned by the detector are small, but for highly accurate spectral measurements, it still needs to be corrected.

An additional effect to be considered for off-axis pixels is self apodization caused by the spatial fringe pattern created when light travels through an FTS. This fringe pattern is a function of mirror displacement. The further the mirror travels away from ZPD, the higher the spatial frequency of the fringe pattern. Since the pixels integrate spatially over the fringe pattern, if the fringe pattern causes a significant phase variation over the pixel, it will decrease the modulation depth of the interferogram. The effect increases with increasing mirror displacement. The first part of this section provides an

analysis of the apodization effect and the second part of this section discusses the off-axis spectral calibration.

In an imaging FTS, the irradiance on the FPA as a function of OPD can be written as

$$E(x, y, d) = \int_0^\infty \frac{1}{2} E_0(x, y, \sigma) \left[ 1 + \cos \left( \frac{4\pi\sigma d}{\cos \theta(x, y)} \right) \right] d\sigma \quad (27)$$

where  $x$  and  $y$  are the distance of a pixel on the FPA away from optical path center and  $d$  is the OPD [2]. It is the dependence of Equation (27) on  $\theta(x, y)$  that generates the fringe pattern of a single frame when viewing a uniform input radiance over the FOV.

$\theta(x, y)$  is given by

$$\theta(x, y) = \tan^{-1} \left( \frac{\sqrt{x^2 + y^2}}{f} \right) \quad (28)$$

where  $f$  is the focal length. To analyze the off-axis effects, it is necessary to determine the phase variation of the fringe pattern over the size of one pixel. From Equation (27), the phase term is given by

$$\phi = \frac{4\pi\sigma d}{\cos \theta(x, y)}, \quad (29)$$

taking the partial derivative of this with respect to  $\theta$  gives the differential phase change with field angle, or

$$d\phi = \frac{4\pi\sigma d \sin \theta}{\cos^2 \theta} d\theta. \quad (30)$$

From Equation (28) the angular variation over the width of a detector element,  $w$ , is given by

$$d\theta = \frac{w}{f} \cos^2 \theta. \quad (31)$$

Inserting Equation (31) into Equation (30) gives,

$$|d\phi| = \frac{4\pi\sigma dw \sin \theta}{f} = \frac{2\pi R w \sin \theta}{2f} \quad (32)$$

where  $R$  is the resolving power given by

$$R = 4d\sigma. \quad (33)$$

As mentioned before, if this phase variation over a detector element is significant, it causes apodization and thus decreased spectral resolution. A phase variation of  $2\pi$  is similar to a cosine apodization where the zeroes of the cosine are aligned with the edges of the pixel. If  $2\pi$  is plugged into Equation (32) for the phase variation and the field angle is solved for, the result is

$$\theta = \sin^{-1} \left( \frac{2f}{Rw} \right). \quad (34)$$

Therefore, in order to restrict the effect of the phase variation, the field angle must be kept smaller than the value given by Equation (34). For  $0.25 \text{ cm}^{-1}$  resolution, which is the Telops highest resolution setting, at a maximum wavenumber of  $1250 \text{ cm}^{-1}$ ,  $R = 5000$ . This means that the maximum field angle according to Equation (34) is actually larger than  $90^\circ$  which is unphysical. So even if  $\sin \theta$  in Equation (32) is its maximum value of 1, a single pixel would still not see a  $2\pi$  phase shift. To compute the phase shift that a pixel will see, first the maximum field angle must be computed based on the size of the FPA. The Telops has a  $256 \times 320$  array of pixels with a pixel size of  $30 \text{ }\mu\text{m}$ . The focal length is  $86 \text{ mm}$ . This gives a maximum angle of

$$\theta(x, y)_{\max} = \tan^{-1} \left( \frac{\sqrt{(320 \cdot 30 \mu m)^2 + (256 \cdot 30 \mu m)^2}}{86 mm} \right) = 8.14^\circ.$$

Plugging the numbers into Equation (32) gives

$$|d\phi| = \frac{2\pi \cdot 5000 \cdot 30 \mu m \cdot \sin(8.14^\circ)}{2 \cdot 86 mm} = 0.776 \text{ rad} = 44.45^\circ$$

for a single pixel. This will cause some apodization but will still allow the desired resolution to be achieved.

Now that the effect of off-axis apodization from the fringe pattern has been quantified for the Telops, the off-axis spectral scaling must be addressed. Figure 13 shows an image that was taken of the same scene as in the previous section, except at  $0.5 \text{ cm}^{-1}$  spectral resolution. The figure also shows the results of a type of end-member analysis that utilizes the k-means algorithm. The parameter used for distance in the k-means algorithm was correlation and the number of end-members was set to 10. The top right image groups end-members by color. What stands out in this image is the concentric rings of color on the front of the uniformly illuminated building and in the sky. These areas should have uniform intensity and spectral features, and yet the algorithm splits them into different groups of concentric circles with the center of the circles seemingly in the center of the FPA. This is the result of off-axis spectral scaling since this was not corrected in post-processing. As mentioned before, the off-axis scaling is a small effect but since the algorithm was forced to find ten end members in a scene that only has four true spectral end members, it picked up on the small differences caused by the scaling. The scaling can be confirmed upon inspection of the bottom plot. The sharp atmospheric absorption features do not quite line up for each end-member spectrum.

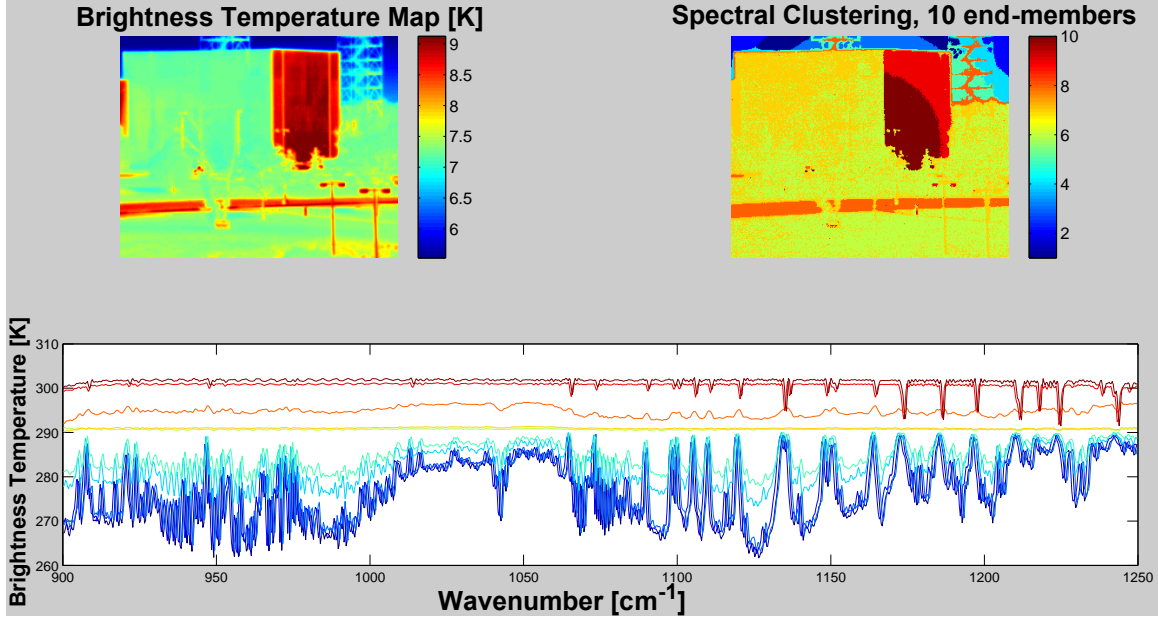


**Figure 13.** Imagery of the same scene with a  $0.5 \text{ cm}^{-1}$  spectra resolution. Shows the results of an end member analysis that utilizes the k-means algorithm with correlation as the distance parameter. The top right image groups the end-members by color and the bottom plot shows the spectrum of each end-member on a brightness temperature scale. The concentric rings are a result of off-axis spectral scaling which has not been compensated for in post processing.

This off-axis scaling effect is typically compensated for by using a modified version of the DFT in Equation (24) for each pixel that includes the  $\theta$  dependent phase term in Equation (27). The corrected DFT is

$$\tilde{Y}(x, y, \sigma) = \frac{1}{N} \sum_{j=1}^N I(x, y, d_j) e^{i \left[ \frac{4\pi\sigma d_j}{\cos \theta(x, y)} \right]}. \quad (35)$$

To implement this correction, optical path center must be known as precisely as possible. For most laboratory instruments, the optical path center is known and remains stable. For a field portable instrument such as the Telops which is often moved around and shipped to the field, the optical path center is not assumed to be constant and therefore must be determined on a periodic basis. This is accomplished through an iterative process that utilizes a uniform spectral calibration source with known spectral

features that fills the FOV of the detector. For the Telops LWIR instrument, the calibration source is a polystyrene film placed between the Telops and the blackbody. The calibration setup is shown in Figure 14. The polystyrene film overfills the FOV of the instrument. The polystyrene film has known spectral features within the sensitive band of the instrument.

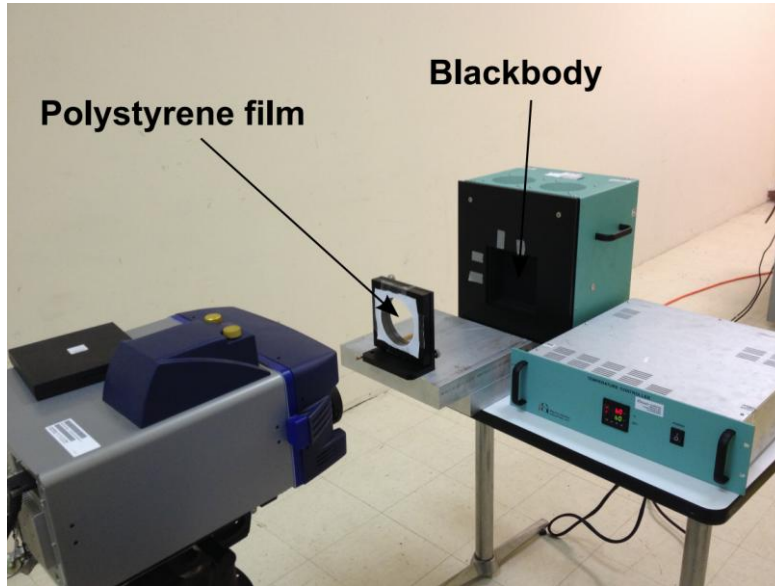


**Figure 14. Setup for generating known spectral features in the LWIR for use during off-axis spectral calibration.**

The calibration scene must generally be acquired multiple times to allow for data cube averaging in order to improve the SNR since the absorption lines must be resolved on a pixel-by-pixel basis. Figure 15 shows the spectrum acquired for several pixels at varying locations on the FPA. The box to the right shows a zoomed-in view of the absorption features. Notice that the feature does not perfectly line up for each pixel.

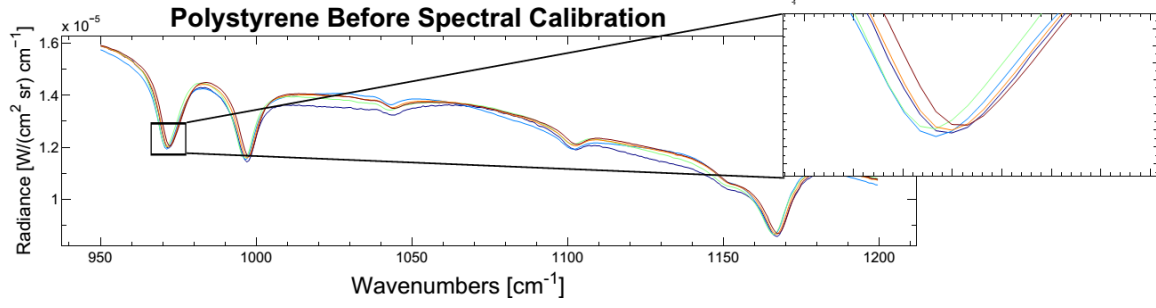


**Figure 15. Polystyrene spectra of several pixels at varying locations on the FPA before the off-axis spectral correction is applied. The zoomed in box shows that the spectral features do not perfectly line up for each pixel.**

To determine optical path center, an initial guess is chosen for optical center and random pixels are chosen from the calibration scene. The spectrum in these pixels is then oversampled and divided by their area for normalization. The pixel corresponding to optical center and the instantaneous field of view (IFOV) is then found by minimizing the pair-wise residual standard deviation between spectral features. Once optical center is found, a matrix of multiplicative spectral-axis scale factors is computed by determining the  $1/\cos \theta$  term in Equation (35). The field angle in Equation (28) can be re-written in terms of pixel location on the FPA and the instantaneous field of view (IFOV) of the pixel so that

$$\theta = \tan^{-1} \sqrt{\tan^2[(R - R_0) \cdot \text{IFOV}_y]^2 + \tan^2[(C - C_0) \cdot \text{IFOV}_x]^2} \quad (36)$$

where  $R_0$  is the row index of optical path center,  $C_0$  is the column index of optical path center,  $R$  is the row index of a given pixel,  $C$  is the column index of the pixel,  $\text{IFOV}_y$  is the IFOV in the vertical dimension, and  $\text{IFOV}_x$  is the IFOV in the horizontal dimension. The  $1/\cos \theta$  scale factor for each pixel can then be determined and placed in a matrix given by

$$\mathbf{M}(R, C) = \cos \left[ \tan^{-1} \sqrt{\tan^2 \left[ (R - R_0) \cdot \text{IFOV}_y \right]^2 + \tan^2 \left[ (C - C_0) \cdot \text{IFOV}_x \right]^2} \right]^{-1}. \quad (37)$$

The matrix of scale factors can then be used to rescale the spectral axis of each off-axis pixel for any hyperspectral data cube, thus allowing for more accurate spectral classification and target detection of objects in the scene. Figure 16 shows the polystyrene data after having been corrected with the rescaling matrix. Now the spectral features at each pixel line up almost perfectly on the spectral axis.

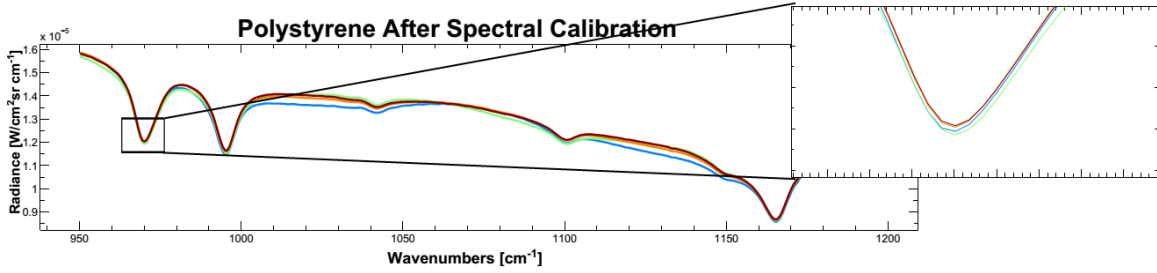


**Figure 16.** Polystyrene spectra of several pixels at varying locations on the FPA after the off-axis spectral correction is applied. The zoomed in box shows that the spectral features now align almost perfectly along the spectral axis.

Now that the rescaling matrix has been determined, the end-member analysis is performed on the corrected data. Figure 17 shows the results of the same end-member analysis after the off-axis spectral scaling has been corrected. Now the absorption features in the bottom plot all line up properly and the concentric rings on the front of the building and in the sky due to off-axis scaling are gone. Unlike before, the sky is divided into groups based on altitude, which is expected. What can also be seen now is the fringe pattern caused by the interferometer itself. This was discussed earlier and is characterized by alternating lighter and darker rings which are larger in the center and become narrower as the off-axis distance increases. This occurs in every frame, no matter what the scene; however it becomes most apparent when viewing large highly



uniform regions. It should be noted that the k-means algorithm defines end members based on both spectral correlation and intensity differences. So while there are only four true spectral end members in the scene, regions such as the sky can be further broken into groups by intensity. This feature is also what allows the algorithm to see the fringe pattern. Spectrally, the two fringing end members are the same, but their intensity is slightly different. In fact, it is hard to distinguish the two fringe intensities on the bottom plot because they are almost right on top of each other with less than a 0.5 K difference. This is close to the noise equivalent delta temperature (NEDT) for the instrument and therefore should not be visible in most cases. Other end-member algorithms exist that perform grouping based solely on spectral features. Using this type of algorithm would eliminate the subdivision of these spectrally uniform regions.

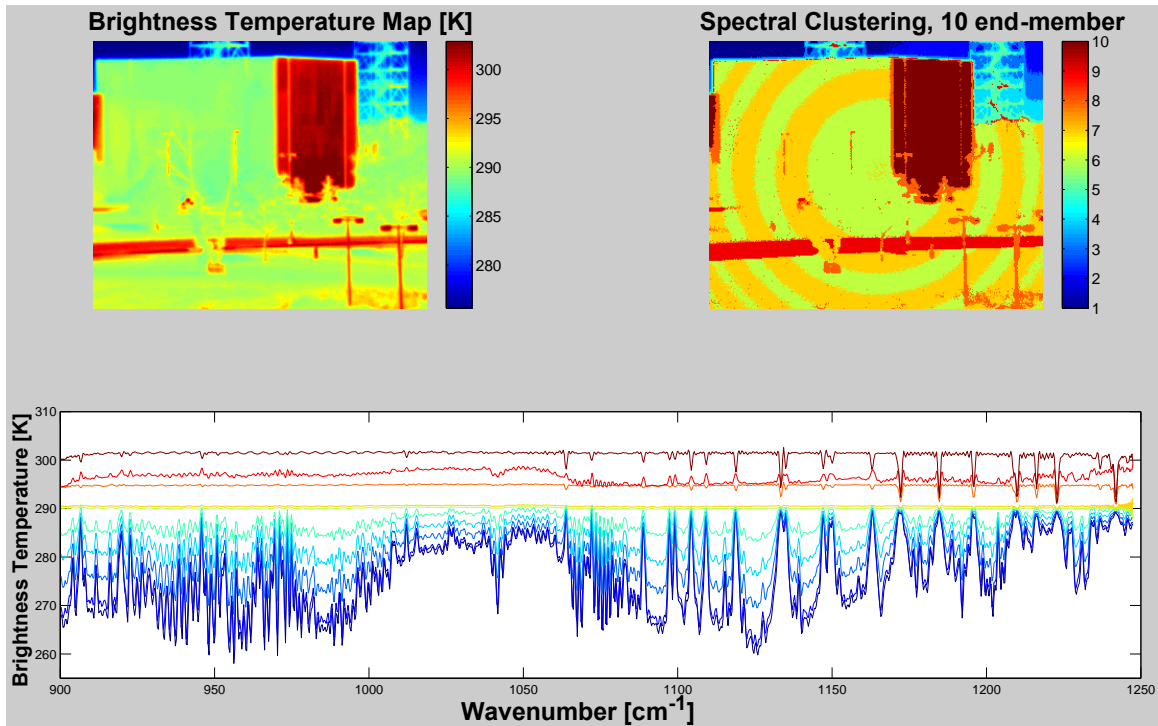


**Figure 17. Results of the end member analysis after the spectral axis scaling has been corrected. Now, all spectral features line up correctly and there are no concentric rings due to off-axis scaling. What is visible, is the fringe pattern created by the interferometer itself. This is an artifact of forcing 10 end members when there are only four true end-members. The light and dark rings are separated by a temperature difference of less than 0.5 K which is close to the NEDT of the instrument.**

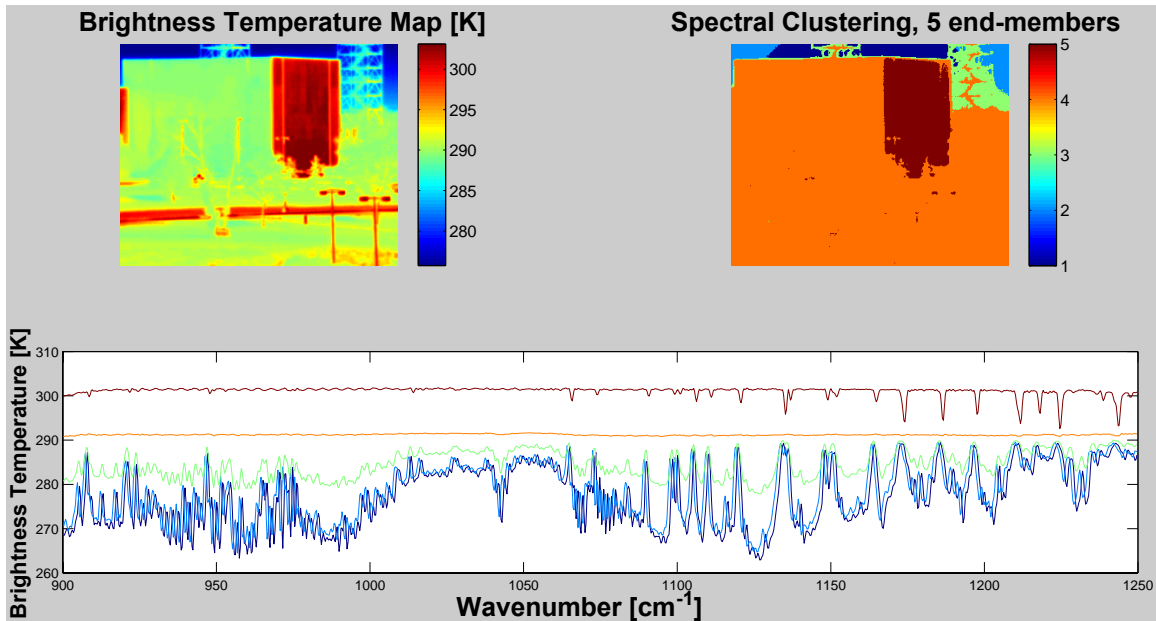
Ten end members were used above to accentuate the off-axis scaling issues.

Figure 18 and Figure 19 show the same analysis done with a more realistic five end members. Figure 18 shows the end-member analysis before spectral axis correction.

Again, the concentric rings in the sky region are visible and in this case the road is incorrectly grouped with another end-member. Figure 19 shows the end-member analysis after the spectral axis correction. Now the sky is correctly grouped by altitude and the road is identified as its own end-member. This illustrates the importance of the spectral axis correction for applications such as anomaly detection or target detection.

For example, if an intelligence analyst were using algorithms such as these to search for

an anomaly in the scene and they didn't apply a proper off-axis spectral calibration, then a key feature in the scene might be missed.



**Figure 18.** End member analysis before spectral axis correction using five end members. The concentric rings are still visible in the sky region and the road is incorrectly grouped together with another end-member.

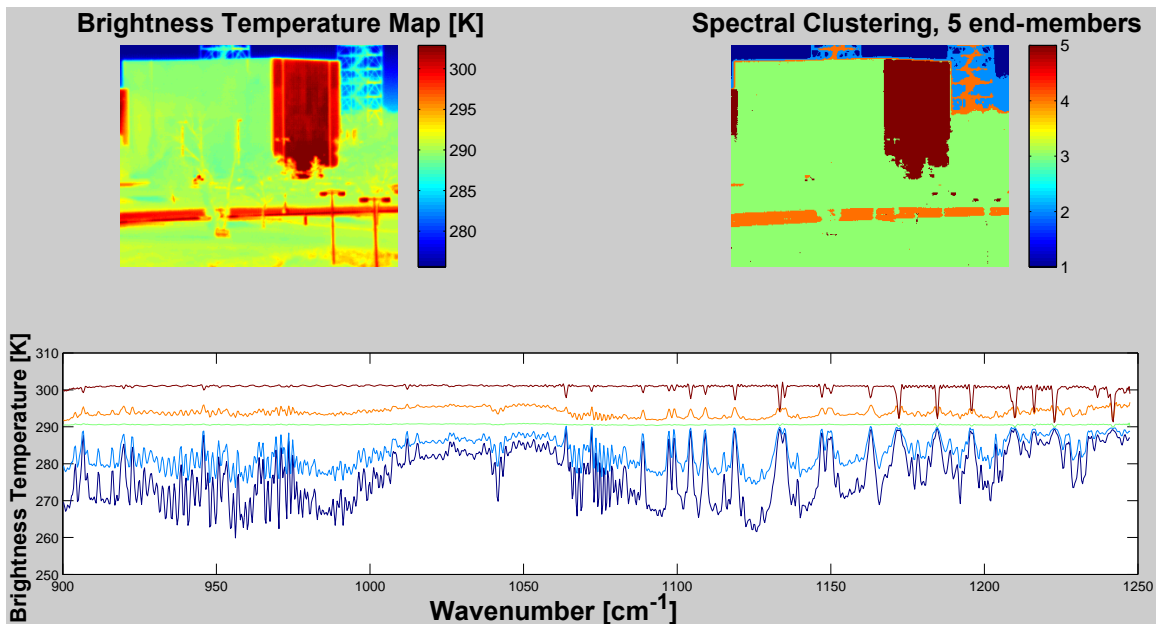


**Figure 19.** End member analysis after spectral axis correction using five end-members. The sky is now appropriately grouped by altitude and the road is properly identified as its own end member.

#### IV. Polarimetric-HSI Calibration

In addition to radiometric and off-axis spectral calibration, a polarimetric calibration is necessary in order to fully exploit the spectro-polarimetric dataset. This necessity arises from the fact that the gain of the system is sensitive to the instrument polarizer angle. Two factors must be considered: first, the instrument polarizer is self-emitting polarized light in the LWIR. This distorts the polarization state of light from the scene that strikes the detector since the emitted light is orthogonally polarized with respect to the transmitted polarized light from the scene. Second, it is possible that the other optics in the system have a slight polarization preference, although this should be small for transmissive optics. The beam splitter in the interferometer is likely to have the greatest polarization effect due to its higher reflectance and angle of incidence with respect to incoming light. To achieve highly accurate Stokes vectors, the full spectro-polarimetric gain of the system must be determined for each pixel.

The first part of this chapter starts by developing a mathematical framework for use as a polarimetric system model using Stokes vectors and the Mueller calculus. This polarimetric system model is then used to derive the calibration methodology based on the current assumption that the instrument polarizer is ideal, or in other words its diattenuation as described by Equation (21) is equal to one. The current polarimetric calibration procedure involves performing a radiometric calibration at each instrument polarizer angle. It will be shown that under the ideal polarizer assumption, this polarimetric calibration procedure works perfectly well.

The next section will then discuss the polarimetric calibration without the assumption of an ideal polarizer. In this section, the experimental methods required for characterizing the non-ideal nature of the system and providing a calibration for these non-idealities will be demonstrated.

Next, the Analysis of results section quantifies how ideally the system is performing and compares the accuracy of the measurements using the current calibration method versus the accuracy of the measurements with the additional correction for a non-ideal polarizer. It also includes a discussion of the noise and error in the measurements.

Next, the NESR of the system is determined using an unpolarized blackbody source. The concept of noise equivalent spectral DoLP (NESDoLP) is then discussed and experimentally determined using the same data set. These same parameters are then determined for a polarized source and the results from both calibration methods are compared.

### **Polarimetric System Model**

To describe the system, a Mueller/Stokes representation is used where each optical component in the system can be described by its own Mueller matrix and offset Stokes vector. The first optical component that the scene radiance will encounter is the polarizer. The Mueller matrix of the polarizer will operate on the scene Stokes vector, creating a new Stokes vector. This new Stokes vector is added to the polarizer's offset Stokes vector. It will then encounter the next optical element in the system which will then convert that Stokes vector into another Stokes vector and so on until the final Stokes vector reaches the detector. A simplified schematic of the system is shown in Figure 20

where an input Stokes vector from the scene travels through the system getting modified by each optical component in the system. After passing through the system, a Stokes vector reaches the detector which is a function of the system Mueller matrix and the instrument offset Stokes vector.

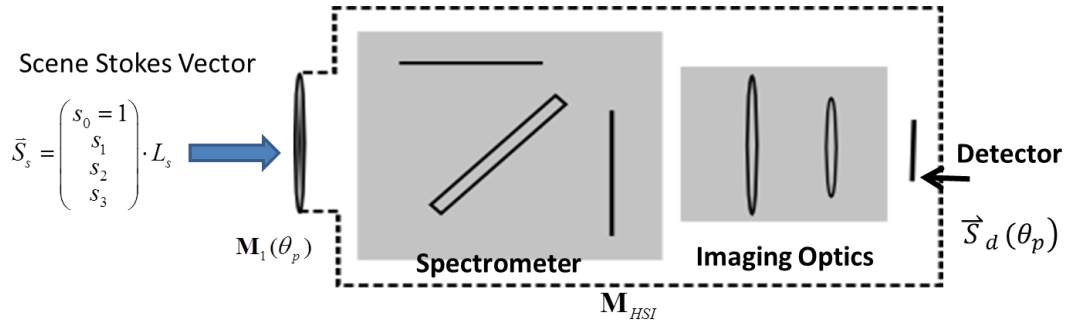


**Figure 20.** Simplified P-HSI system where an input Stokes vector from the scene travels through the system getting modified by each optical component in the system. After passing through the system, a Stokes vector reaches the detector which is a function of the system Mueller matrix and the instrument offset Stokes vector.

Using this approach, the Stokes vector reaching the detector after having passed through each optical component is given by

$$\vec{S}_d(\theta_p) = \mathbf{M}_n \left( \dots \left( \mathbf{M}_2 \left( \mathbf{M}_1(\theta_p) \vec{S}_s + \vec{S}_1(\theta_p) \right) + \vec{S}_2 \right) + \dots \right) + \vec{S}_n \quad (38)$$

where  $\mathbf{M}_1(\theta_p)$  is the Mueller matrix of the polarizer,  $\vec{S}_s$  is the Stokes vector of the incoming scene radiance,  $\mathbf{M}_n$  is Mueller matrix of the  $n^{th}$  optical component, and  $\vec{S}_n$  is the Stokes vector containing the self-emission of the  $n^{th}$  optical component.  $\vec{S}_s$  can be written as

$$\vec{S}_s = \begin{pmatrix} s_0 = 1 \\ s_1 \\ s_2 \\ s_3 \end{pmatrix} \cdot L_s \quad (39)$$

where  $s_0$ ,  $s_1$ ,  $s_2$ , and  $s_3$  are the normalized Stokes parameters and  $L_s$  is the scene radiance. Notice that  $\mathbf{M}_1(\theta_p)$  is the Mueller matrix of the polarizer and is a function of the polarizer angle,  $\theta_p$ , and  $\vec{S}_1(\theta_p)$  is the self-emission of the polarizer which is also a function of the polarizer angle. It should also be noted that each term in Equation (38) is a spectral quantity and therefore is wavenumber dependent; however, the notation is dropped for brevity. Equation (38) captures the cumulative transmitted and self-emitted radiances of each optical component as well as the polarization state as light travels through the optical system. If Equation (38) is multiplied out, it can be written as

$$\vec{S}_d(\theta_p) = \mathbf{M}(\theta_p) \vec{S}_s + \vec{S}_o(\theta_p) \quad (40)$$

where  $\mathbf{M}(\theta_p)$  is the Mueller matrix of the system as a whole and  $\vec{S}_o(\theta_p)$  is the cumulative system offset Stokes vector. Utilizing product-sum notation,  $\mathbf{M}(\theta_p)$  can be written as

$$\mathbf{M}(\theta_p) = \underbrace{\left( \prod_{i=2}^n \mathbf{M}_i \right)}_{\text{HSI}} \underbrace{\mathbf{M}_1(\theta_p)}_{\text{Polarizer}} = \mathbf{M}_{\text{HSI}} \mathbf{M}_1(\theta_p) \quad (41)$$

where the first term is the Mueller matrix of the HSI system (not including the polarizer) and the second term is the Mueller matrix of the polarizer. Equations (38) and (40) describe the Stokes vector arriving at the detector. Upon striking the detector the Stokes vector is converted from radiance units into arbitrary digital units (DN). The detector is also insensitive to the polarization state of incident light and therefore only measures the  $s_0$  element of  $\vec{S}_d(\theta_p)$ . To account for this, a detector vector can be defined as

$$\vec{D} = (d \quad 0 \quad 0 \quad 0) \quad (42)$$

where  $d$  is proportional to the spectral responsivity of the detector.

The measured signal is then given by

$$Y_m(\theta_p) = \bar{D} \cdot \bar{S}_d(\theta_p) = \bar{D} \cdot \mathbf{M}(\theta_p) \bar{S}_s + Y_o(\theta_p) \quad [\text{DN} \cdot \text{cm}^{-1}] \quad (43)$$

where  $Y_o(\theta_p)$  is the offset in DN units. Plugging in for  $\bar{D}$ ,  $\mathbf{M}(\theta_p)$ , and  $\bar{S}_s$  gives

$$Y_m(\theta_p) = \begin{pmatrix} d & 0 & 0 & 0 \end{pmatrix} \cdot \begin{pmatrix} m_{00}(\theta_p) & m_{01}(\theta_p) & m_{02}(\theta_p) & m_{03}(\theta_p) \\ m_{10}(\theta_p) & m_{11}(\theta_p) & m_{12}(\theta_p) & m_{13}(\theta_p) \\ m_{20}(\theta_p) & m_{21}(\theta_p) & m_{22}(\theta_p) & m_{23}(\theta_p) \\ m_{30}(\theta_p) & m_{31}(\theta_p) & m_{32}(\theta_p) & m_{33}(\theta_p) \end{pmatrix} \cdot \begin{pmatrix} 1 \\ s_1 \\ s_2 \\ s_3 \end{pmatrix} \cdot L_s + Y_o(\theta_p)$$

which gives,

$$Y_m(\theta_p) = d \left( m_{00}(\theta_p) + s_1 m_{01}(\theta_p) + s_2 m_{02}(\theta_p) + s_3 m_{03}(\theta_p) \right) L_s + Y_o(\theta_p)$$

and factoring out  $m_{00}$  gives,

$$Y_m(\theta_p) = \underbrace{d \cdot m_{00}(\theta_p)}_{\text{Gain}} \left( 1 + s_1 \hat{m}_{01}(\theta_p) + s_2 \hat{m}_{02}(\theta_p) + s_3 \hat{m}_{03}(\theta_p) \right) L_s + \underbrace{Y_o(\theta_p)}_{\text{Offset}} \quad (44)$$

where  $\hat{m}_{01}$ ,  $\hat{m}_{02}$ ,  $\hat{m}_{03}$  are the normalized Mueller elements of the system as a whole.

Equation (44) describes the measured signal at the detector as a function of polarizer angle and the first row of the Mueller matrix of the system. As described in Chapter III, radiometric calibration involves inputting unpolarized blackbody radiation into the system at two different temperatures and solving for the gain and offset. When this is done,  $s_1$ ,  $s_2$ , and  $s_3$  are zero and Equation (44) reduces to Equation (23) where the gain is now written in terms of the spectral detector responsivity, described with  $d$ , and the spectral transmission of the optical system, described with  $m_{00}(\theta_p)$ . After solving for the gain and offset, as discussed in Chapter III, and converting to calibrated radiance, Equation (44) can be written as

$$L_m(\theta_p) = \left( 1 + s_1 \hat{m}_{01}(\theta_p) + s_2 \hat{m}_{02}(\theta_p) + s_3 \hat{m}_{03}(\theta_p) \right) L_s \quad (45)$$



where  $L_m(\theta_p)$  is the calibrated radiance measured by the detector. Notice that there are four unknown Stokes parameters from the scene that must be determined. This requires measurement of the scene at four different polarizer angles. When this is done, the resulting system of equations based on Equation (45) can be written in matrix form as

$$\begin{pmatrix} L_m(0) \\ L_m(45) \\ L_m(90) \\ L_m(135) \end{pmatrix} = \begin{pmatrix} 1 & \hat{m}_{01}(0) & \hat{m}_{02}(0) & \hat{m}_{03}(0) \\ 1 & \hat{m}_{01}(45) & \hat{m}_{02}(45) & \hat{m}_{03}(45) \\ 1 & \hat{m}_{01}(90) & \hat{m}_{02}(90) & \hat{m}_{03}(90) \\ 1 & \hat{m}_{01}(135) & \hat{m}_{02}(135) & \hat{m}_{03}(135) \end{pmatrix} \cdot \begin{pmatrix} 1 \\ s_1 \\ s_2 \\ s_3 \end{pmatrix} L_s \quad (46)$$

or

$$\bar{L}_m = \mathbf{W} \cdot \bar{S}_s. \quad (47)$$

In Equation (47),  $\bar{L}_m$  is called the channel vector and it contains the measured radiance at each of the four polarizer angles (or channels),  $\mathbf{W}$  is called the system matrix, and  $\bar{S}_s$  is the input Stokes vector from the scene. Clearly, the system matrix transforms the input Stokes vector into the measured radiance at each of the four polarimetric channels. The system matrix, therefore, represents the polarimetric effect that the system has on the input signal. The goal of the polarimetric calibration is to determine the system matrix so that its effects can be removed. Once the system matrix is known, the input Stokes vector can be determined by multiplying both sides of the equation by the pseudo-inverse of the system matrix, that is

$$\bar{S}_s = \mathbf{W}^+ \bar{L}_m \quad (48)$$

where  $\mathbf{W}^+$  is the pseudo-inverse of  $\mathbf{W}$ . In the literature,  $\mathbf{W}^+$  is known as the data reduction matrix,  $\mathbf{R}$  so that

$$\vec{S}_s = \mathbf{R} \cdot \vec{L}_m. \quad (49)$$

Up until this point no assumptions have been made about the polarizer. The next section will determine the system matrix under the assumption that the instrument polarizer is ideal. After that, the more general case of a non-ideal polarizer is developed.

### Polarimetric Calibration under the Ideal Polarizer Assumption

To determine the system matrix, the form of  $m_{00}(\theta_p)$ ,  $\hat{m}_{01}(\theta_p)$ ,  $\hat{m}_{02}(\theta_p)$ , and  $\hat{m}_{03}(\theta_p)$  must be determined. This can be done by carrying out the multiplication in Equation (41). For an ideal polarizer,  $\mathbf{M}_1(\theta_p)$  is given by

$$\mathbf{M}_1(\theta_p) = \frac{1}{2} \begin{pmatrix} 1 & \cos(2\theta_p) & \sin(2\theta_p) & 0 \\ \cos(2\theta_p) & \cos^2(2\theta_p) & \sin(2\theta_p)\cos(2\theta_p) & 0 \\ \sin(2\theta_p) & \sin(2\theta_p)\cos(2\theta_p) & \sin^2(2\theta_p) & 0 \\ 0 & 0 & 0 & 0 \end{pmatrix}. \quad (50)$$

Plugging this into Equation (41) gives

$$\mathbf{M}(\theta_p) = \mathbf{M}'_{HSI} \mathbf{M}_1(\theta_p) = \begin{pmatrix} 1 & m'_{01} & m'_{02} & m'_{03} \\ m'_{10} & m'_{11} & m'_{12} & m'_{13} \\ m'_{20} & m'_{21} & m'_{22} & m'_{23} \\ m'_{30} & m'_{31} & m'_{32} & m'_{33} \end{pmatrix} \begin{pmatrix} 1 & \cos(2\theta_p) & \sin(2\theta_p) & 0 \\ \cos(2\theta_p) & \cos^2(2\theta_p) & \sin(2\theta_p)\cos(2\theta_p) & 0 \\ \sin(2\theta_p) & \sin(2\theta_p)\cos(2\theta_p) & \sin^2(2\theta_p) & 0 \\ 0 & 0 & 0 & 0 \end{pmatrix} \frac{1}{2}$$

where  $\mathbf{M}'_{HSI}$  is the normalized Mueller matrix of the HSI system not including the polarizer and  $\mathbf{M}_1(\theta_p)$  is the Mueller matrix of the polarizer. Carrying out this multiplication for the first row only and normalizing by the  $m_{00}$  element gives

$$\mathbf{M}(\theta_p) = \frac{1}{2} \left( 1 + m'_{01} \cos(2\theta_p) + m'_{02} \sin(2\theta_p) \right) \begin{pmatrix} 1 & \cos(2\theta_p) & \sin(2\theta_p) & 0 \\ \hat{m}_{10}(\theta_p) & \hat{m}_{11}(\theta_p) & \hat{m}_{12}(\theta_p) & 0 \\ \hat{m}_{20}(\theta_p) & \hat{m}_{21}(\theta_p) & \hat{m}_{22}(\theta_p) & 0 \\ \hat{m}_{30}(\theta_p) & \hat{m}_{31}(\theta_p) & \hat{m}_{32}(\theta_p) & 0 \end{pmatrix}.$$

Therefore,  $m_{00}(\theta_p) = \frac{1}{2}(1 + m'_{01} \cos(2\theta_p) + m'_{02} \sin(2\theta_p))$ ,  $\hat{m}_{01}(\theta_p) = \cos(2\theta_p)$ ,

$\hat{m}_{02}(\theta_p) = \sin(2\theta_p)$ , and  $\hat{m}_{03}(\theta_p) = 0$ . Notice, that since  $\hat{m}_{03}(\theta_p) = 0$ ,  $s_3$  cannot be

measured with this system. This result makes sense for a linear polarizer because  $s_3$  represents circularly polarized light. Plugging these into the system matrix gives

$$\mathbf{W}_{\text{ideal}} = \begin{pmatrix} 1 & 1 & 0 \\ 1 & 0 & 1 \\ 1 & -1 & 0 \\ 1 & 0 & -1 \end{pmatrix}. \quad (51)$$

Solving for the data reduction matrix by taking the pseudo-inverse of  $\mathbf{W}_{\text{ideal}}$  gives

$$\mathbf{R}_{\text{ideal}} = \begin{pmatrix} 0.25 & 0.25 & 0.25 & 0.25 \\ 0.5 & 0 & -0.5 & 0 \\ 0 & 0.5 & 0 & -0.5 \end{pmatrix}. \quad (52)$$

The input Stokes vector can then be determined according to Equation (49) as

$$\begin{pmatrix} s_0 \\ s_1 \\ s_2 \end{pmatrix} = \begin{pmatrix} 0.25 & 0.25 & 0.25 & 0.25 \\ 0.5 & 0 & -0.5 & 0 \\ 0 & 0.5 & 0 & -0.5 \end{pmatrix} \cdot \begin{pmatrix} L_m(0) \\ L_m(45) \\ L_m(90) \\ L_m(135) \end{pmatrix}. \quad (53)$$

Carrying out this multiplication gives

$$s_0 = \frac{L_m(0) + L_m(45) + L_m(90) + L_m(135)}{4}, \quad (54)$$

$$s_1 = \frac{L_m(0) - L_m(90)}{2}, \quad (55)$$

and

$$s_2 = \frac{L_m(45) - L_m(135)}{2}. \quad (56)$$

This result indicates that if the polarizer is ideal, then polarimetric calibration can be achieved simply by performing a radiometric calibration at each of the four polarizer angles. These calibrated radiances can then be plugged into the above equations to determine the Stokes parameters of the scene.

If the polarizer is not perfectly ideal, however, the elements of the system matrix will not be given by simple trigonometric functions and some residual error in the polarimetric measurements will remain if the above equations are used. The magnitude of the residual error will depend on how non-ideal the polarizer is and how large of an effect the optical components in the HSI system have on the polarization of light travelling through it. For a non-ideal polarizer, the system matrix must be experimentally determined. The next few sections walk through the experimental determination of the system matrix and the analysis of the system performance.

### **Polarimetric Calibration Without the Ideal Polarizer Assumption**

In order to solve for the system matrix in Equation (47), the channel vector must be measured for multiple input Stokes vectors. The number of input Stokes vectors must be large enough to allow for a proper least squares solution to the resulting matrix equation. In this case, Equation (47) becomes the following matrix equation:

$$\mathbf{L}_m = \mathbf{W} \cdot \mathbf{S} \quad (57)$$

where the channel vector is now a  $M \times N$  matrix,  $\mathbf{L}_m$ , where  $M$  is the number of instrument polarizer angles and  $N$  is the number of unique Stokes input vectors. It follows that  $\mathbf{S}$  is now a  $4 \times N$  matrix where each row corresponds to an element in the Stokes vector. In this work,  $M=4$ , which corresponds to measurements at  $0^\circ$ ,  $45^\circ$ ,  $90^\circ$ , and

135°. Clearly, in order to achieve an accurate solution for  $\mathbf{W}$ , the input Stokes vectors must be known with a high accuracy. This presents a challenge when working in the LWIR for reasons which will be discussed below. An experimental method to overcome this challenge and generate highly accurate input Stokes vectors was originally developed by Persons, C. M. *et al* in 2007 (see Reference [20]). The methodology used below is based on the method used in that paper.

### ***Methodology Overview***

An external polarizer is used to generate the known input Stokes vector; however, in the LWIR, knowledge of the input Stokes vector is more complicated than in the visible region due to the self-emission and reflected components of the external polarizer. Figure 21 illustrates this concept where  $\vec{S}_E$  is the self-emitted component,  $\vec{S}_T$  is the transmitted component, and  $\vec{S}_R$  is the reflected component.

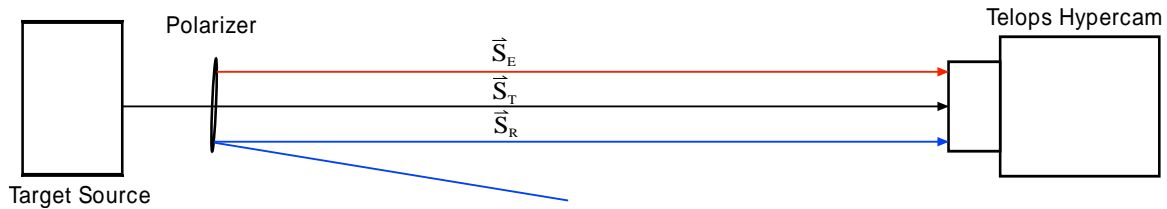


**Figure 21. Experimental setup showing blackbody radiation passing through a linear polarizer and reaching the Telops Hypercam. Illustrates the self-emitted and reflected components that also reach the instrument making it difficult to determine the transmitted component.**

In order to overcome this difficulty, the self-emitted and reflected components must be effectively removed to isolate the transmitted component. If they are not removed, they will negatively affect the data in two ways. First, the amount of radiance being emitted and reflected from the polarizer is likely not known with great accuracy and therefore knowledge of the input Stokes vector would be inaccurate. This would

introduce error in the calibration. Second, the reflected and emitted radiance from the polarizer are orthogonally polarized with respect to the transmitted component. This has the effect of reducing the DoLP of the signal that makes it to the instrument and therefore reducing the SNR of the polarimetric measurements. To remove the reflected and emitted components, the setup shown is modified with an additional reference source to control the reflected component and data is then collected at two different target source temperatures so that the two can be differenced. This reference source overfills the polarizer to ensure a uniform reflected component. Figure 22 illustrates the modified setup. In this setup, the external polarizer's plane is rotated by  $4^\circ$  and the reference blackbody is placed at the specular angle of  $8^\circ$  with respect to the Telops instrument. The reference blackbody is then kept at a constant temperature in order to control the reflected component. During the experiment, it was found that a baffle that prevented light from the target source from reflecting off of the metallic edge of the reference blackbody and then off of the external polarizer into the system was also necessary.

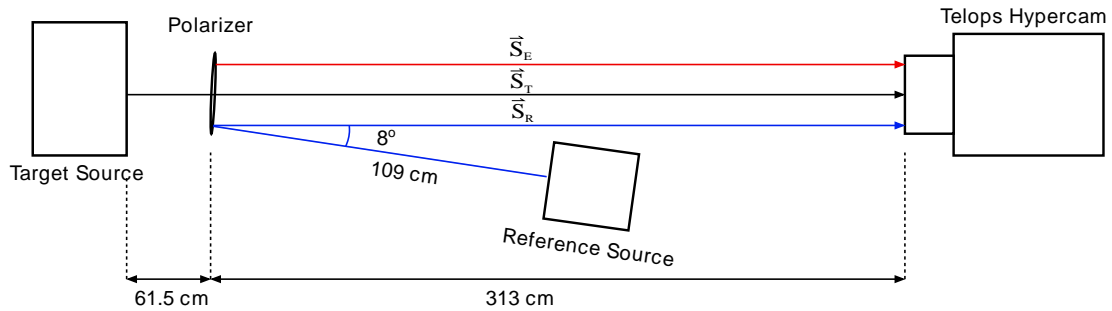


**Figure 22. Experimental setup used for polarimetric calibration. Two different target source temperatures are used for differencing and the reference source is placed at the specular angle and kept at a constant temperature.**

With this setup in place, the external polarizer is used to generate the input polarization states, and at each polarization state, data is collected at two different temperatures. The input Stokes vectors are then differenced so that

$$\begin{aligned} \bar{S}_2 &= \bar{S}_{T_2} + \cancel{\bar{S}_E} + \cancel{\bar{S}_R} \\ - \bar{S}_1 &= \bar{S}_{T_1} + \cancel{\bar{S}_E} + \cancel{\bar{S}_R} \\ \hline \Delta \bar{S} &= \Delta \bar{S}_T \end{aligned} \quad (58)$$

This gets rid of the emitted and reflected components and isolates the transmitted component. After differencing, the Stokes vector that reaches the instrument is simplified to

$$\Delta \bar{S} = \Delta \bar{S}_T = \Delta L_s \begin{pmatrix} 1 \\ D \cos(2\theta) \\ D \sin(2\theta) \\ 0 \end{pmatrix} \quad (59)$$

where  $D$  is the diattenuation of the external polarizer and  $\Delta L_s$  is the differenced radiance of the blackbody after transmission through the external polarizer. Note that since  $s_3 = 0$ , it will be dropped and the three-element Stokes vector will be used from now on. Now, Equation (57) becomes

$$\Delta \mathbf{L}_m = \mathbf{W} \cdot \Delta \mathbf{S}. \quad (60)$$

For example, if only four input polarization states were used where the external polarizer was oriented at  $0^\circ$ ,  $45^\circ$ ,  $90^\circ$ , and  $135^\circ$ , then the resulting equation would be

$$\begin{pmatrix} \Delta L_m^0(0) & \Delta L_m^{45}(0) & \Delta L_m^{90}(0) & \Delta L_m^{135}(0) \\ \Delta L_m^0(45) & \Delta L_m^{45}(45) & \Delta L_m^{90}(45) & \Delta L_m^{135}(45) \\ \Delta L_m^0(90) & \Delta L_m^{45}(90) & \Delta L_m^{90}(90) & \Delta L_m^{135}(90) \\ \Delta L_m^0(135) & \Delta L_m^{45}(135) & \Delta L_m^{90}(135) & \Delta L_m^{135}(135) \end{pmatrix} = \mathbf{W} \cdot \Delta L_s \begin{pmatrix} 1 & 1 & 1 & 1 \\ D & 0 & -D & 0 \\ 0 & D & 0 & -D \end{pmatrix} \quad (61)$$

where  $\Delta L_m^i(\theta_p)$  is the measured radiance after calibration and after differencing, and the superscript corresponds to the external polarizer angle (and therefore the input Stokes vector). Notice that  $\Delta L_s$  must be determined before  $\mathbf{W}$  can be determined. To determine  $\Delta L_s$  the channel vectors in  $\Delta \mathbf{L}_m$  are averaged and the Stokes vectors in  $\Delta \mathbf{S}$  are averaged to generate the following equation:

$$\frac{1}{4}(\Delta \bar{L}_m^0 + \Delta \bar{L}_m^{45} + \Delta \bar{L}_m^{90} + \Delta \bar{L}_m^{135}) = \mathbf{W} \cdot \begin{pmatrix} \Delta L_s \\ 0 \\ 0 \end{pmatrix}. \quad (62)$$

In the derivation of the system matrix, it was shown that the first column of  $\mathbf{W}$  is a column of ones. This was simply a result of performing a radiometric calibration at each of the four instrument polarizer angles. Utilizing this, the right side of Equation (62) can be multiplied out to give

$$\frac{1}{4}(\Delta \bar{L}_m^0 + \Delta \bar{L}_m^{45} + \Delta \bar{L}_m^{90} + \Delta \bar{L}_m^{135}) = \begin{pmatrix} \Delta L_s \\ \Delta L_s \\ \Delta L_s \\ \Delta L_s \end{pmatrix}, \quad (63)$$

which means that the best statistical solution for  $\Delta L_s$  is just the average of the channel matrix, or

$$\Delta L = \frac{1}{16} \sum_i^4 (\Delta \bar{L}_i^0 + \Delta \bar{L}_i^{45} + \Delta \bar{L}_i^{90} + \Delta \bar{L}_i^{135}). \quad (64)$$



Now, everything that is necessary to compute the system matrix is available. Solving for  $\mathbf{W}$  gives

$$\mathbf{W} = \Delta \mathbf{L}_m \cdot \Delta \mathbf{S}^+ \quad (65)$$

or

$$\mathbf{W} = \begin{pmatrix} \Delta L_m^0(0) & \Delta L_m^{45}(0) & \Delta L_m^{90}(0) & \Delta L_m^{135}(0) \\ \Delta L_m^0(45) & \Delta L_m^{45}(45) & \Delta L_m^{90}(45) & \Delta L_m^{135}(45) \\ \Delta L_m^0(90) & \Delta L_m^{45}(90) & \Delta L_m^{90}(90) & \Delta L_m^{135}(90) \\ \Delta L_m^0(135) & \Delta L_m^{45}(135) & \Delta L_m^{90}(135) & \Delta L_m^{135}(135) \end{pmatrix} \cdot \Delta L_s \begin{pmatrix} 1 & 1 & 1 & 1 \\ D & 0 & -D & 0 \\ 0 & D & 0 & -D \end{pmatrix}^+ \quad (66)$$

where again,  $\Delta \mathbf{S}^+$  is the pseudo-inverse of  $\Delta \mathbf{S}$ . From this, the data reduction matrix,  $\mathbf{R}$ , can be determined as before and this can be used to convert the measured channel vector of any scene to the corresponding input Stokes vector without the assumption of an ideal instrument polarizer.

In the example above, only four input Stokes vectors were used to make the math conceptually simpler. By using additional input Stokes vectors that are mixtures of the four primary ones described above, the calibration should be more accurate for a greater number of input states. In light of this, 12 input Stokes vectors were used rather than 4 by incrementing the external polarizer by  $15^\circ$  starting at  $0^\circ$  and going to  $165^\circ$ .

### ***Experimental Setup***

The physical setup used for this experiment was briefly discussed above and is shown in Figure 22. This section describes the experimental setup in much greater detail. The two target source temperatures were  $55^\circ\text{C}$  and  $65^\circ\text{C}$  and the reference blackbody was kept at  $30^\circ\text{C}$ . The 2-inch target blackbodies have a temperature stability of  $0.003^\circ\text{C}$

and the stability of the 6-inch reference blackbody is 0.5 °C. The onboard blackbodies used for calibration were kept at 20 °C and 60 °C and the integration time was kept at 200 $\mu$ s for all collections. At these temperatures, the calibration blackbodies bounded the scene radiance and stayed within the linear range of the instrument. The data was collected at 16  $cm^{-1}$  spectral resolution and 64 acquisitions of each scene were collected, as well as 34 acquisitions for each calibration blackbody collection for averaging purposes. The Hypercam FPA was windowed down so that only the polarizer and part of the target blackbody was in the scene. The broadband image of the scene is shown in Figure 23. As mentioned before, a baffle was placed on the left side of the polarizer so that light from the target blackbody would not reflect off of the reference blackbody and then off of the polarizer into the instrument. Before the baffle was put into place, a stripe could be seen in the image of the polarizer where the reflection off of the polarizer was taking place. The experimental setup parameters are outlined in Table 2. Parameters that are colored red are thought to be the primary limitations of the experimental setup which could be improved upon in future experiments.

**Table 2. Experimental Setup Parameters**

<i><b>Parameter</b></i>	<i><b>Specification</b></i>
<b>Target source temperatures</b>	55, 65 °C
<b>Target source stability</b>	0.003 °C
<b>Reference source temperature</b>	30 °C
<b>Reference source stability</b>	0.5 °C
<b>Calibration source temperatures</b>	20, 60 °C
<b>Avg. external polarizer diattenuation</b>	0.992

<b>Integration time</b>	200 $\mu s$
<b>Spectral range</b>	900-1250 $cm^{-1}$
<b>Spectral resolution</b>	16 $cm^{-1}$
<b>Polarizer type</b>	Wire-grid (linear)
<b>Polarizer material</b>	ZnSe
<b>Polarizer orientation accuracy</b>	1°
<b>Frame averaging</b>	64

---

In order to ensure proper alignment of the external and instrument polarizers, a dataset was collected where the polarizer was held constant and the external polarizer was rotated from 0 to 180° in 4° increments except near the maximum intensity point, where it was rotated in 1° increments for higher resolution. This was done to map the angle of the rotation stage holding the polarizer to the transmission axis of the polarizer itself. The results are shown in Figure 24. Since the instrument polarizer was kept in the horizontal position, the angle of the external polarizer at which maximum signal was achieved was used to determine the proper horizontal alignment of the external polarizer. A  $\cos^2(\theta)$  curve was fit to the data using Malus' law which is given by

$$L_m = L_0 \cos^2(\theta). \quad (67)$$

This allowed for proper orientation of the external polarizer for generating the necessary input Stokes vectors.

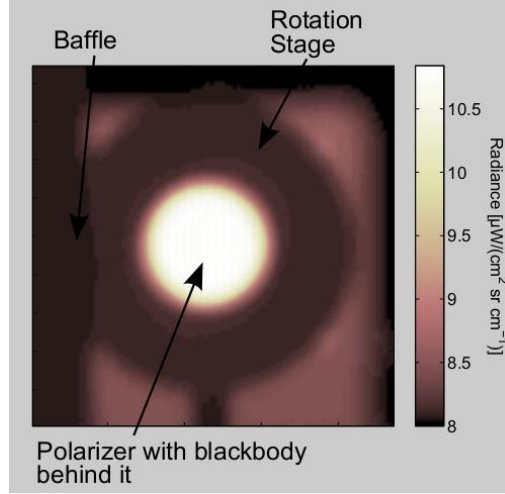


**Figure 23.** Band-averaged image of the polarizer with the 65 °C blackbody in the background. Note the active area of the blackbody overfills the polarizer but not the entire rotation stage. The baffle can be seen on the left side of the image.

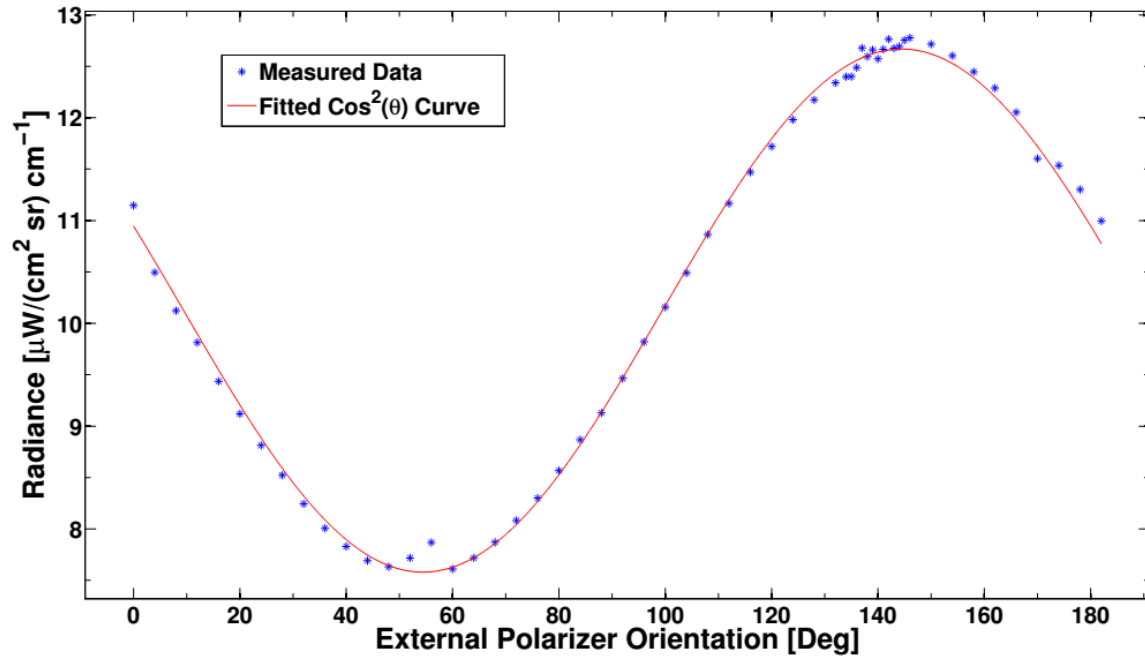


**Figure 24.** Data collected from the external polarizer as it was rotated through 180°. The angle of the external polarizer at which maximum signal was received corresponds to the best alignment between the external and internal polarizer. The solid line is the best fit  $\cos^2$  curve.

Using this setup, data was collected in 15° increments starting at 0° and going to 165° degrees resulting in 12 input Stokes vectors at the cold temperature and 12 input Stokes vectors at the hot temperature. It was important to take the high-temperature

measurement immediately following the low temperature measurement in order to minimize the temperature drift of the external polarizer. Therefore, two target blackbodies were used with one set at the high temperature and one set at the low temperature so they could be switched out quickly. The sequence of instrument polarizer angles used was also optimized in order to minimize temperature drift between orthogonal polarizer measurements, *i.e.*, the instrument polarizer collection order was  $0^\circ$ ,  $90^\circ$ ,  $45^\circ$ , and then  $135^\circ$ . This method is implemented due to the fact that calculation of the  $s_1$  and  $s_2$  Stokes elements requires differencing the two orthogonal states. Figure 25 shows the  $s_0$ ,  $s_1$ , and  $s_2$  Stokes images from the scene with the external polarizer at  $15^\circ$  and the target blackbody at  $65^\circ\text{C}$ . In the  $s_0$  image, the background scene including the blackbody and the baffle is present, whereas in the  $s_1$  and  $s_2$  images the background scene is black. This indicates that there was very little temperature drift in the scene during the collection. Additionally, Figure 26 shows the  $s_0$  image after differencing the hot and cold temperatures. This shows that the background scene is no longer visible even in the  $s_0$  image, which indicates that there was minimal temperature drift between collection of the hot and cold datasets.

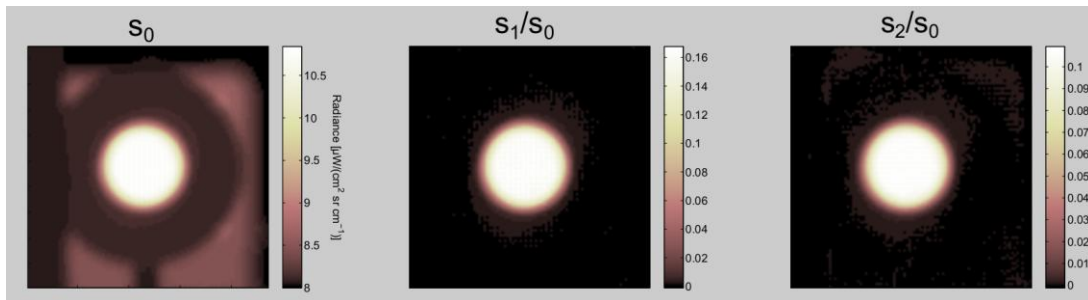


**Figure 25.** Stokes images of the scene with the target blackbody at  $65^\circ\text{C}$ . The background scene is visible in the  $s_0$  Stokes image, whereas it is not visible in the  $s_1$  and  $s_2$  Stokes images indicating that there was very little thermal drift in the scene during the collection.

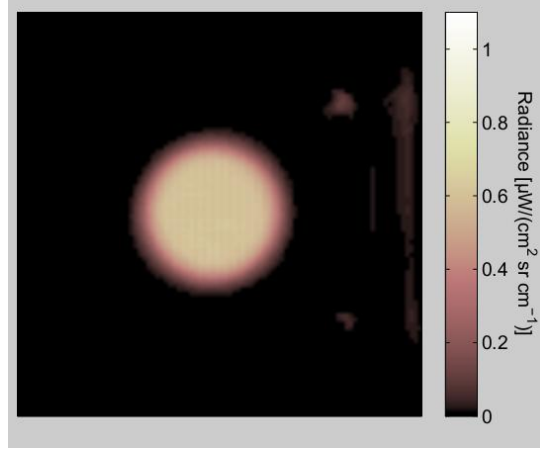


**Figure 26.**  $s_0$  image after differencing the hot and cold data. The dark background scene indicates that the thermal drift between collection of the hot and cold data was small.

Next, a channel matrix was generated based on the calibrated differenced data. Figure 27 provides a useful way of visualizing the channel matrix which helps to understand its physical significance. In the figure, each column is a channel vector which corresponds to an input Stokes vector. For visualization purposes, only four input Stokes orientations are shown rather than all 12.

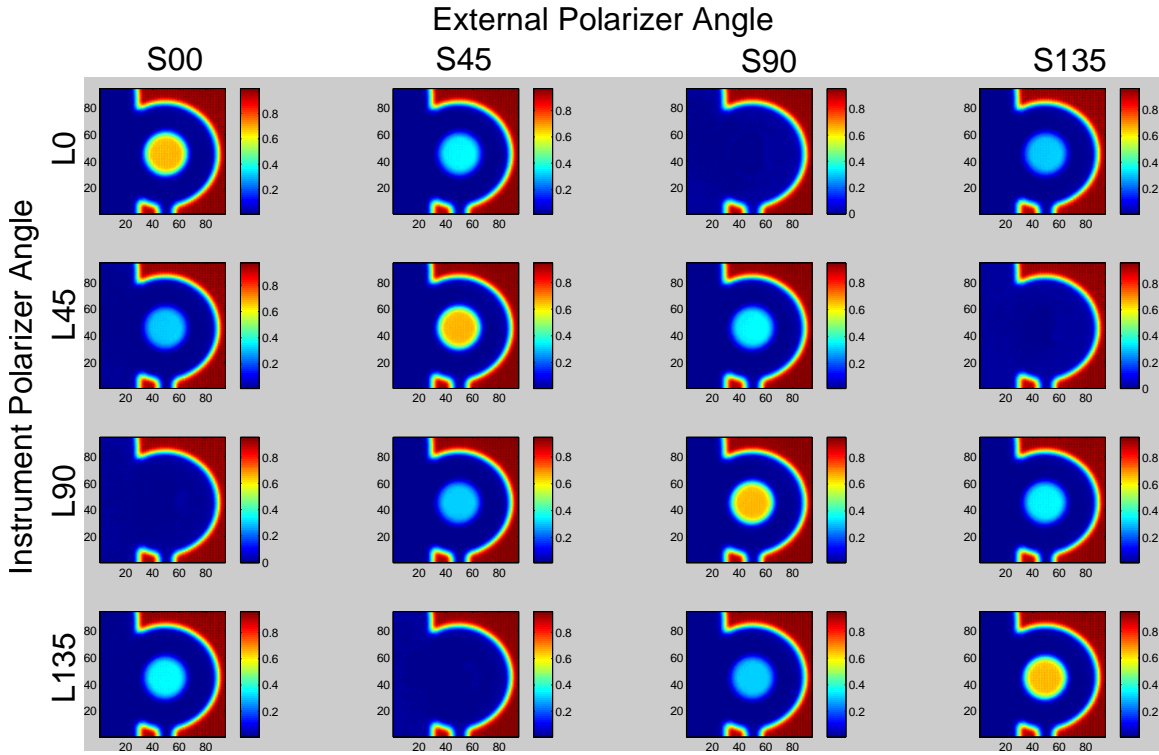


**Figure 27. Visualization of the channel matrix where each column is a channel vector corresponding to an input Stokes vector.**

In order to use the data for calculation of the system and data reduction matrices, only a circular region within the polarizer was used. To do this, a circular mask was created to remove the scene other than the circular region within the external polarizer. This is shown in Figure 28.

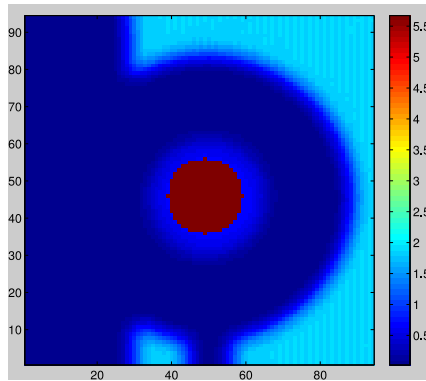


**Figure 28. Circular mask to remove all scene data other than the circular region within the polarizer.**

With this mask in place, it is easy to show the effect that differencing the hot and cold data has on  $s_1$ ,  $s_2$ , and DoLP. Figure 29 shows the  $s_1$ ,  $s_2$ , and DoLP images of the polarizer when it is horizontally aligned with the instrument polarizer. This should result in an  $s_1$  close to one, an  $s_2$  close to zero, and a DoLP close to 100%. This proves to be true for the differenced data, while it is far from true for the undifferenced data due to the reflected and emitted component discussed before. For the undifferenced data,  $s_1$  is approximately 0.2 and the percent DoLP is approximately 20%. For the differenced data,  $s_1$  is approximately 0.995 and the percent DoLP is approximately 99.5%. In practice, a DoLP of 100% is not achievable since there will always be some diattenuation that drives it down; however, noise in the measurements can potentially cause a DoLP of over 100% when using the Modified Pickering method. To demonstrate this mathematically, consider the following calculation of  $s_1$  that includes noise:

$$\begin{aligned}
 s_1 &= \frac{(L_m(0) + n(0)) - (L_m(90) + n(90))}{\frac{1}{2}[(L_m(0) + n(0)) + (L_m(90) + n(90)) + (L_m(45) + n(45)) + (L_m(135) + n(135))]} \\
 &= \frac{(L_m(0) - L_m(90)) + (n(0) - n(90))}{\frac{1}{2}[(L_m(0) + L_m(90) + L_m(45) + L_m(135)) + (n(0) + n(90) + n(45) + n(135))]} \quad . \quad (68)
 \end{aligned}$$

Therefore, if  $L_m(90)$  is close to zero as it should be if the external polarizer is horizontal, and if  $[L_m(45) + L_m(135)] < [L_m(0) + L_m(90)]$  due to noise, then this could result in an artificially high calculation of  $s_1$ . This noise is minimized by averaging multiple frames, but in this case, thermal drift of the external polarizer between measurement of the hot and cold data sets can have a similar effect. It is also interesting and somewhat



counterintuitive to note that although the  $s_1$  in the undifferenced data is much smaller than in the differenced data, the  $s_2$  value in the undifferenced data is actually closer to zero than in the differenced data. Another look at the math will reveal that this is a perfectly valid result. For the undifferenced data,  $s_1$  is given by

$$s_1 = \frac{(\bar{S}(0)_T + \bar{S}(0)_R + \bar{S}(0)_E) - (\bar{S}(90)_T + \bar{S}(90)_R + \bar{S}(90)_E)}{(\bar{S}(0)_T + \bar{S}(0)_R + \bar{S}(0)_E) + (\bar{S}(90)_T + \bar{S}(90)_R + \bar{S}(90)_E)}.$$

Assuming  $\bar{S}(90)_T \approx 0$ ,  $\bar{S}(0)_R \approx 0$ , and  $\bar{S}(0)_E \approx 0$  this gives

$$s_1 \approx \frac{\bar{S}(0)_T - \bar{S}(90)_R - \bar{S}(90)_E}{\bar{S}(0)_T + \bar{S}(90)_R + \bar{S}(90)_E} \neq 1, \quad (69)$$

whereas with the difference data,  $s_1$  is given by

$$s_1 \approx \frac{\Delta \bar{S}(0)_T}{\Delta \bar{S}(0)_T} \approx 1. \quad (70)$$

This shows that in the differenced data,  $s_1$  should be close to 1, but in the undifferenced data if the emitted and reflected components are significant then  $s_1$  will not be close to one. Calculation of  $s_2$  in the undifferenced data is given by

$$s_2 = \frac{(\bar{S}(45)_T + \bar{S}(45)_R + \bar{S}(45)_E) - (\bar{S}(135)_T + \bar{S}(135)_R + \bar{S}(135)_E)}{(\bar{S}(45)_T + \bar{S}(45)_R + \bar{S}(45)_E) + (\bar{S}(135)_T + \bar{S}(135)_R + \bar{S}(135)_E)}$$

where  $\bar{S}(45)_T \approx \bar{S}(135)_T$ ,  $\bar{S}(45)_R \approx \bar{S}(135)_R$ , and  $\bar{S}(45)_E \approx \bar{S}(135)_E$ , which gives

$$s_2 \approx \frac{0}{2(\bar{S}_T + \bar{S}_R + \bar{S}_E)} \approx 0. \quad (71)$$

For the differenced data,  $s_2$  is given by

$$s_2 \approx \frac{0}{\Delta\bar{S}(45) + \Delta\bar{S}(135)} \approx 0. \quad (72)$$

In this case, the numerator for both the undifferenced and differenced data is approximately zero, but the denominator is much smaller for the differenced data. So to any extent that the numerator is not zero, the differenced calculation of  $s_2$  will always be larger. A non-zero numerator can result from noise in the measurements and polarizer misalignment.

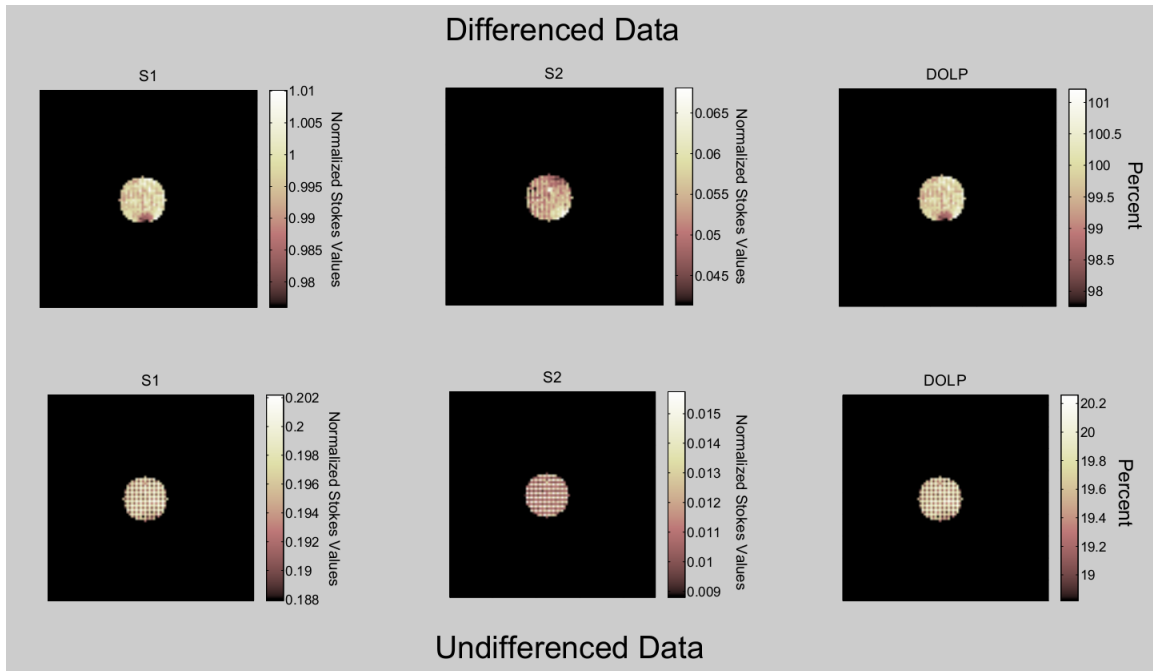


**Figure 29. Images showing the effect on the Stokes elements and DoLP of differencing the high and low temperature data sets. The external and internal polarizers are aligned horizontally which should result in a value of  $s_1$  close to one and  $s_2$  close to zero with a DoLP close to 100%. In the differenced data this is true whereas in the undifferenced data this is far from true due to the reflected and emitted components.**

## Analysis of Results

### *Evaluation of System Matrices*

Comparing the experimentally determined system matrix to the ideal system matrix provides valuable insight into how ideal or non-ideal the system is performing.

All of the non-ideal effects can be captured in a single Mueller matrix as follows:

$$\bar{L}_m = \mathbf{W} \cdot \bar{S} \equiv \mathbf{W}_{\text{ideal}} \mathbf{M}_{\Delta} \cdot \bar{S} \quad (73)$$

where the measured system matrix has been split into the ideal system matrix multiplied by a Mueller matrix,  $\mathbf{M}_{\Delta}$ , called the Mueller deviation matrix [20]. From Equation (73),  $\mathbf{M}_{\Delta}$  can be determined with

$$\mathbf{M}_{\Delta} = \mathbf{W}_{\text{ideal}}^+ \mathbf{W}. \quad (74)$$

If the system were ideal, this matrix would be equal to the identity matrix, so any deviations from the identity matrix is an indication of non-ideal effects. These non-ideal effects are a result of the non-ideal nature of the instrument polarizer, the non-zero diattenuation of the HSI instrument following the polarizer, the non-linearity of the detector, and other effects such as noise. The Mueller deviation matrix also has the interesting property that it converts an input Stokes vector into the Stokes vector that would be measured by the system if it were assumed to be ideal, *i.e.*

$$\bar{S}_m = \mathbf{M}_{\Delta} \cdot \bar{S}_{in}. \quad (75)$$

This provides another useful way to understand physically what the system is doing. By multiplying the Mueller deviation matrix by various ideal input Stokes vectors and seeing what comes out, one gains an understanding of how well the system is performing and what the different biases are. In fact, another method of calibrating the instrument via

direct determination of the Mueller deviation matrix can be developed. Solving for the Mueller deviation matrix with multiple input Stokes vectors gives

$$\mathbf{M}_{\Delta} = \mathbf{S}_m \cdot \mathbf{S}_{in}^+ . \quad (76)$$

Once the Mueller deviation matrix is determined, Equation (73) can be used to determine the system matrix via

$$\mathbf{W} = \mathbf{W}_{ideal} \mathbf{M}_{\Delta} \quad (77)$$

and the data reduction matrix can then be determined by taking the pseudo-inverse of  $\mathbf{W}$ . This method is effectively the same as the previous method mathematically and is simply provided as an additional option.

Recall that the ideal system matrix is given by

$$\mathbf{W}_{ideal} = \begin{pmatrix} 1 & 1 & 0 \\ 1 & 0 & 1 \\ 1 & -1 & 0 \\ 1 & 0 & -1 \end{pmatrix} \quad (78)$$

and as mentioned above, the corresponding ideal Mueller deviation matrix is given by the identity matrix, *i.e.*

$$\mathbf{M}_{\Delta} = \begin{pmatrix} 1 & 0 & 0 \\ 0 & 1 & 0 \\ 0 & 0 & 1 \end{pmatrix}. \quad (79)$$

Using the experimental setup and methodology described above, a system matrix was computed for the Telops Hypercam. Since the Hypercam is an imaging spectrometer, this had to be done on a pixel-by-pixel and band-by-band basis, creating a data cube of system matrices. Since it is impractical to report the results for each pixel at each band, a

spectrally and spatially averaged system matrix was also computed. The resulting system matrix is

$$\mathbf{W}_{avg} = \begin{pmatrix} 1.015 & 1.015 & 0.010 \\ 1.000 & 0.011 & 0.999 \\ 0.992 & -0.988 & 0.018 \\ 0.992 & 0.010 & -1.004 \end{pmatrix} \quad (80)$$

While not perfectly matching the ideal matrix, the results show that on an averaged basis, the system is performing very close to ideally. The fact that the first column is not a column of ones suggests that the radiometric calibration was not perfect or that the temperature of the blackbody sources were not stable. To prevent applying a polarimetric bias to unpolarized light, the first row must be set to ones. The corresponding average Mueller deviation matrix is

$$\mathbf{M}_{\Delta} = \begin{pmatrix} 1.000 & 0.007 & 0.001 \\ 0.000 & 1.001 & -0.014 \\ 0.000 & 0.011 & 1.001 \end{pmatrix}. \quad (81)$$

As mentioned above, the Mueller deviation matrix is used to calculate the Stokes vector that the system would measure without any correction and this provides another good way to evaluate how well the system is performing by multiplying this Mueller deviation matrix by various ideal Stokes vectors. For instance, if perfectly horizontally polarized light were incident on the instrument, the output Stokes measurement would be

$$\vec{S}_m = \begin{pmatrix} 1.000 & 0.007 & 0.001 \\ 0.000 & 1.001 & -0.014 \\ 0.000 & 0.011 & 1.001 \end{pmatrix} \begin{pmatrix} 1 \\ 1 \\ 0 \end{pmatrix} = \begin{pmatrix} 1.007 \\ 1.013 \\ 0.015 \end{pmatrix}; \quad (82)$$

Similarly, vertically polarized incident light gives

$$\vec{S}_m = \begin{pmatrix} 0.993 \\ -1.001 \\ -0.011 \end{pmatrix}, \quad (83)$$

45° incident light gives

$$\vec{S}_m = \begin{pmatrix} 1.001 \\ -0.014 \\ 1.001 \end{pmatrix}, \quad (84)$$

and 135° incident light gives

$$\vec{S}_m = \begin{pmatrix} 0.999 \\ 0.014 \\ -1.001 \end{pmatrix}. \quad (85)$$

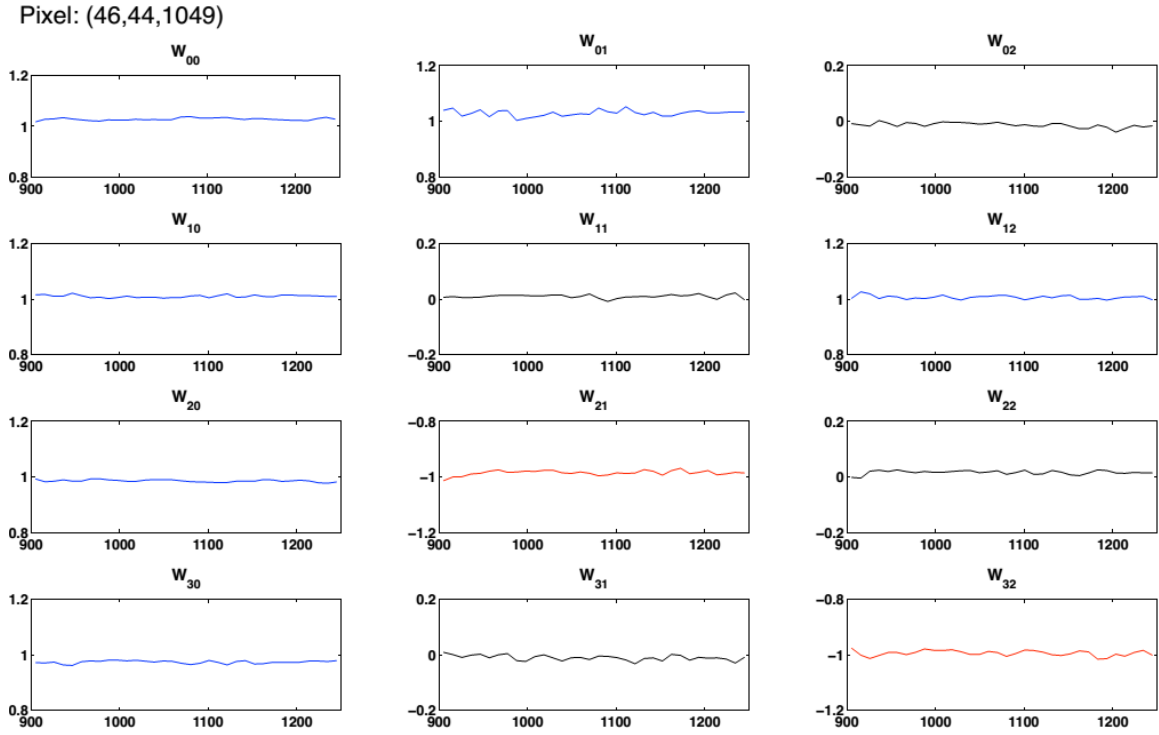
These results indicate less than 1.5% error in most cases before any further polarimetric calibration is performed. The DoLPs associated with these four measurements are 99.4%, 100.9%, 100.1%, and 100.2% respectively. While DoLPs of over 100% are unphysical, recall the mathematical argument in Equation (68) and the fact that the system matrix is computed with a least squares solution to measurements subject to noise and limited input accuracy.

Since the instrument is an imaging spectrometer, it is also important to evaluate the performance on a pixel-by-pixel and band by band basis. To start with, four random pixels at four random bands were selected to report the system matrix of those individual pixels at the respective individual bands. The results are given below:

$$\begin{aligned}
\mathbf{W}_1 &= \begin{pmatrix} 1.027 & 1.023 & -0.010 \\ 1.004 & 0.005 & 1.010 \\ 0.991 & -0.987 & 0.016 \\ 0.979 & -0.001 & -0.998 \end{pmatrix} & \mathbf{W}_2 &= \begin{pmatrix} 1.035 & 1.025 & -0.012 \\ 1.005 & -0.002 & 1.001 \\ 0.968 & -0.989 & 0.014 \\ 0.992 & -0.026 & -1.022 \end{pmatrix} \\
(46, 44, 1049) & & (48, 54, 998) & \\
\mathbf{W}_3 &= \begin{pmatrix} 1.014 & 1.036 & 0.004 \\ 1.000 & 0.007 & 0.967 \\ 0.990 & -1.000 & 0.031 \\ 0.996 & 0.014 & -1.021 \end{pmatrix} & \mathbf{W}_4 &= \begin{pmatrix} 1.032 & 1.041 & -0.008 \\ 1.003 & 0.021 & 1.003 \\ 0.990 & -0.972 & 0.020 \\ 0.985 & -0.012 & -0.981 \end{pmatrix} \\
(49, 51, 1101) & & (54, 40, 915) &
\end{aligned}$$

where the numbers in parenthesis below the matrices corresponds to the pixels' row, column, and band in wavenumbers, respectively. This shows that the system is generally within about 4% of the ideal case for the pixels selected even at the individual pixel and individual band level when no spatial or spectral averaging has taken place. A more complete view of the spectral nature of each of the four pixels selected is shown in Figure 30. The elements of the system matrix for each of the four pixels discussed above are plotted spectrally. While there is some noise in the spectral elements, the results are good overall, showing that the elements of the system matrix are spectrally flat for each individual pixel. The lines are color coded as a visual aid. Blue lines correspond to elements with a value near one, black lines are near zero, and red lines are near negative one. It is common to do some spatial averaging over a group of pixels that are imaging a spatially uniform part of the scene. Any averaging of this nature will reduce the noise and flatten the lines out further. Figure 31 shows the plot of the spatially averaged system matrix with the standard deviation represented with shaded bands. Note that the scale on this plot is much narrower than the scale on the individual pixel plots to aid visualization of the noise in the measurements. It is clear that the majority of the noise is

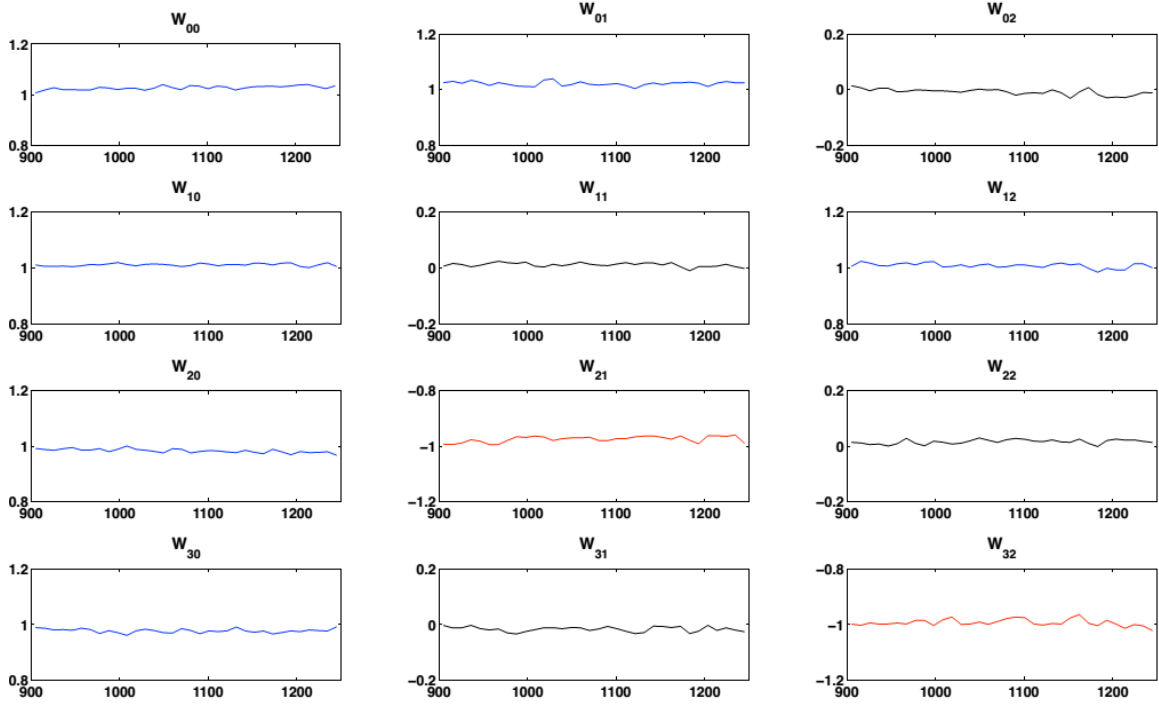
removed as a result of the spatial averaging. The average standard deviation in the measurement of the system matrix ranges from 0.35% to 0.77%.



a.) Spectral plot of the W matrix elements for pixel 1.

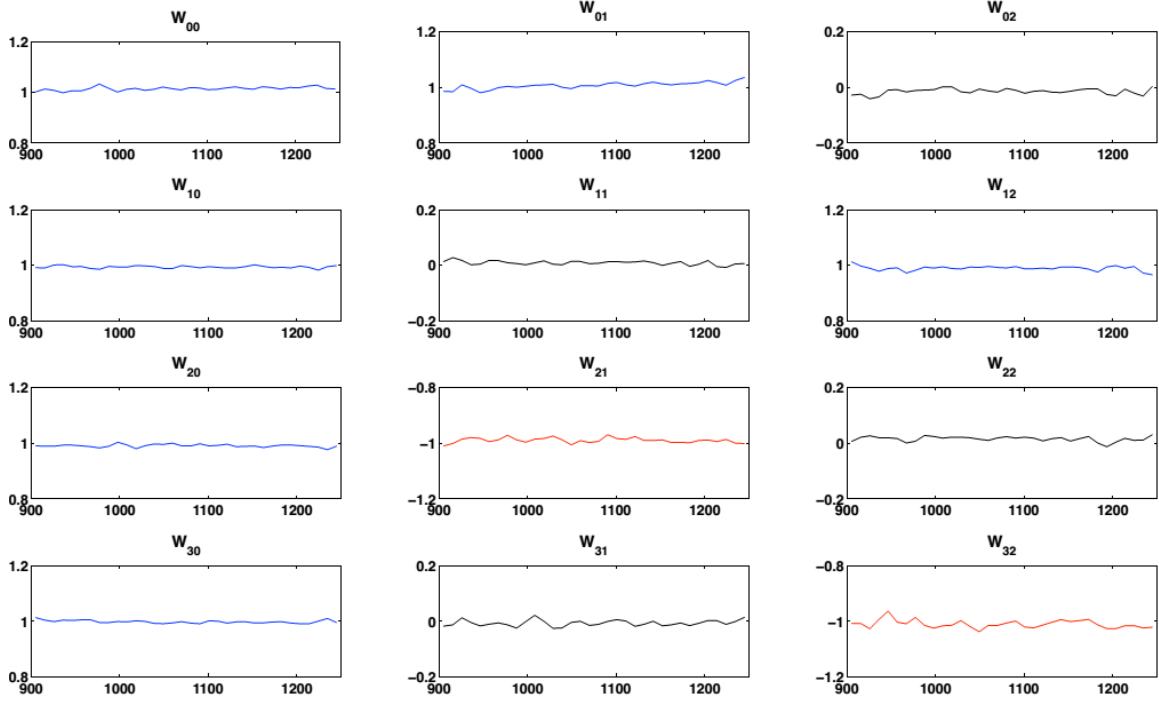


Pixel: (48,54,998)



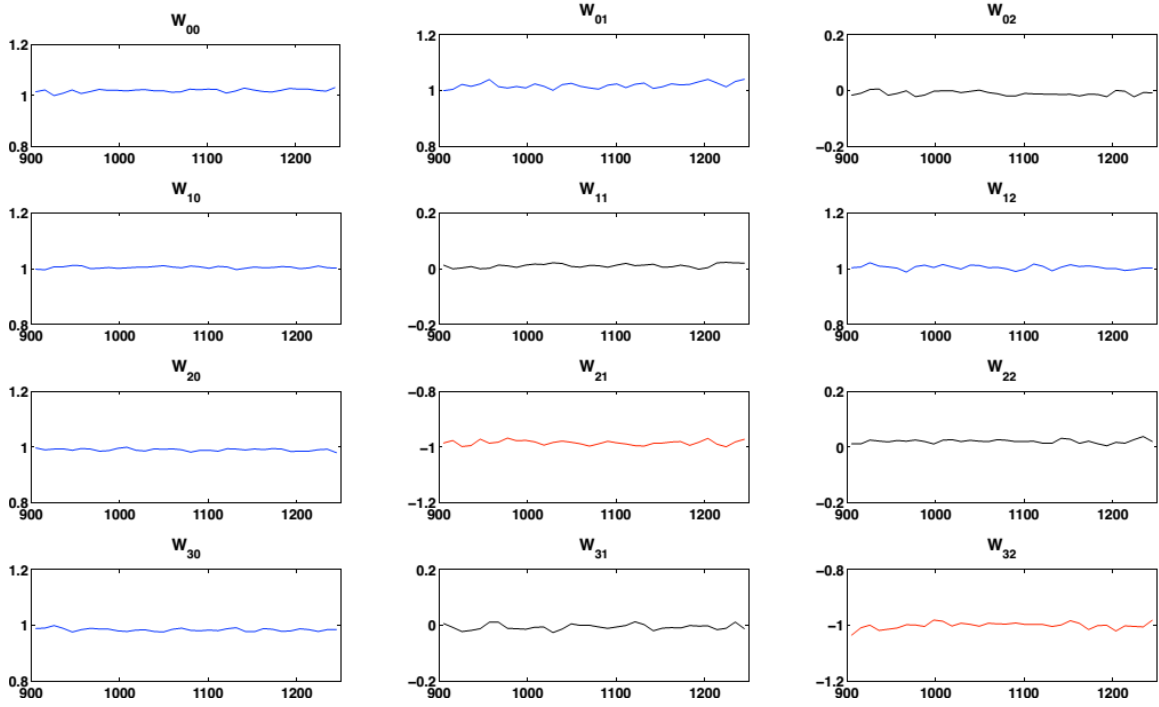
b.) Spectral plot of the W matrix elements for pixel 2.

Pixel: (49,51,1101)



c.) Spectral plot of the W matrix elements for pixel 3.

Pixel: (54,40,915)



d.) Spectral plot of the W matrix elements for pixel 4

**Figure 30.** Spectral plots of the system matrix elements for each of the four pixels discussed above. The elements of  $W$  for each individual pixel are spectrally flat other than the random noise seen in the plots. The lines are color coded as a visual aid. Blue lines correspond to elements with a value near one, black lines are near zero, and red lines are near negative one.

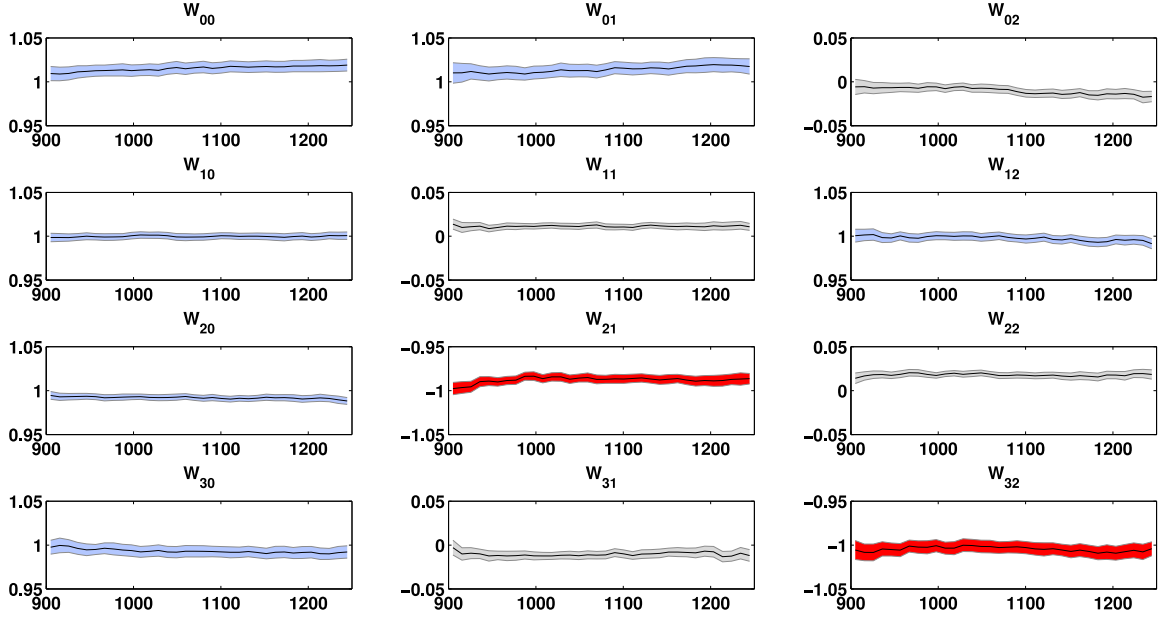


**Figure 31. Spectral plot of the system matrix,  $W$ , after spatial averaging. The standard deviation is represented with the shaded bands around measured values. Since this is a spatial average, the noise is reduced considerably. The scale on this plot is zoomed in to allow better visualization of the noise in the measurements.**

Another interesting result is shown in Figure 32 where each element of the band-averaged Mueller deviation matrix is plotted for each pixel creating a spatial map. The diagonal elements are all close to one and the off-diagonal elements are all close to zero as expected. The checkerboard pattern seen in the off-diagonal elements is believed to be due to non-linear effects in the read out integrated circuitry (ROIC) and represents a current limit on data accuracy. Calibrating this effect out is the subject of a separate, ongoing research effort.

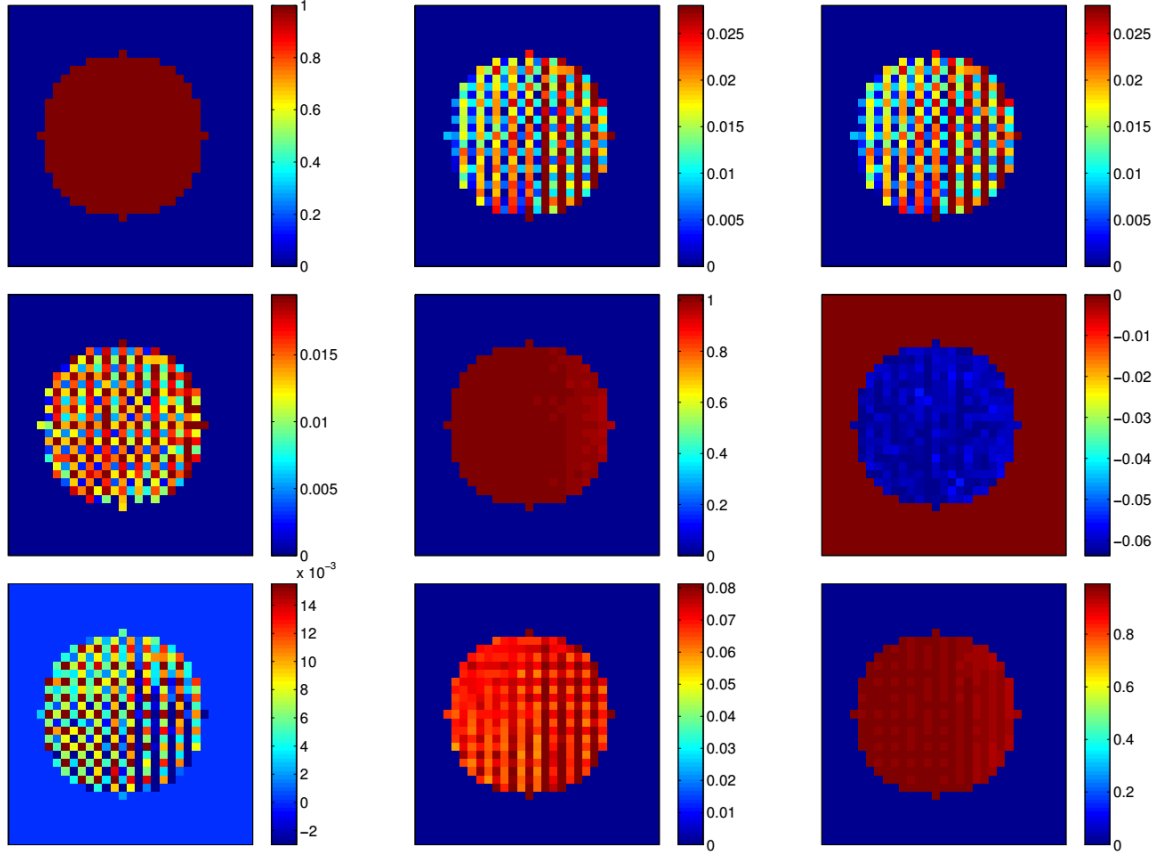


**Figure 32.** Each element of the band-averaged Mueller deviation matrix is plotted for each pixel. The diagonal elements are all close to one and the off-diagonal elements are all close to zero as expected. The checkerboard pattern in the off-diagonal elements is believed to be due to non-linear effects in the read out integrated circuitry (ROIC) and represents a current limit on data accuracy.

### *Calibration Verification on an Unpolarized Source*

Now that the data reduction matrix has been determined experimentally, it is necessary to verify how well the calibration is working under various input states. From here on, the term “uncorrected data” refers to data that has been processed and polarimetrically calibrated under the assumption of an ideal polarizer, and the term “corrected data” refers to the additional correction for the non-ideal polarizer by application of the experimentally determined data reduction matrix. The first verification will measure the system response to unpolarized light. It is important to note here that

the diattenuation of the polarizers has no effect on the system response to unpolarized light. This can be verified by plugging  $s_1 = 0$ ,  $s_2 = 0$ , and  $s_3 = 0$  into Equation (45) (See Chapter V for more details on this equation for the non-ideal polarizer case). The correction, therefore, should have no effect on the measured Stokes vector. To demonstrate this, a blackbody source was used as an unpolarized source to determine whether or not the system showed any polarimetric bias. A 6-inch blackbody was used to flood fill the detector and 200 data cubes were collected for each instrument polarizer angle. On-board blackbody calibration data was also collected at each polarization angle. Each of the 200 data cubes at each angle was then individually calibrated and used to determine the Stokes vector of the incoming light. This was done spectrally on a pixel-by-pixel basis. Then, the spatial and band average of each data cube was taken. This generated an averaged Stokes vector for each of the 200 measurements. Next, the histogram of the 200 Stokes vectors was determined and the normalized  $s_1$  and  $s_2$  distributions were plotted. For each histogram, a normal distribution curve was fitted to the data. The results are shown in Figure 33. The plot shows that the mean of  $s_1$  and  $s_2$  are  $8.6 \times 10^{-4}$  and  $7.6 \times 10^{-4}$ , respectively, for the uncorrected data. The corrected data is also plotted and lines up almost on top of the uncorrected data as expected. Ideally, both  $s_{1_m}$  and  $s_{2_m}$  would be zero for unpolarized light. In this case, there appears to be a very small positive bias on both  $s_{1_m}$  and  $s_{2_m}$ . It is not clear exactly what is causing the bias; however, some possibilities include non-stable target or calibration blackbody sources or the non-linearity of the detector. As mentioned before, the 6-inch blackbody source has a temperature stability of  $\pm 0.5$  °C. To determine if this was a possible

candidate for the bias, a simulation was run to determine the temperature drift that would be required between measurements at orthogonal polarizer angles to produce this bias. The results of the simulation showed that a temperature difference of  $0.5^{\circ}\text{C}$  between orthogonal measurements produces a band-averaged bias of approximately  $8.6 \times 10^{-4}$ . This is, therefore, a feasible source of the bias. Since this is an important source of uncertainty introduced by the experimental setup, the thermal stability of the 6-inch blackbody was independently verified rather than relying on the manufacturer's specification. The results in Figure 34 show that the 6-inch blackbody is indeed oscillating approximately  $0.5^{\circ}\text{C}$  about the set point every 1.2 minutes.

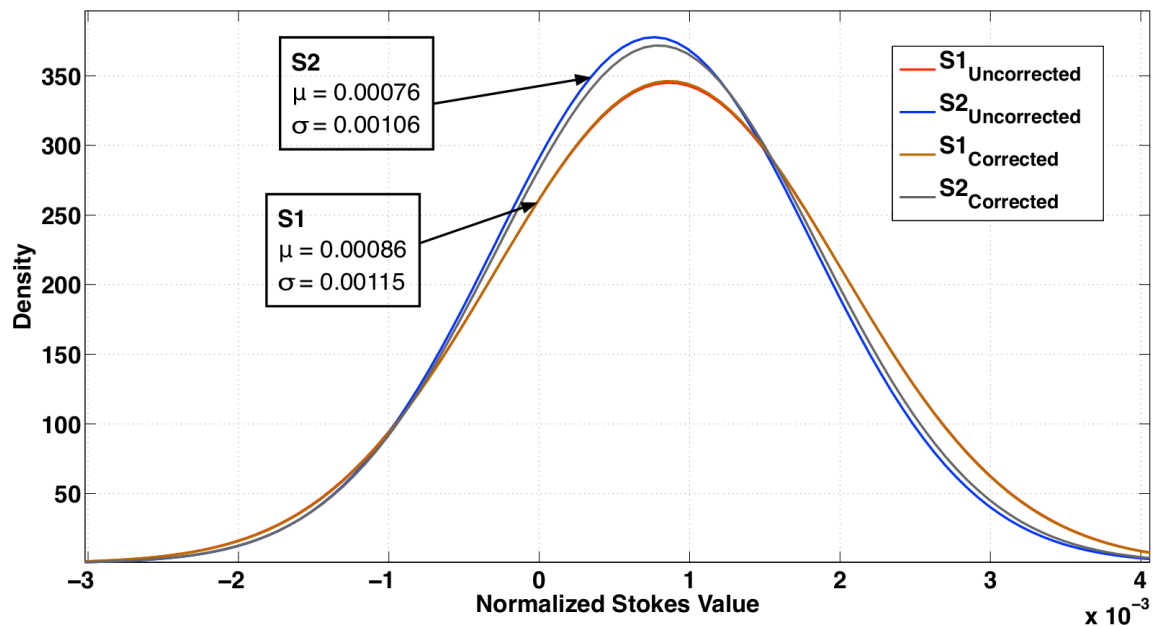


**Figure 33. Histogram of  $s_1$  and  $s_2$  Stokes elements for 200 measurements of blackbody radiation. The histograms are fitted with a normal distribution curve. In the ideal case, the mean of  $s_1$  and  $s_2$  would be zero. This shows that there is a small bias in the measurements, possibly to unstable blackbody sources or the non-linearity of the detector.**

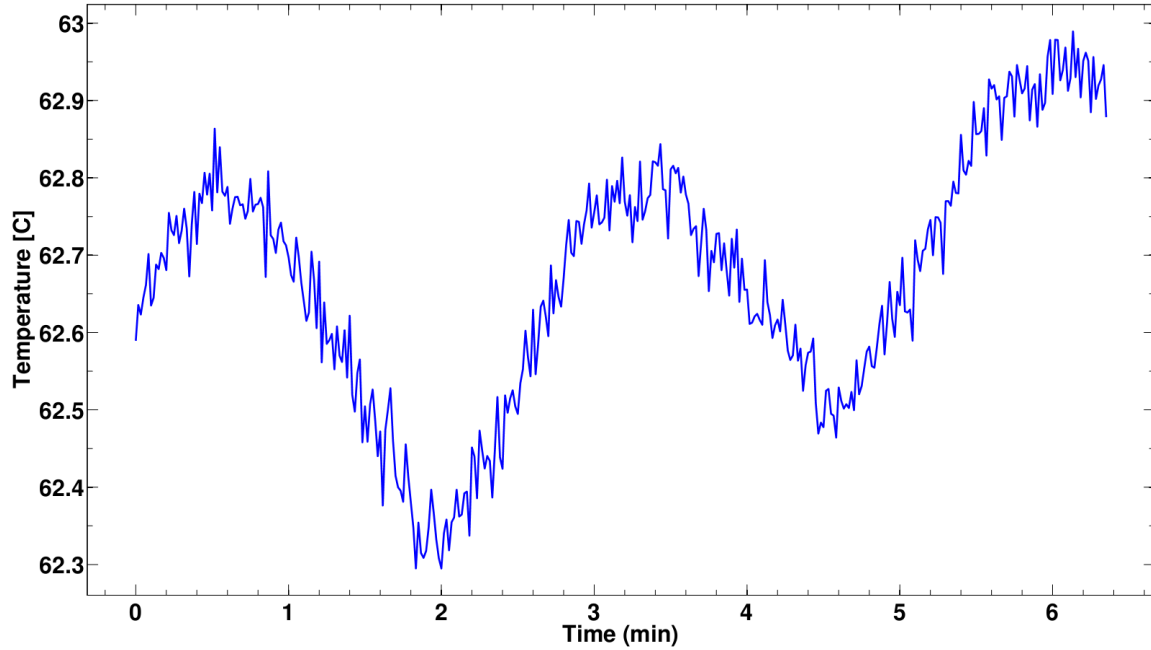


**Figure 34.** Temperature stability of the 6-inch blackbody over a period of just more than 6 minutes. This verifies that the temperature is oscillating approximately 0.5 °C with a period of less than 1.5 minutes.

### *Calibration Verification on Polarized Sources*

Now, how well this experimentally determined matrix is able to correct for the non-idealities of the system is explored when polarized light is input. The band-averaged extinction ratio of the Hypercam polarizer is approximately 400. This gives a diattenuation of

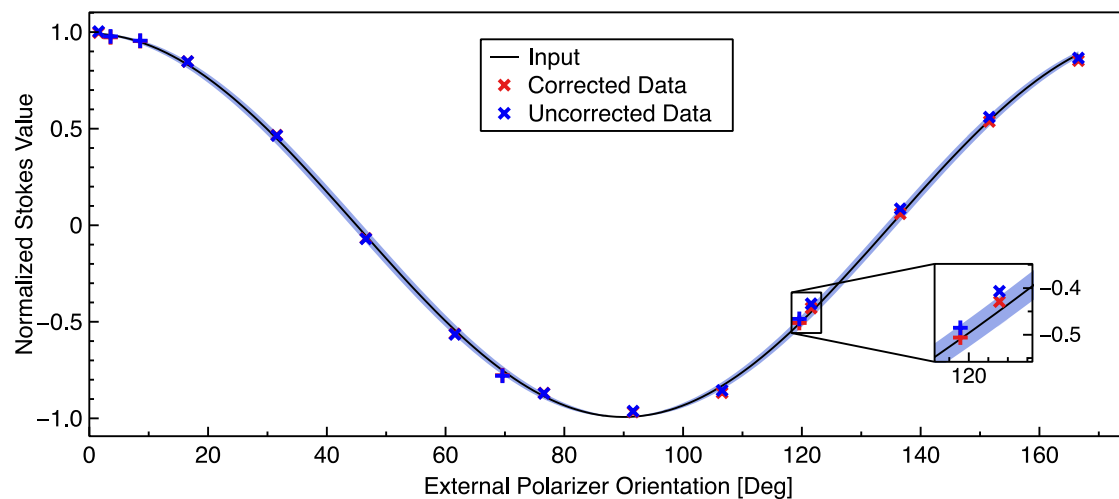
$$D_{pol} = \frac{R-1}{R+1} = \frac{400-1}{400+1} = 0.995 .$$

This means that the uncorrected polarimetric calibration should achieve results on the order of 0.5% from the ideal case if noise and other uncertainties have been sufficiently reduced. To evaluate the effectiveness of the correction on polarized light, the measured Stokes parameters output from the system were compared to the input Stokes vectors for both the uncorrected case and the corrected case. The spatially and spectrally averaged

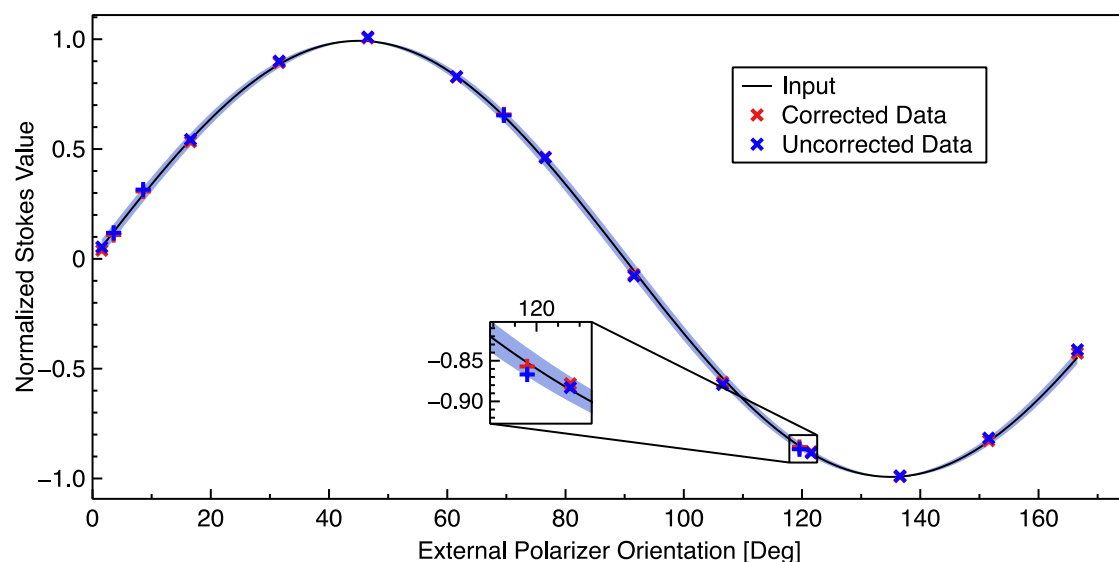
results are shown in Figure 35. In each plot, the solid line shows the input Stokes value as a function of external polarizer orientation and the shaded band represents the uncertainty in the external polarizer orientation. The blue markers are for the uncorrected data and the red markers are for the corrected data. The ‘x’ markers are at the calibration points and the ‘+’ markers are in-between calibration points. It is difficult to visually tell the difference between the corrected and uncorrected data from the plots, which again confirms that the polarimetric calibration under the ideal polarizer assumption works very well. To see the effect of the correction, a zoomed in view is shown for a specific data point. Now it can be seen that the corrected data is closer to the input line than the uncorrected data for that specific data point.

To visualize the spectral behavior of the measured Stokes values, both on a spatially averaged and a pixel-by-pixel basis, Figure 36 shows a 3-D plot of the data matrix. The two plots on the left show the measured values of  $s_1$  and  $s_2$  for one pixel and the plots on the right show the measured values of  $s_1$  and  $s_2$  for a spatial average of 317 pixels. The results indicate that, while there is some noise in the measured values of one pixel, the measured Stokes values are flat spectrally. This is clear on the averaged data. Note that Figure 36 only shows the uncorrected data; however, as in Figure 35, it is hard to discern any visual difference between the corrected and uncorrected data in these plots.



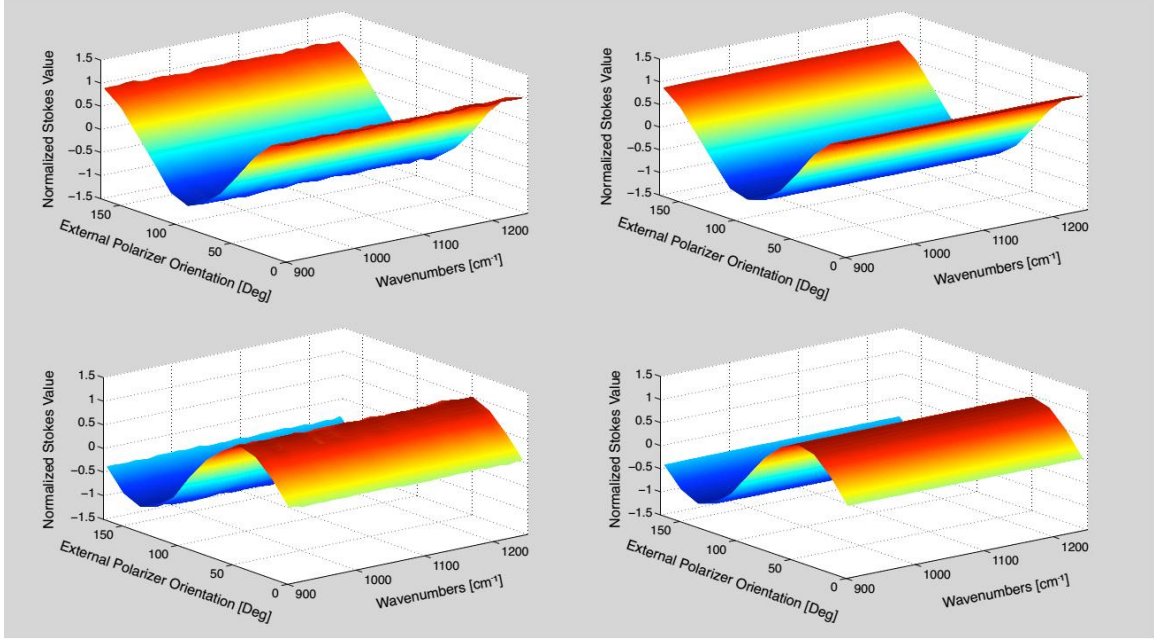


a.)



b.)

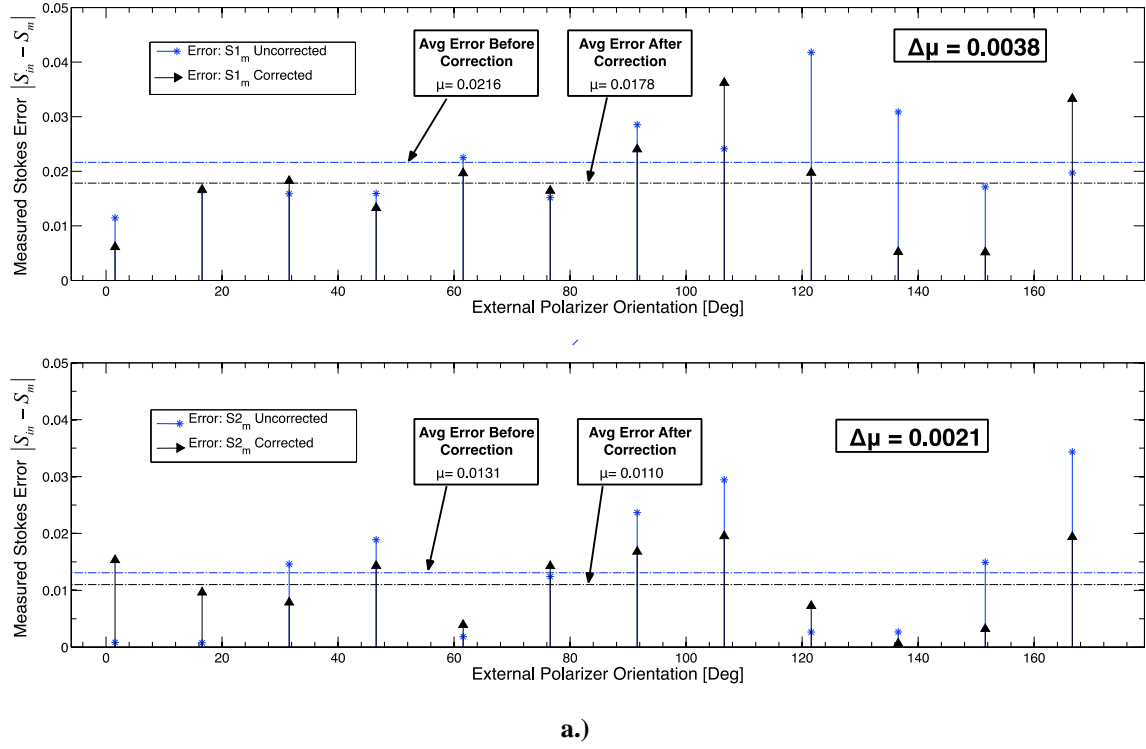
**Figure 35. Comparison of the measures Stokes values for the corrected and uncorrected data for a.)  $s_1$  and b.)  $s_2$ . The solid line is the input Stokes values with a shaded band representing the uncertainty in the external polarizer orientation.**

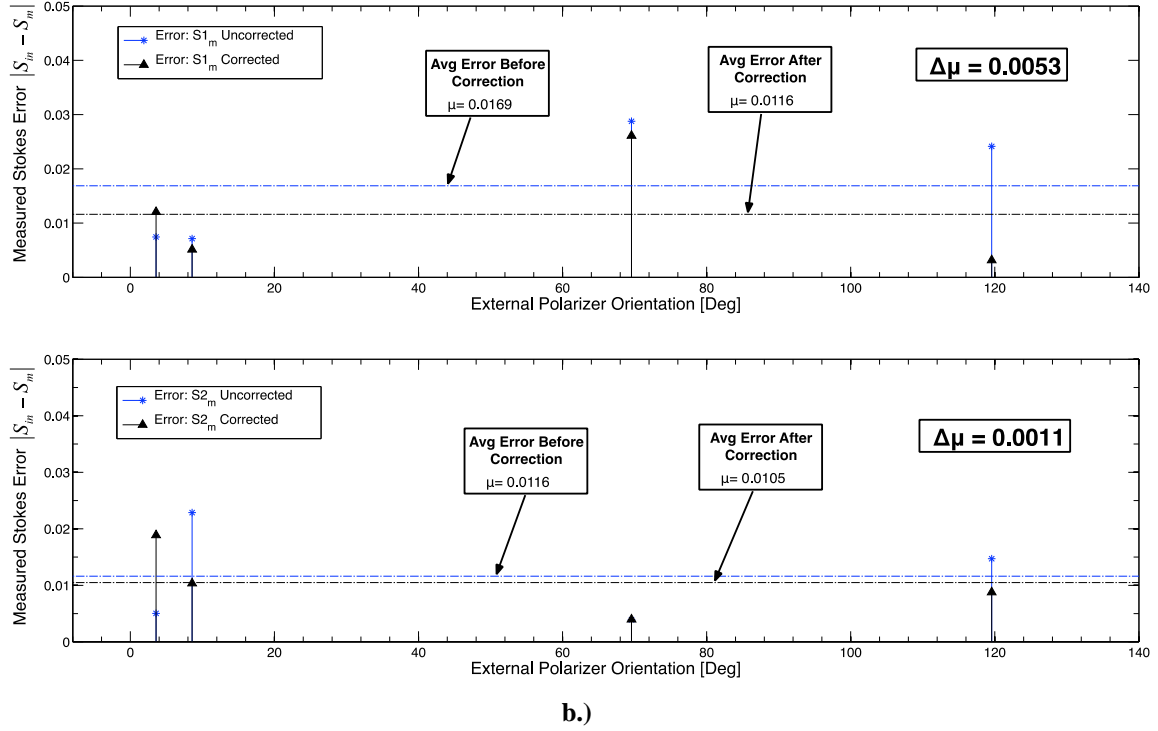


**Figure 36.** Shows the spectral nature of each of the 12 measurements for a single pixel (left) and for 317 spatially averaged pixels (right). The top plots are  $s_1$  and the bottom plots are  $s_2$ .

To further analyze the performance of the correction, the error between the measured data and the input values are calculated for both the corrected and uncorrected data. In this case, the data at the calibration points are plotted separately from the data taken in-between calibration points. This helps to understand how much error is in the least squares solution at the calibration points. Figure 37 shows these results. In all cases, the correction reduced the average error although there are still points where the corrected data has a greater error than the uncorrected data. The data shows that on a spatially and band averaged basis, the correction improves the error by 0.5% or less and that there is a residual error ranging from approximately 1-2% even after calibration. The primary cause of the residual error is likely to be the thermal drift of the 6-inch blackbody as discussed in the previous section. The correction of 0.5% is consistent with the fact

that the instrument polarizer is within about 0.5% of an ideal polarizer based on its diattenuation.

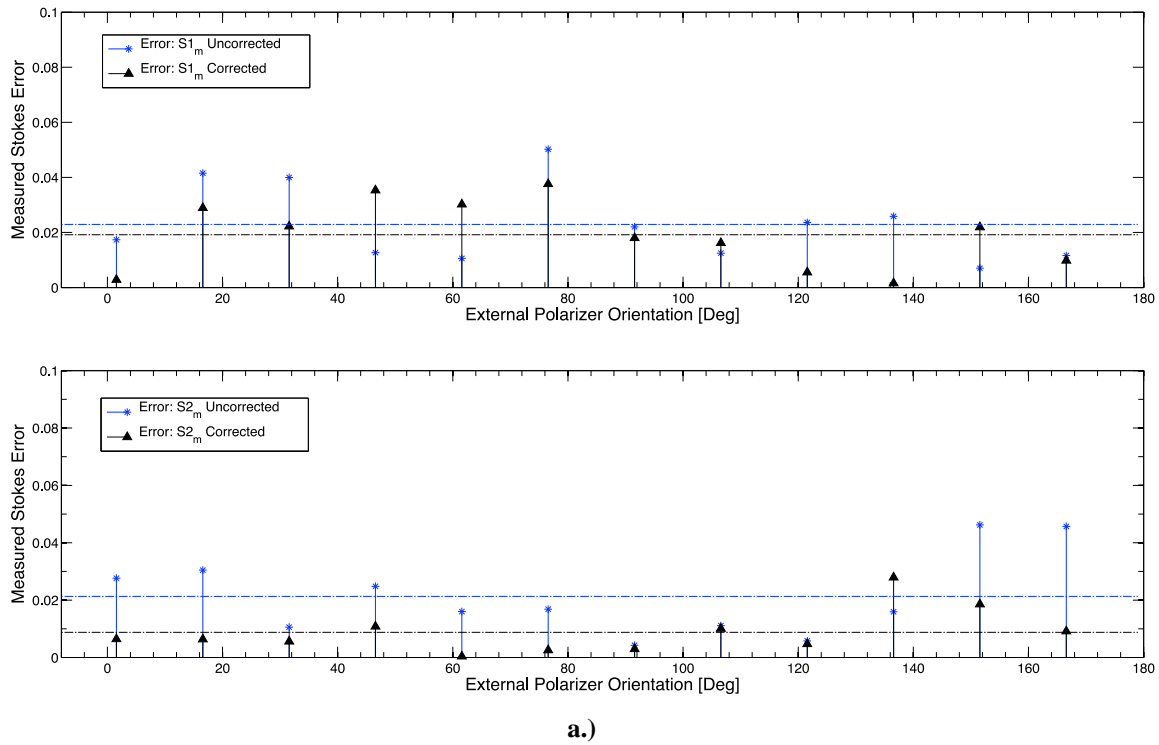


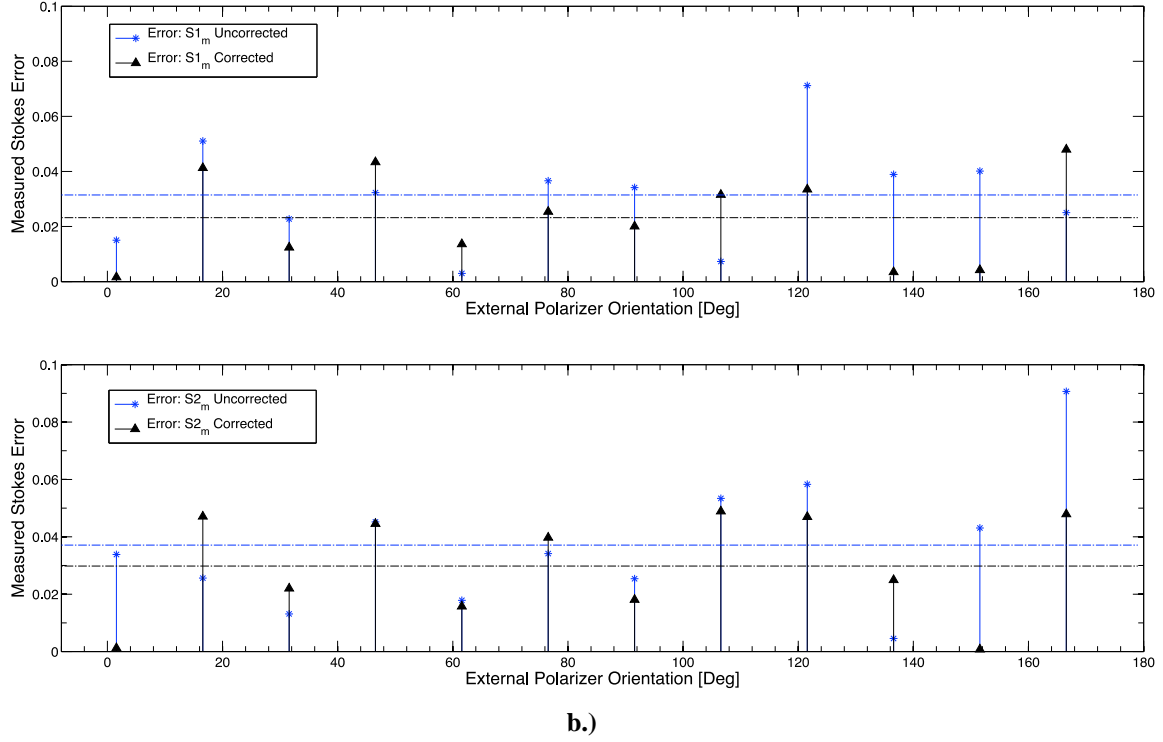


**Figure 37. a.) Error between the measured data and the input data both before and after correction at the 12 calibration points. b.) Error for the data collected in-between the calibration points.**

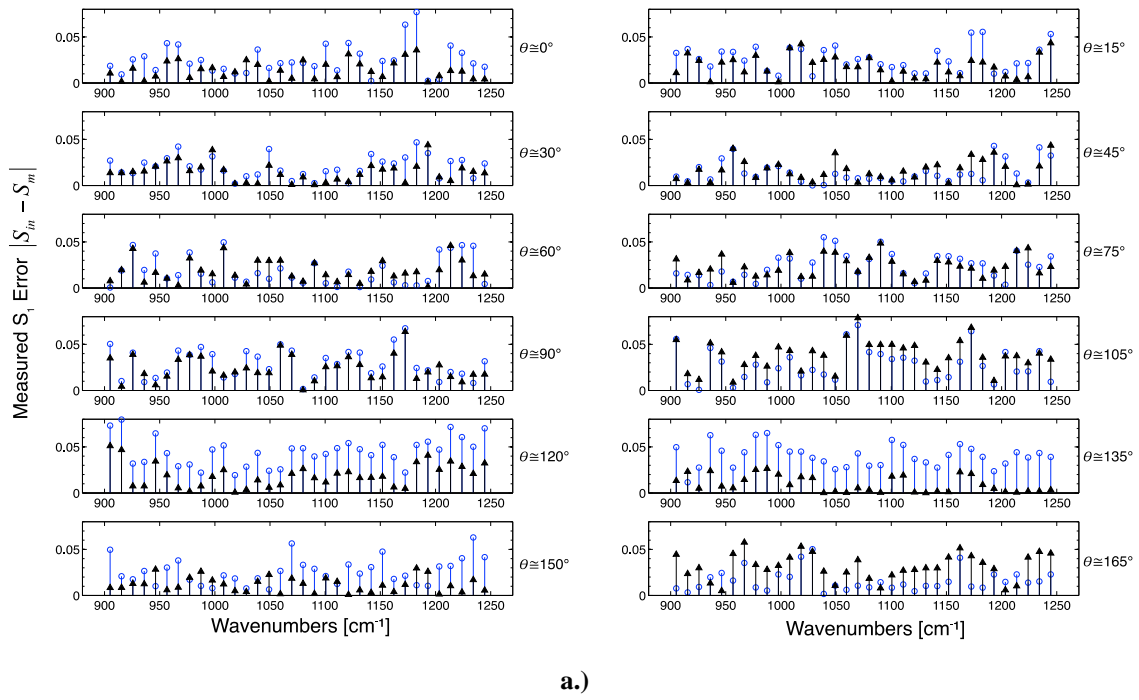
Next, the same error plots are shown in Figure 38 for an individual pixel at two individual bands, one near the middle of the bandwidth and one near the edge of the bandwidth where the SNR is slightly decreased due to the sensor's sensitivity. As expected, the average error increases, now ranging from roughly 1-4%; however, on average, the error after correction is less than the error before correction for both  $s_1$  and  $s_2$ . To gain a better understanding of the error of one pixel across the entire bandwidth, Figure 38 shows the error of the same pixel plotted spectrally for each of the 12 measured Stokes vectors before and after correction for  $s_1$  and  $s_2$ . Additionally, since there will likely be some spatial averaging done during post-processing for a typical scene, Figure 39 shows the spectral error for 317 spatially averaged pixels. The results show that on an

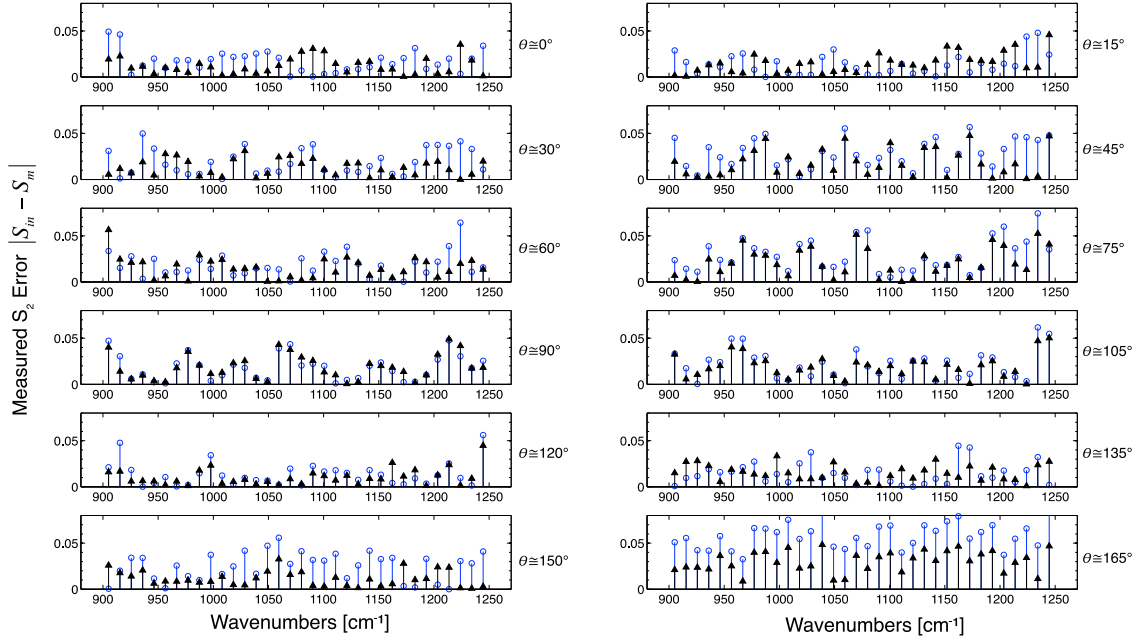
individual pixel basis, the error of the corrected data tends to stay either above the uncorrected error for the entire band or below the uncorrected error for the entire band without jumping back and forth too much. On a spatially averaged basis this trend is even stronger since the error flattens out considerably across the band. The average error across the band is also reduced. In order to aid visual comparison between the individual pixel results and the averaged pixel results, they were both plotted on the same scale. Notice that in all of the error plots shown below, there appears to be a sinusoidal oscillatory nature to error magnitude. It is speculated that this oscillatory nature in the error, is again related to the oscillatory thermal fluctuations of the 6-inch blackbody shown in Figure 34.





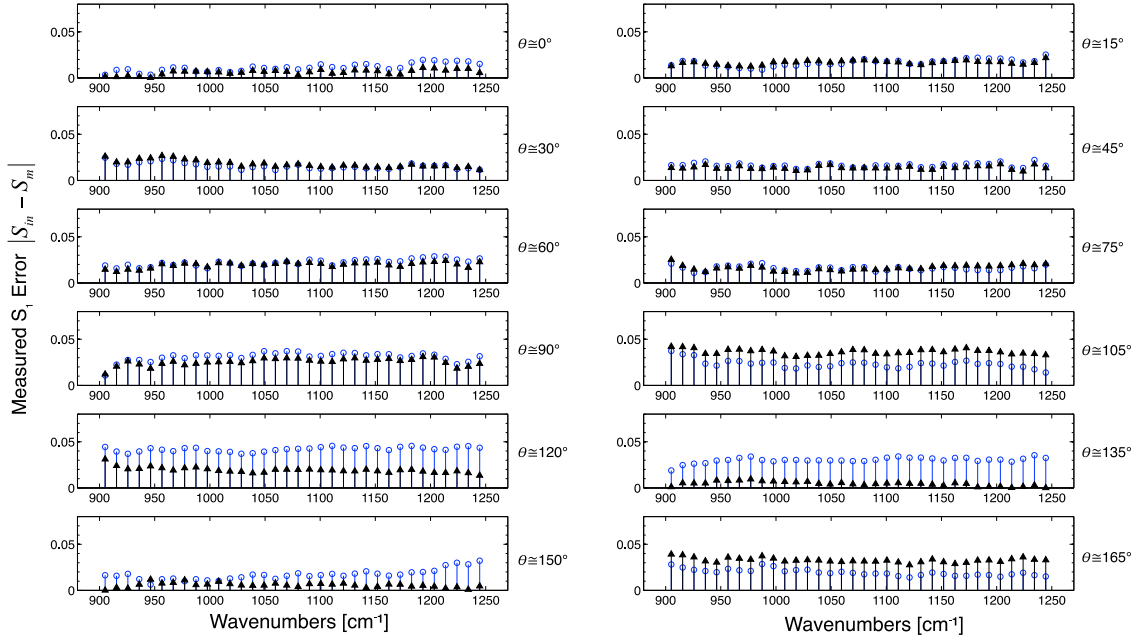
**Figure 38.** Error of the measured data for an individual pixel at a.) near the center of the bandwidth and b.) near the edge of the bandwidth where detector sensitivity is slightly decreased.





b.)

**Figure 39. Shows the measured spectral error for one pixel for a.)  $s_1$  and b.)  $s_2$  for each of the 12 input Stokes vectors. The label to the right of each plot indicates the orientation of the external polarizer.**



a.)

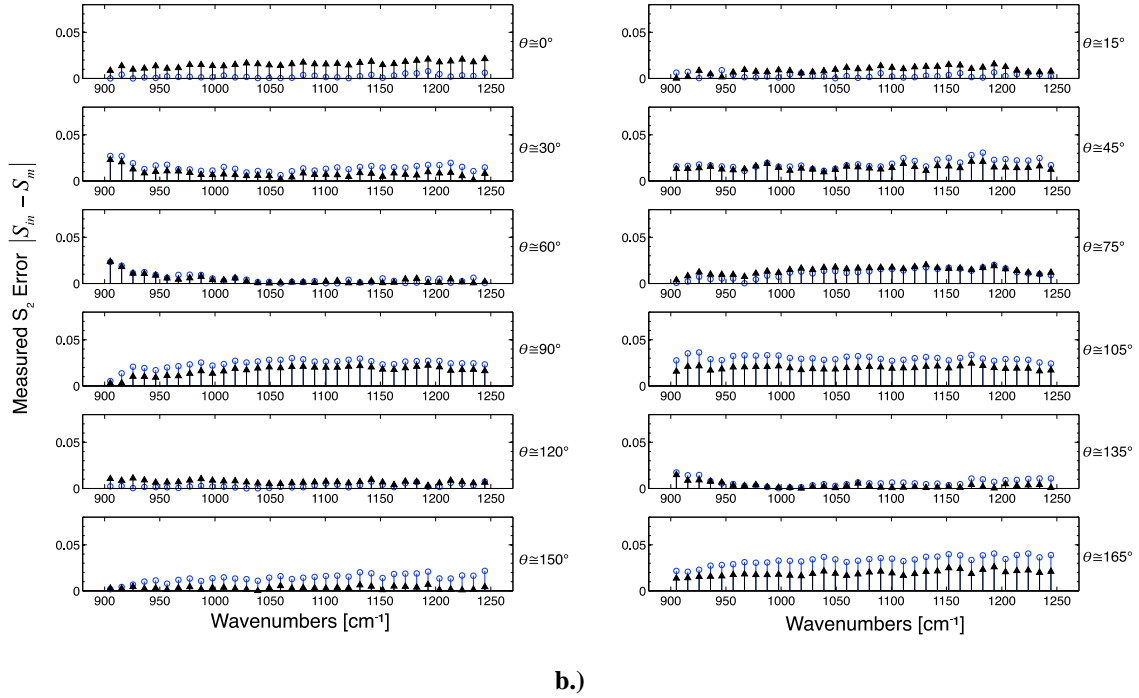


**Figure 40.** Shows the measured spectral error of 317 spatially averaged pixels for a.)  $s_1$  and b.)  $s_2$  for each of the 12 input Stokes vectors. The label to the right of each plot indicates the orientation of the external polarizer.

### *Noise and Error Analysis*

Next, it is important to quantify the noise in the measurements in order to gain further insight into the error results shown above. Theoretically, if the noise in the measurements was zero and the detector was perfectly linear, then the polarimetric calibration correction should perfectly correct the measured Stokes vectors back to the known input Stokes vectors. The more random noise in the measurements and the more non-systematic errors, the worse the least squares solution is going to be and the worse the polarimetric calibration is going to perform. Unfortunately, the SNR for this experiment is forced down by the fact that the hot and cold collections are differenced. This differencing effectively reduces the signal while increasing the random noise.



Some typical noise sources include photon shot noise, shot noise from the dark current, Johnson noise, preamplifier noise, and quantization noise [28]. Additional sources of noise that are introduced by the limitations of the experimental setup include random error when setting the external polarizer angle, random fluctuations of the external blackbody sources, and random or inconsistent thermal fluctuations in the external polarizer between hot and cold measurements. In addition to these random noises, systematic errors can exist which will bias the data in the same way for each measurement. Sources of possible systematic error include the uncertainty in determining the absolute zero-angle of the external polarizer and the uncertainty in the spectral diattenuation of the external polarizer. Thermal drift of the external polarizer could also be considered a systematic error if the thermal drift was constant and affected each measurement the same way. A systematic error in the external polarizer angle will result in a horizontal shift of the input Stokes vector in Figure 35 and other similar plots, and will cause the calculated error before correction to be artificially high. An error in the diattenuation of the external polarizer will result in a vertical scaling of the input Stokes vector and will cause the corrected Stokes values to be scaled by the ratio of the measured diattenuation to the true diattenuation. Thermal drift of the external polarizer between hot and cold measurements could cause artificially high or low measured values for  $s_1$  and  $s_2$ . For the error analysis, the relative systematic error due to an incorrect determination of the external polarizer zero-angle is assumed to be zero since it was removed by fitting a sinusoid to the uncorrected measurements and correcting for the phase shift between the input Stokes vector and the fitted sinusoid. Therefore, the

relative error before the correction is a result of random error/noise and the assumption of an ideal polarizer. The correction should then remove the assumption of an ideal polarizer and leave only error due to random noise, detector non-linearity, and the thermal fluctuations of the 6-in blackbody discussed before. This means that the random noise in the measurements of the input Stokes vectors (after frame averaging) must be smaller than the error due to the assumption of an ideal polarizer in order to have a definitive effect. If this is not true, then the uncertainty in the solution of the system matrix will be larger than the 0.5% correction it is attempting to make. It was already shown in Figure 31 that the noise in the measurement of the system matrix elements ranged from 0.35-0.77%. Therefore, it will be difficult to make a 0.5% correction unless the noise is further reduced. Additionally, the noise statistics of  $s_1$  and  $s_2$  must be used to compare to the error reported for  $s_1$  and  $s_2$  earlier. This is shown in Figure 41. The noise ranges from around 1-2%. This noise can account for some of the residual error after calibration.

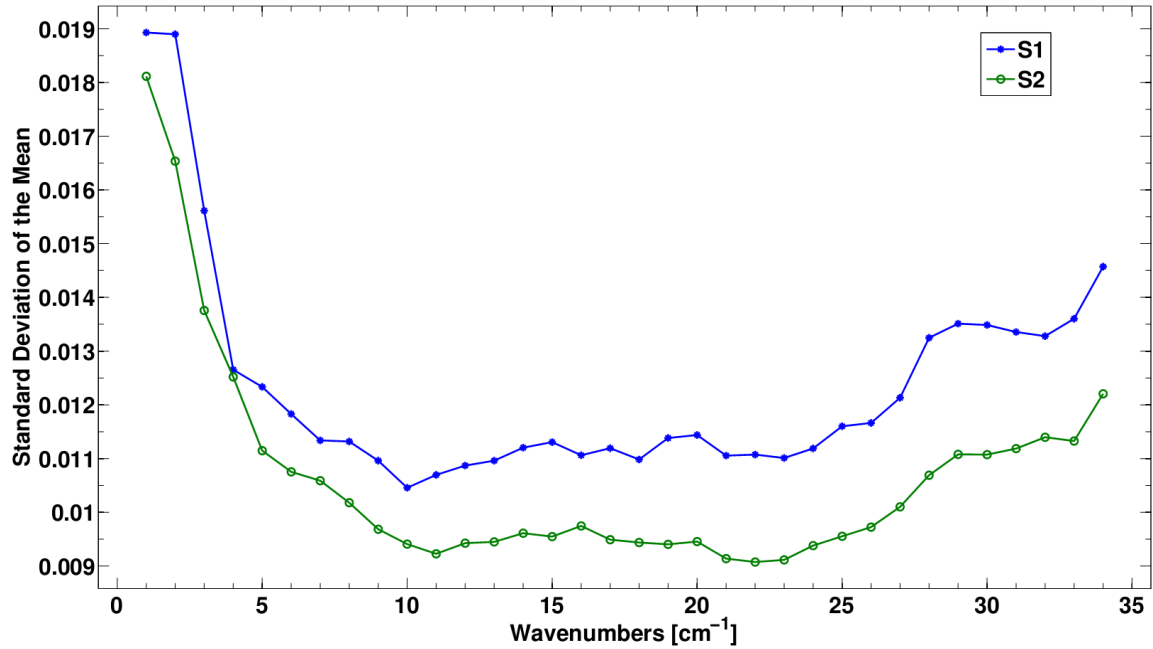


**Figure 41.** Spectrally resolved noise of the  $s_1$  and  $s_2$  measurements when viewing horizontally polarized light. The noise was determined by taking the standard deviation of the mean for the 64 frames acquired at each band.

### NESR and NESDoLP of an Unpolarized Source

In addition to trying to correct for the non-ideal nature of the instrument polarizer, there was also a desire to understand what the noise equivalent spectral radiance (NESR) and noise equivalent DoLP (NESDoLP) of the system are.

To determine the NESR from experimental data, a 45 °C blackbody was placed in front of the Telops so that the full detector array was flood filled. The integration time was set to 200  $\mu$ s and the spectral resolution was 16  $\text{cm}^{-1}$ . The blackbody source provides the ideal condition to measure the NESR since the temporal variations of the scene radiance are negligible with a well-controlled blackbody [3]. Next, 200 data cubes were collected at each of the four standard instrument polarizer angles (0°, 45°, 90°, and 135°). A radiometric calibration was performed at each of the instrument polarizer angles and bad pixels were removed. The NESR is then determined for each pixel by

calculating the temporal standard deviation of the measured radiance at each waveband. The pixel average of the measured NESR for each instrument polarizer angle is shown in Figure 43. The NESR values measured are consistent, although slightly lower, than the NESR values reported by Telops in [3]. It makes sense that the values are lower since the values reported by Telops were for a  $4 \text{ cm}^{-1}$  resolution as opposed to a  $16 \text{ cm}^{-1}$  resolution and NESR increases with higher spectral resolution [2]. It is believed that the difference between the NESR at  $0^\circ$  and  $90^\circ$  is due to the non-linearity of the detector response. This difference, however, had little effect on the calibration's ability to normalize the system response since the SNR is greater than 100 across the band. This can be shown in Figure 42 where the radiance measured by the detector at each instrument polarizer angle is plotted. There is very little deviation between the measured radiance at each polarizer angle.

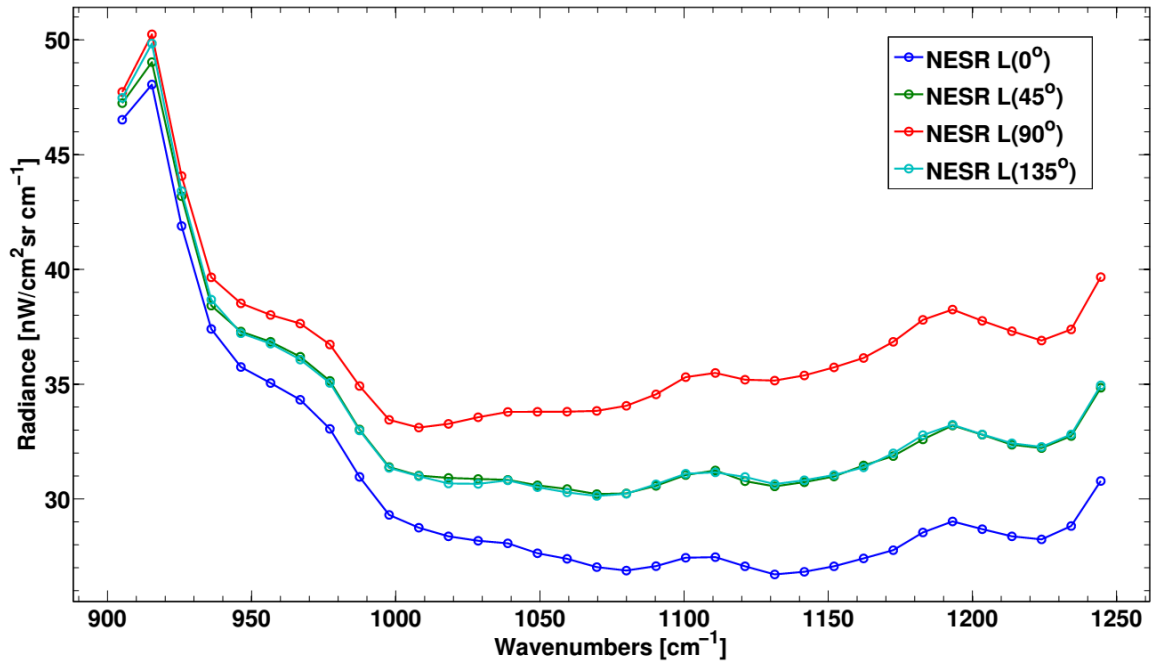


Figure 42. Measured NESR of the Telops instrument at each polarizer angle.

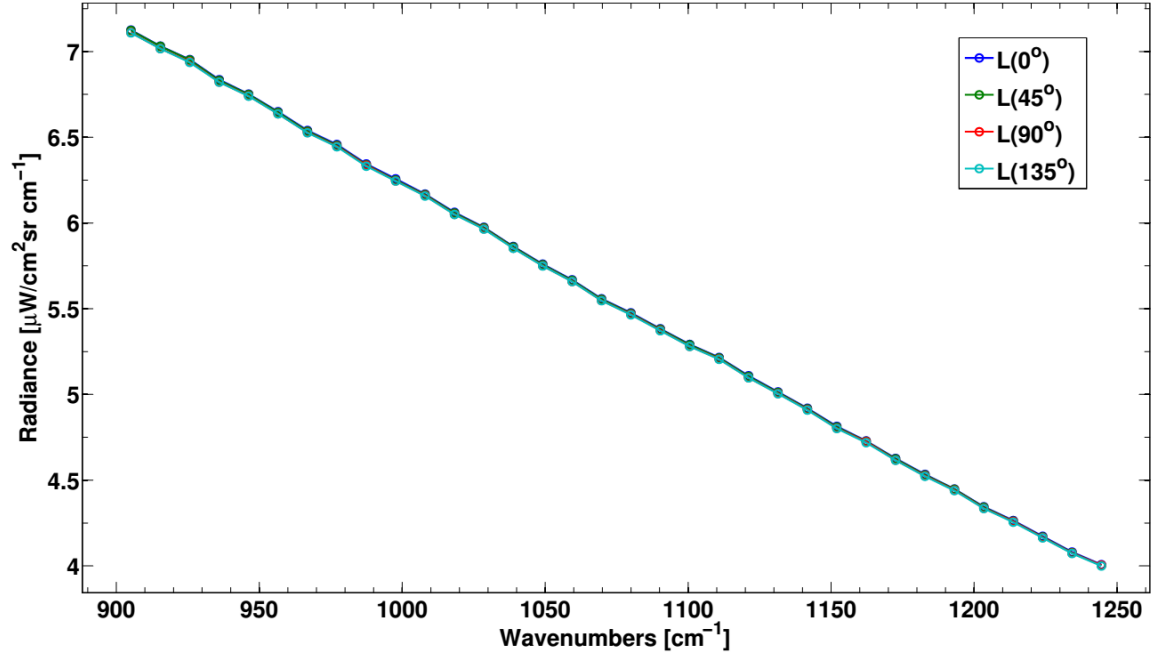


Figure 43. Measured radiance when viewing an unpolarized blackbody source at each instrument polarizer angle after calibration.

Next, the NESDoLP is determined. The NESDoLP is effectively the minimum DoLP the system can discern and is based on the noise in the measurement of  $s_1$  and  $s_2$ . Recall that DoLP is given by

$$\text{DoLP} = \sqrt{s_1^2 + s_2^2}, \quad (86)$$

where in this case,  $s_1$  and  $s_2$  have already been normalized by  $s_0$ . This means that the accuracy in the measurement of DoLP can never be better than the propagated uncertainty in  $s_1$  and  $s_2$ . The propagation of uncertainty of Equation (86), and therefore the NESDoLP, is given by

$$\text{NESDoLP} = \sqrt{\left(\frac{\partial \text{DoLP}}{\partial s_1} \delta s_1\right)^2 + \left(\frac{\partial \text{DoLP}}{\partial s_2} \delta s_2\right)^2} \quad (87)$$

which gives

$$\text{NEDoLP} = \sqrt{\left( \frac{s_1}{\sqrt{s_1^2 + s_2^2}} \cdot \delta s_1 \right)^2 + \left( \frac{s_2}{\sqrt{s_1^2 + s_2^2}} \cdot \delta s_2 \right)^2} \quad (88)$$

where  $\delta s_1$  and  $\delta s_2$  are the temporal standard deviation of  $s_1$  and  $s_2$ . Doing this at each pixel and at each waveband generates the spectrally resolved NEDoLP, or the noise equivalent spectral DoLP (NESDoLP) given by

$$\text{NESDoLP}(i, j, \sigma) = \sqrt{\left( \frac{s_1(i, j, \sigma) \cdot \delta s_1(i, j, \sigma)}{\sqrt{s_1^2(i, j, \sigma) + s_2^2(i, j, \sigma)}} \right)^2 + \left( \frac{s_2(i, j, \sigma) \cdot \delta s_2(i, j, \sigma)}{\sqrt{s_1^2(i, j, \sigma) + s_2^2(i, j, \sigma)}} \right)^2} \quad (89)$$

where  $i$  is the pixel row index,  $j$  is the pixel column index, and  $\sigma$  is the spectral dependence on wavenumbers.

Further insight into the actual system parameters that determine NEDoLP is provided by Jones and Persons. In their paper (Ref [27]), they derive a model for the NEDoLP of a micro-grid polarimeter. This model is useful in understanding the system parameters which affect the NEDoLP. Their model for NEDoLP is given by

$$\text{NEDoLP} = \frac{\sqrt{1 + 2\delta - 2\delta\beta + D^2 \text{DoLP}^2 \left( \frac{1+\delta}{2} - \beta \left( 1 - \frac{\delta}{2} \right) \right)}}{\beta D \sqrt{n}} \quad (90)$$

where  $\delta$  is the ratio of read noise to shot noise,  $\beta$  is the ratio of signal electrons accumulated in the well to total electrons accumulated in the well,  $D$  is the diattenuation of the polarizer, and  $n$  is the well capacity. From this, the following observations can be made: First, if the read noise is significant compared to the shot noise, then NEDoLP is degraded. Second, the NEDoLP is improved with a larger well size of the FPA so the

polarimetric performance will benefit from a large well capacity. Third, a better SNR will improve NEDoLP. Finally, a more ideal polarizer will improve the NEDoLP.

In order to experimentally determine the NESDoLP, the same dataset from the NESR determination was used. The NESDoLP was calculated for each pixel at each waveband using Equation (89). This was done for both the corrected and uncorrected data. As demonstrated in the "Calibration Verification on Unpolarized Source" section, if the detector non-linearity is small and the calibration sources are stable, the correction should have little effect on unpolarized light, and therefore the NESDoLP should be the same for the corrected and uncorrected data. The pixel average of the NESDoLP for the corrected and uncorrected data is shown in Figure 44. As expected, the corrected and uncorrected data give the same results. The NESDoLP ranges from 0.32% to 0.55% across the band. There are a few things to keep in mind here. First, this is the NESDoLP for one measurement. If  $N$  measurements are averaged then the NESDoLP is improved by

$$\text{NESDoLP}' = \frac{\text{NESDoLP}}{\sqrt{N}}. \quad (91)$$

Second, the NESDoLP will change depending on the SNR in the measurements. Third, this assumes that all other error has been removed and that the only remaining uncertainty in the measurement comes from the random noise. Assuming that the blackbody is randomly polarized, the calculated DoLP should be approximately the same as the NESDoLP. If this is not true, then some other error or uncertainty other than random noise remains in the measurements. Figure 45 shows the spectral DoLP plotted with the NESDoLP. Since the measured DoLP is larger than the NESDoLP, there appears to be

some uncertainty in the measurements which has not been removed. The figure shows that on average the DoLP errors are approximately 0.12% larger than what the NESDoLP predicts. This again, could be due to blackbody sources that are fluctuating slightly or it could be due to the non-linearity of the detector. It has been shown that the ability to measure low DoLP signatures is greatly influenced by the accuracy of the 2-point calibration [29], [30] [31], [25].

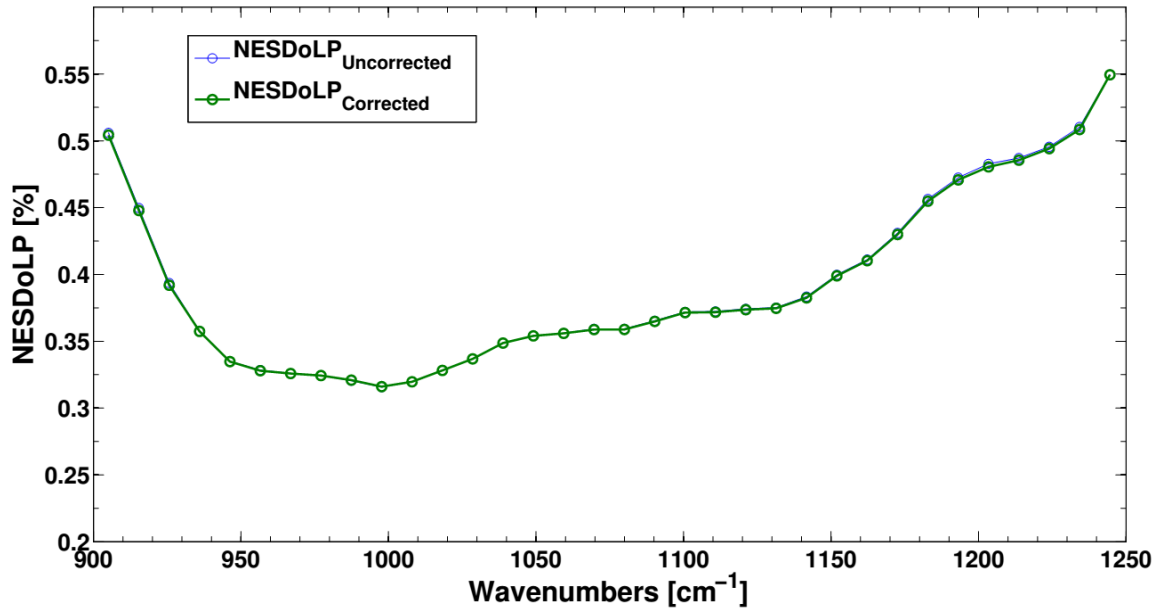


**Figure 44.** Noise equivalent spectral DoLP of the Telops instrument.



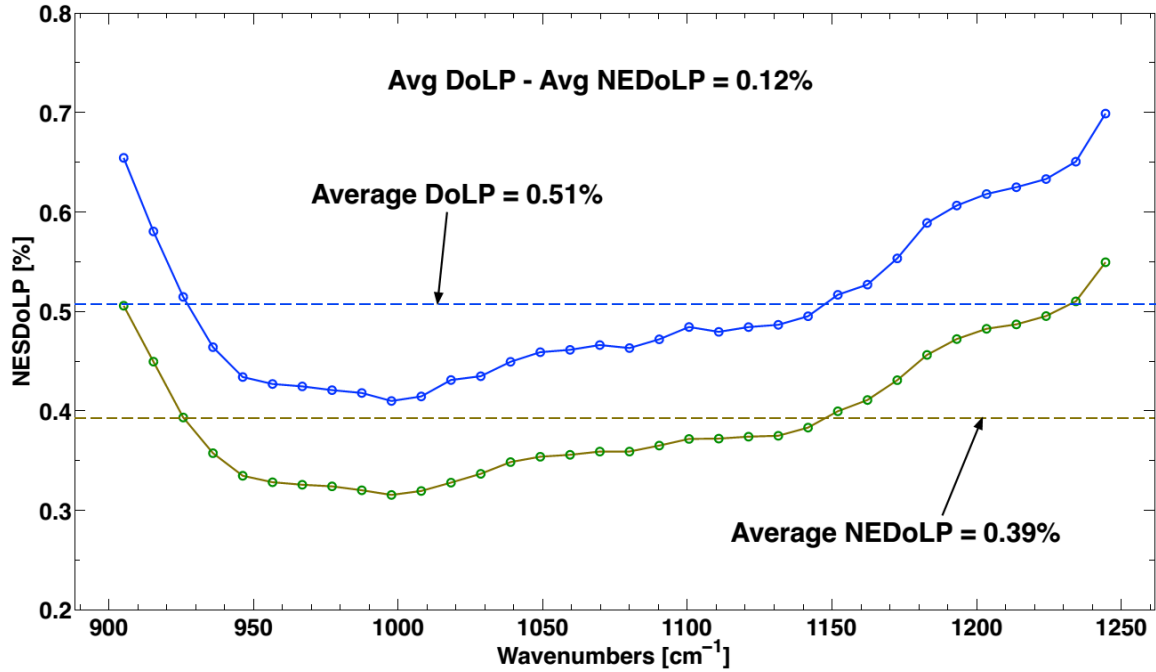


Figure 45. DoLP and NESDoLP plotted together. The DoLP error is approximately 0.12% larger than predicted by the NESDoLP.

### NESR and NESDoLP of a Polarized Source

Now, the exact same plots as above are plotted for a source that is close to horizontally polarized (after fitting a sinusoid to the data, it was actually determined to be polarized at  $1.57^\circ$ ). The horizontally polarized source was generated using the setup shown in Figure 22 and the same differencing method described earlier. One expectation here would be that the correction should now have an effect since polarized light is input into the system. Another expectation would be that the noise has more of an effect on the data because the SNR is much lower due to the differencing. Figure 46 shows the NESR at each instrument polarizer angle. The NESR is roughly the same as it was for the unpolarized source. Figure 47 shows the measured radiance at each instrument polarizer angle. Notice that because of the differencing, the radiance measured at each angle is small compared to the radiance measured for the unpolarized source. Also, the radiance

at  $45^\circ$  and  $135^\circ$  are off slightly due to the  $1.57^\circ$  offset mentioned before. Figure 48 shows the measured DoLP before and after correction. This time the correction improves the DoLP measurement by an average of 0.56%.

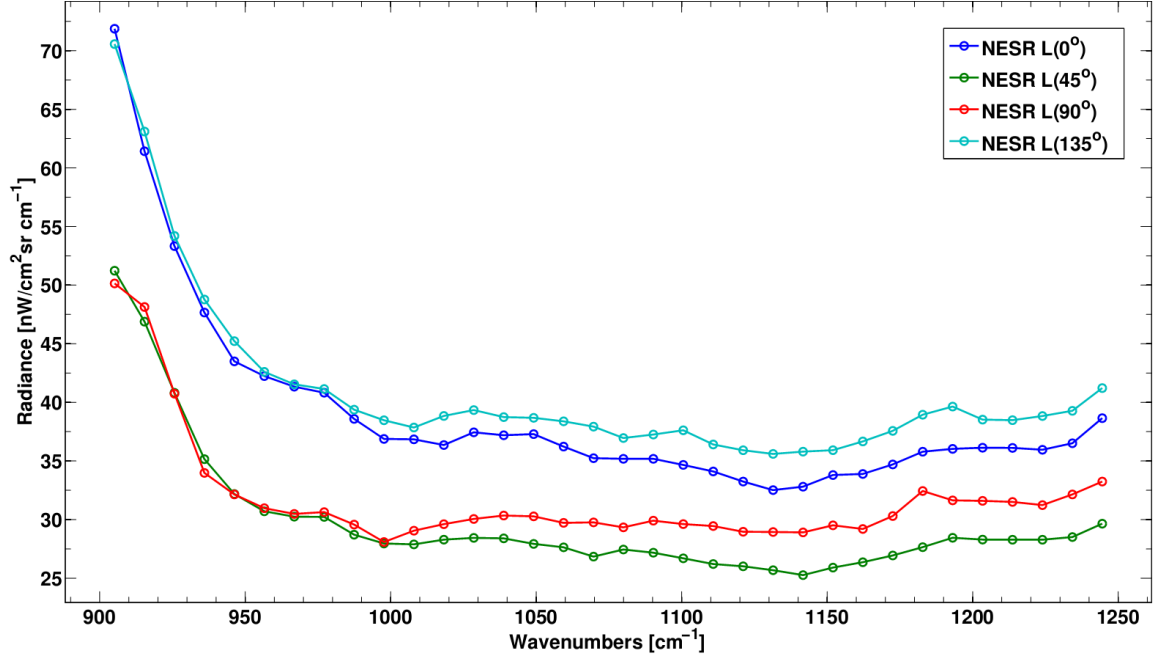


Figure 46. Measured NESR for horizontally polarized light at each instrument polarizer angle.

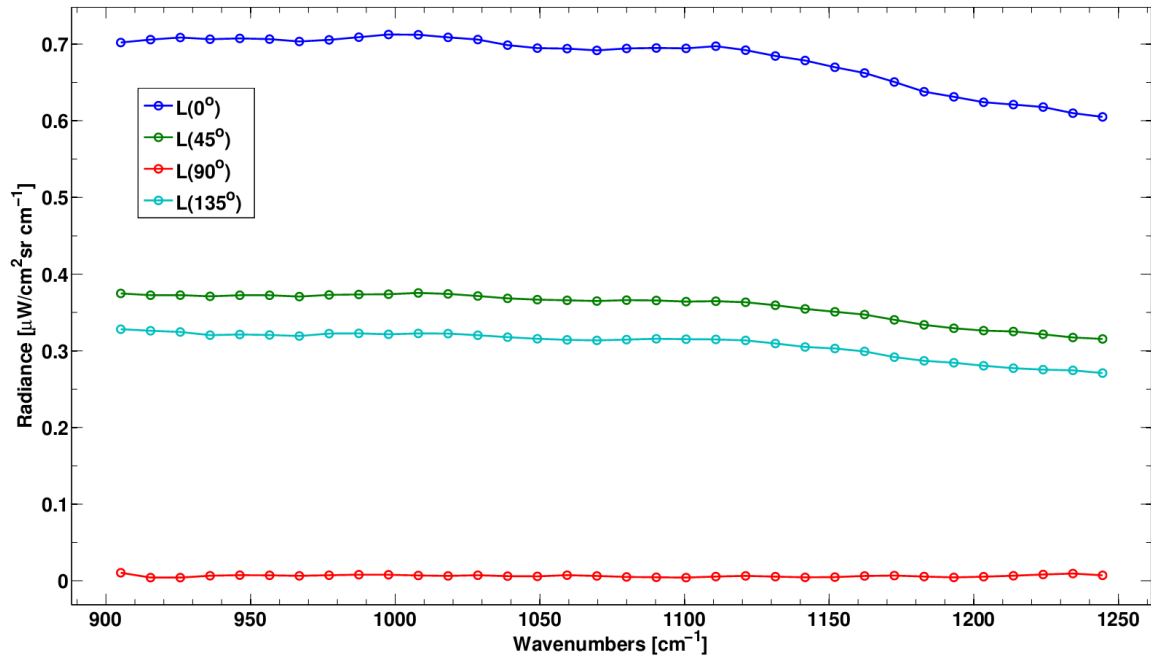


Figure 47. Measured radiance at each instrument polarizer angle for a horizontally polarized source.

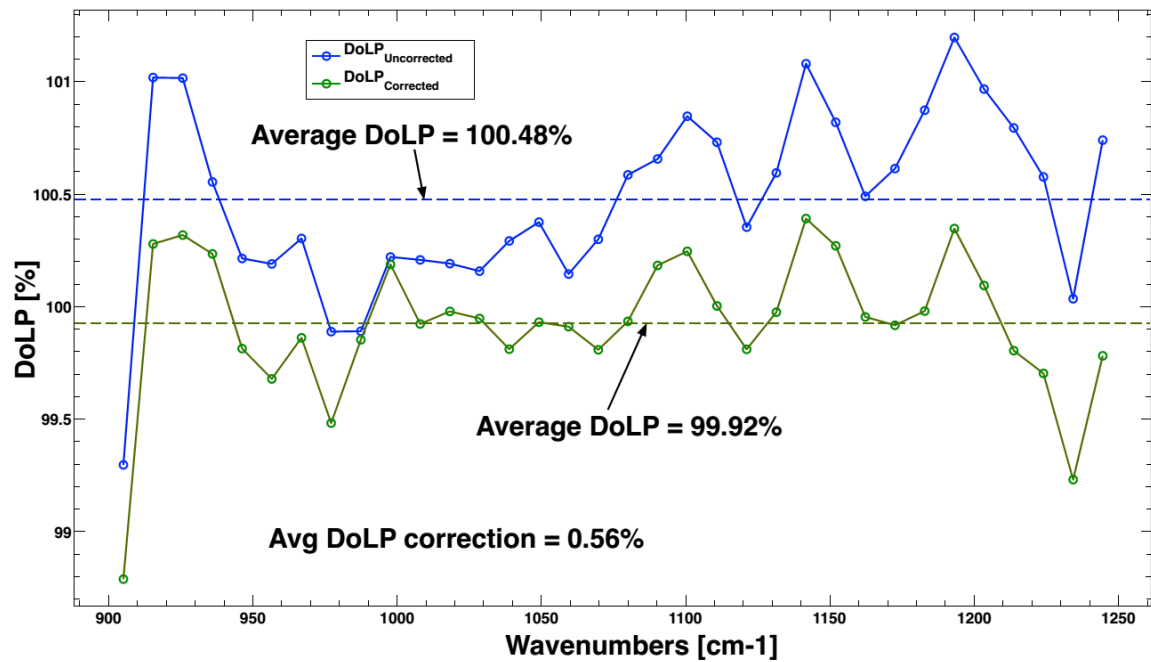


Figure 48. Measured DoLP before and after correction for horizontally polarized light. This time the correction improves the measurement by 0.56% on average.

## V. Polarimetric Performance Modeling

This chapter utilizes the mathematical frame work developed in the previous chapter to analyze the effect of having a non-ideal instrument polarizer and a non-ideal HSI system Mueller matrix. In the previous chapter, the Mueller matrix of an ideal polarizer was used to determine the functional form of  $\hat{m}_{01}(\theta_p)$  and  $\hat{m}_{02}(\theta_p)$  in Equation (44). The functional form of these elements must now be determined using the more general Mueller matrix of a linear polarizer that includes diattenuation. This Mueller matrix is given by

$$\frac{1}{2} \begin{pmatrix} q+r & (q-r)\cos 2\theta_p & (q-r)\sin 2\theta_p & 0 \\ (q-r)\cos 2\theta_p & (q+r)\cos^2 2\theta_p + 2\sqrt{qr}\sin^2 2\theta_p & (q+r-2\sqrt{qr})\sin 2\theta_p \cos 2\theta_p & 0 \\ (q-r)\sin 2\theta_p & (q+r-2\sqrt{qr})\sin 2\theta_p \cos 2\theta_p & (q+r)\sin^2 2\theta_p + 2\sqrt{qr}\cos^2 2\theta_p & 0 \\ 0 & 0 & 0 & 2\sqrt{qr} \end{pmatrix} \quad (92)$$

where  $q$  is the maximum transmission of linearly polarized light and  $r$  is the minimum transmission of linearly polarized light. Diattenuation is then given by  $(q-r)/(q+r)$  and the extinction ratio is given by  $q/r$ . Plugging this into Equation (41) and noting that  $\sin 2\theta \cos 2\theta$  is always zero at the angles used in the calibration (*i.e.*  $0^\circ$ ,  $45^\circ$ ,  $90^\circ$ , and  $135^\circ$ ), it is found that

$$\hat{m}_{01}(\theta_p) = \frac{(q-r)\cos 2\theta_p + m'_{01}((q+r)\cos^2 2\theta_p + 2\sqrt{qr}\sin^2 2\theta_p)}{q+r+(q-r)(m'_{01}\cos 2\theta_p + m'_{02}\sin 2\theta_p)} \quad (93)$$

and

$$\hat{m}_{02}(\theta_p) = \frac{(q-r)\sin 2\theta_p + m'_{02}((q+r)\sin^2 2\theta_p + 2\sqrt{qr}\cos^2 2\theta_p)}{q+r+(q-r)(m'_{01}\cos 2\theta_p + m'_{02}\sin 2\theta_p)} \quad (94)$$

Now, Equations (93) and (94) are plugged into Equation (45). This gives

$$L_m(\theta_p) = \begin{pmatrix} 1 + s_1 \frac{(q-r)\cos 2\theta_p + m'_{01}((q+r)\cos^2 2\theta_p + 2\sqrt{qr}\sin^2 2\theta_p)}{q+r+(q-r)(m'_{01}\cos 2\theta_p + m'_{02}\sin 2\theta_p)} \\ +s_2 \frac{(q-r)\sin 2\theta_p + m'_{02}((q+r)\sin^2 2\theta_p + 2\sqrt{qr}\cos^2 2\theta_p)}{q+r+(q-r)(m'_{01}\cos 2\theta_p + m'_{02}\sin 2\theta_p)} \end{pmatrix} L_s \quad (95)$$

where the only assumption made is that circular polarization in the scene is negligible and therefore  $s_3 = 0$ . This is a good assumption for passive remote sensing applications since the degree of circular polarization is typically very small [9].  $s_1$  and  $s_2$  then are solved for using Equations (55) and (56) and normalizing by  $s_0$ . This gives

$$s_{1m} = \frac{-(q-r)((m'_{01})^2 - 1)(q+r)s_1 + 2m'_{01}m'_{02}\sqrt{qr}s_2}{(q+r)^2 - m'_{01}{}^2(q-r)^2 + 4m'_{01}qrs_1 + 2m'_{02}q\sqrt{qr}s_2 + 2m'_{02}r\sqrt{qr}s_2} \quad (96)$$

and,

$$s_{2m} = \frac{-(q-r)((m'_{02})^2 - 1)(q+r)s_2 + 2m'_{01}m'_{02}\sqrt{qr}s_1}{(q+r)^2 - m'_{02}{}^2(q-r)^2 + 4m'_{02}qrs_2 + 2m'_{01}q\sqrt{qr}s_1 + 2m'_{01}r\sqrt{qr}s_1}. \quad (97)$$

While the form of  $s_{1m}$  and  $s_{2m}$  are complicated, it is interesting to see what happens when the Mueller matrix of the system (excluding the polarizer) is assumed to be close to or exactly the identity matrix. In the case of an identity system Mueller matrix,  $m'_{01}$  and  $m'_{02}$  are equal to zero. Using this in Equation (93),  $\hat{m}_{01}(\theta_p)$  reduces to

$$\hat{m}_{01}(\theta_p) = \frac{(q-r)\cos 2\theta_p}{q+r} = D\cos 2\theta_p \quad (98)$$

and

$$\hat{m}_{02}(\theta_p) = \frac{(q-r)\sin 2\theta_p}{q+r} = D\sin 2\theta_p. \quad (99)$$

Using this to solve for  $s_{1_m}$  and  $s_{2_m}$  gives

$$s_{1_m} = \frac{L_m(0) - L_m(90)}{L_m(0) + L_m(90)} = \frac{(1 + s_1 D)L_s - (1 - s_1 D)L_s}{(1 + s_1 D)L_s + (1 - s_1 D)L_s} = \frac{2s_1 DL_s}{2L_s} = s_1 D \quad (100)$$

and

$$s_{2_m} = \frac{L_m(45) - L_m(135)}{L_m(45) + L_m(135)} = \frac{(1 + s_2 D)L_s - (1 - s_2 D)L_s}{(1 + s_2 D)L_s + (1 - s_2 D)L_s} = \frac{2s_2 DL_s}{2L_s} = s_2 D. \quad (101)$$

This means that if the polarizer is non-ideal and the rest of the system has no effect on the polarimetric state of the light, then the measured Stokes vectors will simply be the true Stokes vectors multiplied by the diattenuation of the polarizer. This is a good approximation since the components of the system consist mainly of lenses and mirrors which have a small polarization effect. The one element still in question is the beam splitter which might have a more significant effect since it is more reflective and angled with respect to incident light.

### ***Simulation of Polarimetric Performance with non-ideal Polarizer***

It is hard to derive useful information from Equations (96) and (97), although it is interesting to note that if the polarizer is ideal, that is  $q = 1$  and  $r = 0$ , then  $s_{1_m} = s_1$  and  $s_{2_m} = s_2$  as expected. The easiest way to make sense of Equations (96) and (97) is to plug in realistic values for  $q$  and  $r$  since the extinction ratio of the polarizer is known, and to plug in a range of physically acceptable values for  $m'_{01}$  and  $m'_{02}$ . Then the result from various input polarization states can be simulated. These results can then be plotted and compared to actual data collected from the Hypercam. Since the band-averaged extinction ratio of the instrument polarizer is known to be approximately 400, let  $q = 0.8$

and  $r = 0.002$ . This gives an extinction ratio,  $q / r$  equal to 400. Possible values for  $m'_{01}$  and  $m'_{02}$  range from -1 to 1. For the first case, horizontally polarized light will be simulated, and therefore,  $s_1 = 1$  and  $s_2 = 0$  is input to the system. Doing this reduces Equations (96) and (97) to

$$s_{1_m} = 1.005 - \frac{0.010}{1.010 - m'_{01}} \quad (102)$$

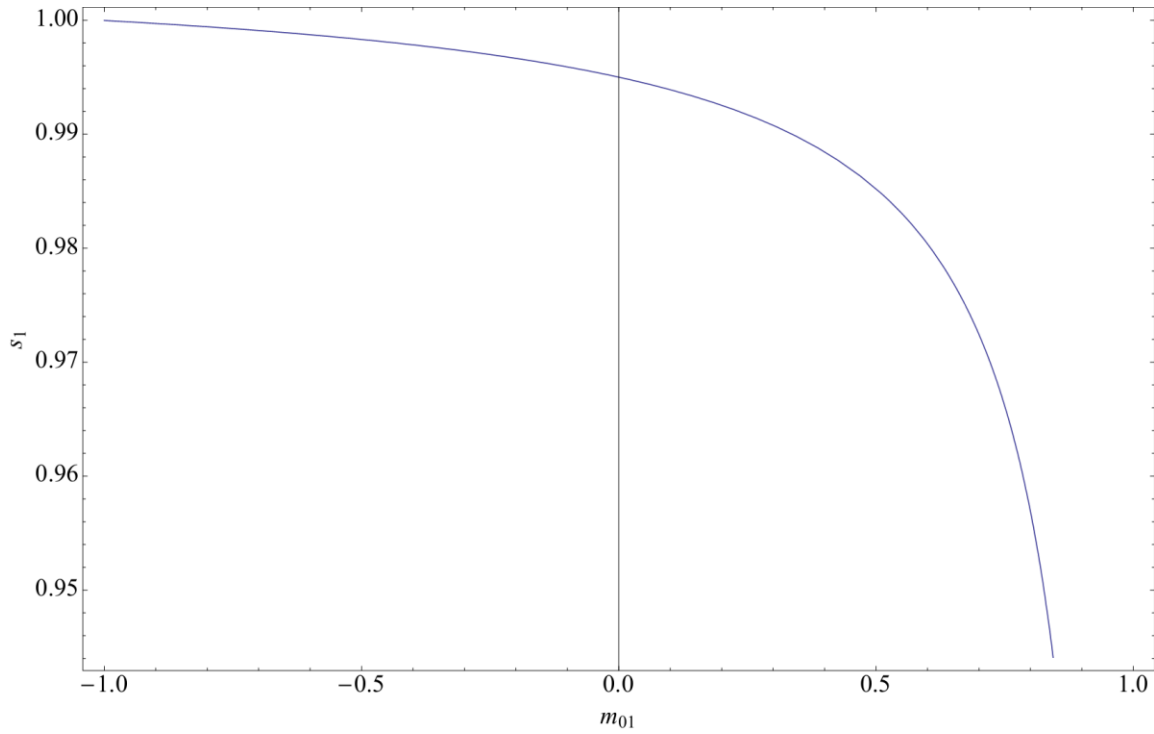
and

$$s_{2_m} = \frac{-0.995m'_{01}m'_{02}}{10.025 + m'_{01} - 9.925m'^2_{02}}. \quad (103)$$

Figure 49 shows a plot of  $s_{1_m}$  in which  $m'_{01}$  was allowed to range from -1 to 1. The plot confirms that for values of  $m'_{01}$  close to zero, the measured  $s_{1_m}$  is approximately the diattenuation of the instrument polarizer. A plot of the measured  $s_{2_m}$  is more difficult since it depends both on  $m'_{01}$  and  $m'_{02}$ . To gain a reasonable picture of how  $s_{2_m}$  varies with the values of  $m'_{01}$  and  $m'_{02}$ , a 3-D plot was generated with both  $m'_{01}$  and  $m'_{02}$  ranging from -0.7 to 0.7. As expected, the measured value of  $s_{2_m}$  is approximately zero when  $m'_{01}$  and  $m'_{02}$  are close to zero.

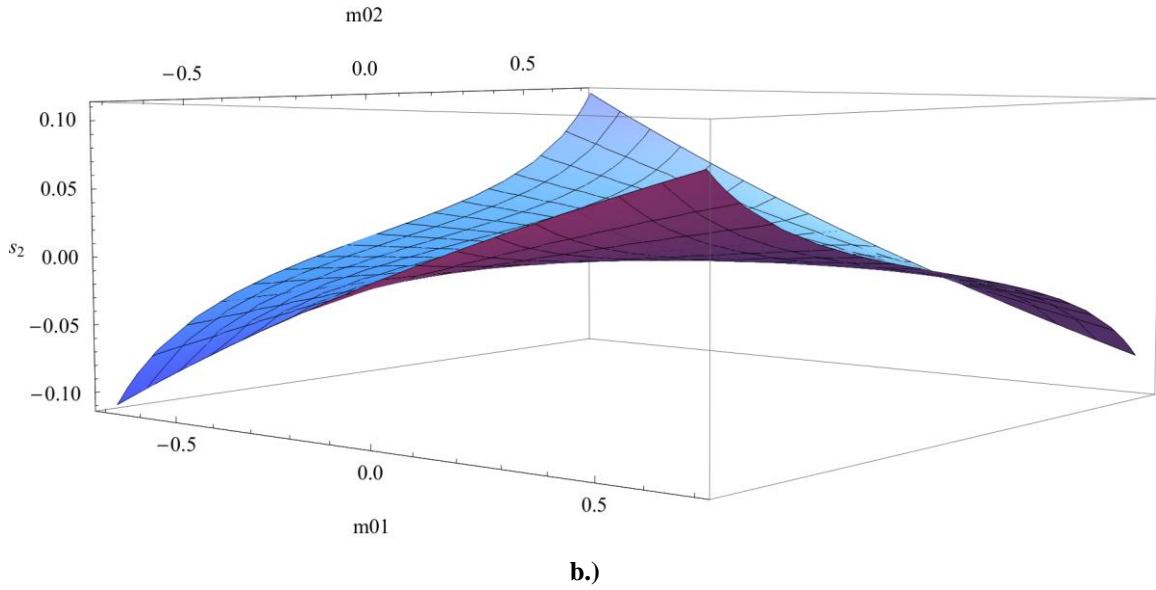
The derivations thus far in this section have used the Pickering Method for calculation of  $s_{1_m}$  and  $s_{2_m}$ . This was done to illustrate the math without having the equations become overly long and complicated. By doing so,  $s_{1_m}$  and  $s_{2_m}$  can never have a value greater than one. It is not hard, however, to extend the simulations to incorporate the modified Pickering Method. It will be necessary to do so since all of the

results reported in this thesis make use of this method and using this method allows the possibility of an  $s_{1_m}$  or  $s_{2_m}$  measurements greater than one due to the non-ideal effects of the polarizer. Figure 50 shows the results of the same simulation where an  $s_1 = 1$  and  $s_2 = 0$  is input into the system and the measured  $s_{1_m}$  and  $s_{2_m}$  are determined using the Modified Pickering method. In this case, the measured  $s_{1_m}$  also becomes a function of both  $m'_{01}$  and  $m'_{02}$  and so a 3-D plot is used and  $m'_{01}$  and  $m'_{02}$  are allowed to range from -0.7 to 0.7. Figure 50 (a) shows that the measured  $s_{1_m}$  has a weak dependence on  $m'_{02}$  and is roughly linearly dependent on  $m'_{01}$  for reasonable values of  $m'_{01}$  and  $m'_{02}$ . Figure 50 (b) shows that  $m'_{01}$  and  $m'_{02}$  both have a similar effect on the measured  $s_{2_m}$ , but for reasonable values of  $m'_{01}$  and  $m'_{02}$ ,  $s_{2_m}$  is approximately zero as expected.

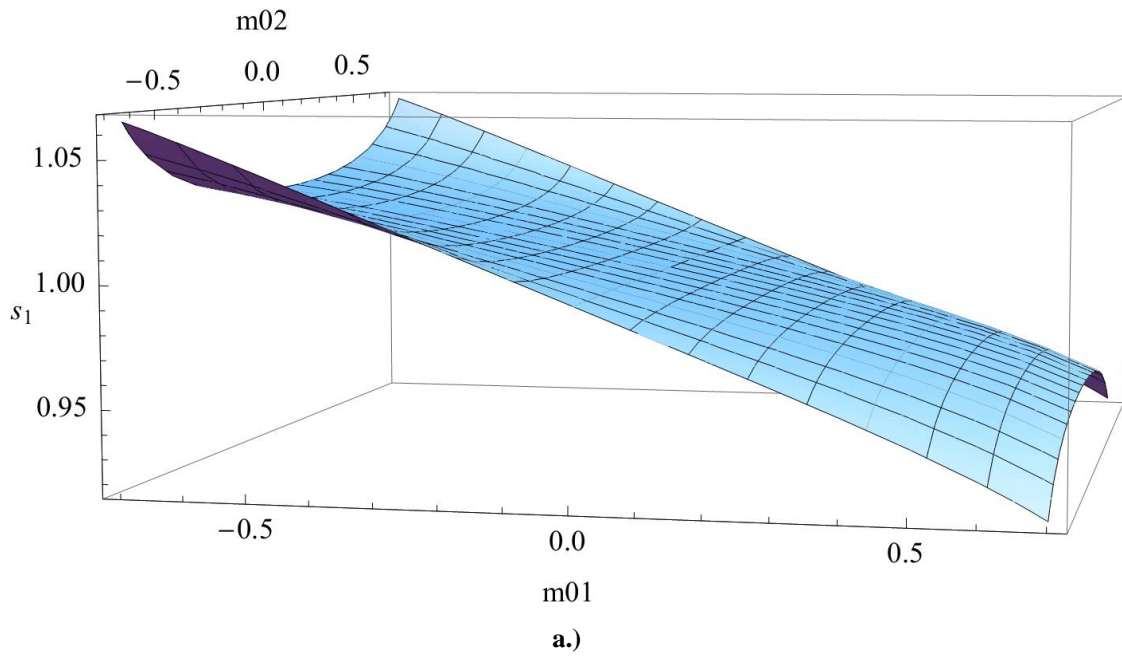


a.)





**Figure 49. a.) Simulation of the measured  $s_{1m}$  Stokes value when horizontally polarized light is incident on the system and  $m'_{01}$  is allowed to range from -1 to 1. b.) Simulation of the measured  $s_{2m}$  Stokes values when  $m'_{01}$  and  $m'_{02}$  are allowed to range from -0.7 to 0.7. The extinction ratio of the instrument polarizer is set to 400.**



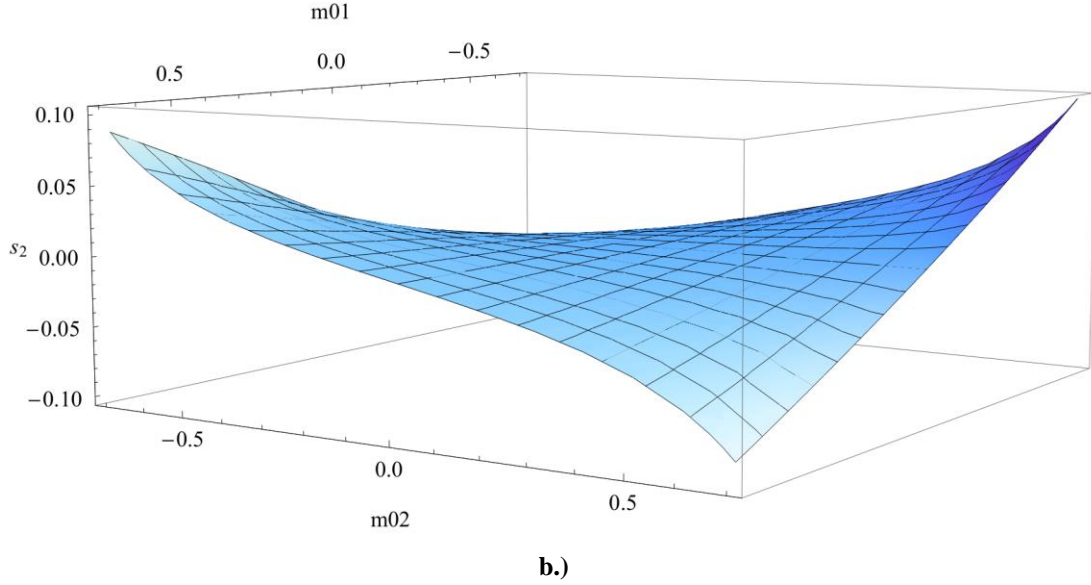


**Figure 50.** Same simulation for a.)  $s_{1m}$  and b.)  $s_{2m}$  as in Figure 49, except using the Modified Pickering method for calculation of the measured  $s_{1m}$  and  $s_{2m}$ . Notice that the value of the measured  $s_1$  can possibly exceed one using this method.

Another interesting simulation to run is for partially polarized light. If the instrument polarizer were ideal, the amount of  $s_2$  input would not affect the measured value for  $s_{1m}$  and vice-versa. Since the polarizer is not ideal, however, the two equations become coupled and the  $s_2$  input will affect the measured value for  $s_{1m}$  and vice-versa. The degree to which an  $s_2$  input affects the measured value of  $s_{1m}$  is dependent on the magnitude of  $m'_{01}$  and  $m'_{02}$ . Figure 51 shows the simulation for the measured value of  $s_{1m}$  when the input Stokes values of  $s_1$  and  $s_2$  are allowed to vary from 0 to 1. Figure 51 (a) is for  $m'_{01} = 0.05$  and  $m'_{02} = 0.05$  and Figure 51 (b) is for  $m'_{01} = 0.5$  and  $m'_{02} = 0.5$ . The results show that the input  $s_2$  has very little effect on the measured  $s_{1m}$  when  $m'_{01} = 0.05$ , but when  $m'_{01} = 0.5$  the input  $s_2$  does have a non-trivial effect on the measured  $s_{1m}$  value.

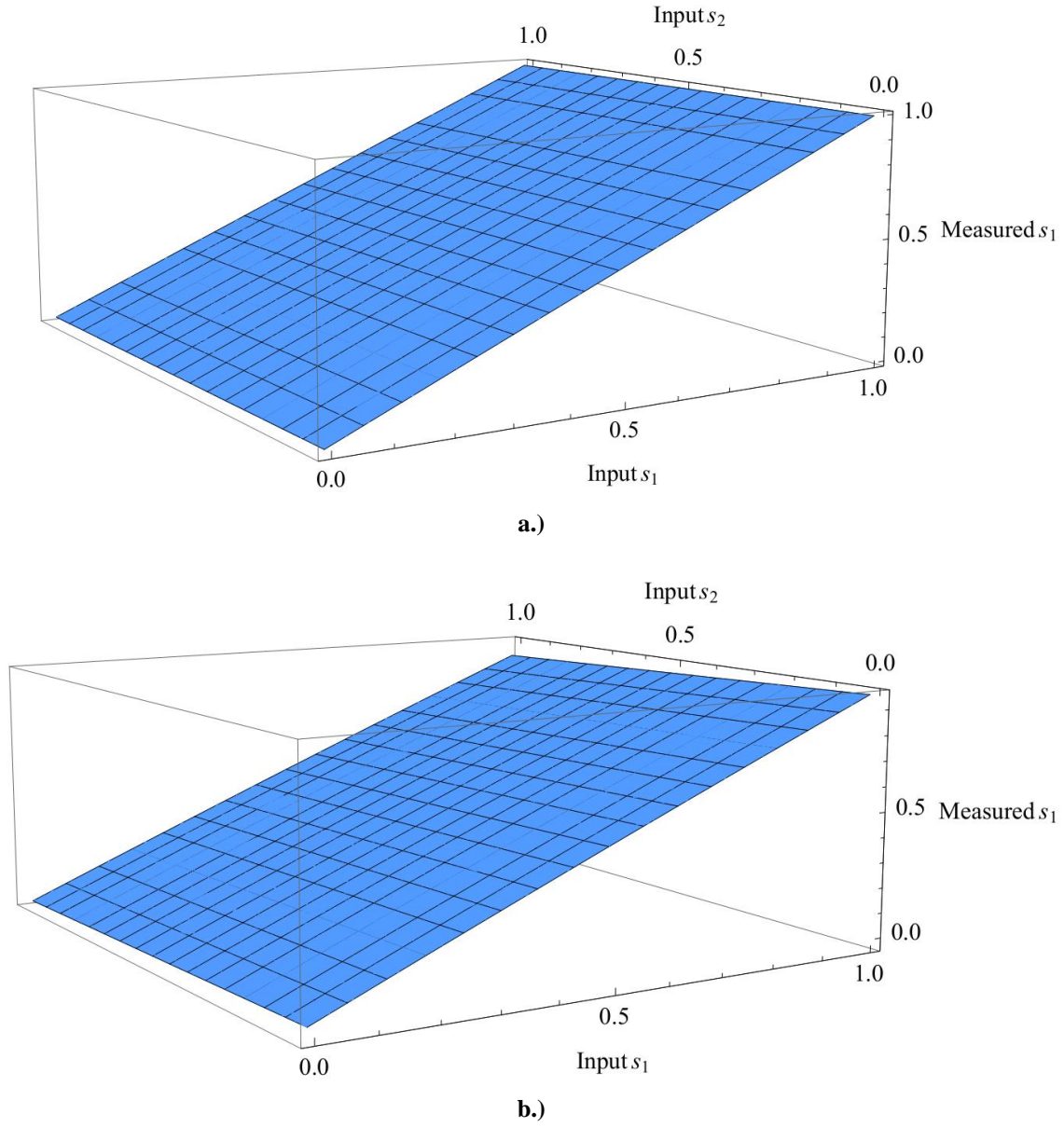


**Figure 51.** Measured value of  $s_{1m}$ , when the input Stokes values are allowed to range from 0 to 1 for a.)  $m'_{01}$  and  $m'_{02}$  equal to 0.05 and b.)  $m'_{01}$  and  $m'_{02}$  equal to 0.5.

Finally, one last simulation is provided to explore the dependence of the measured Stokes values on the extinction ratio of the instrument polarizer. To do this,  $q$  and  $r$  are allowed to vary from 0 to 1. The input Stokes parameters are  $s_1 = 1$  and  $s_2 = 0$  while  $m'_{01}$  and  $m'_{02}$  are both set to 0.05. Figure 52 shows the results. A value of  $q$  close to 1

and a value of  $r$  close to zero corresponds to a polarizer that is nearly ideal. As  $q$  moves away from 1 and  $r$  moves away from 0, the measured value of  $s_{1_m}$  decreases from the true input value.

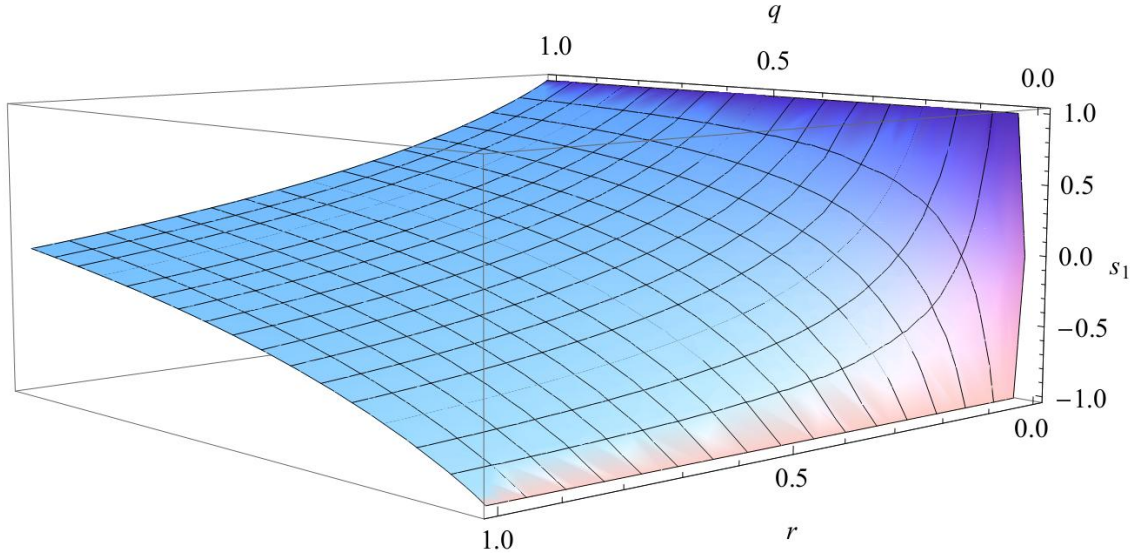


**Figure 52.** Shows the dependence of the measured  $s_{1_m}$  values on the extinction ratio of the instrument polarizer. The values of  $q$  and  $r$  are allowed to vary from 0 to 1. The input Stokes parameters are  $s_1 = 1$  and  $s_2 = 0$  and  $m_{01}'$  and  $m_{01}'$  are both equal to 0.05.

The simulations shown above provide insight into the effects of a non-ideal polarizer and a system Mueller matrix that is not assumed to be the identity matrix, on the quality of the measured Stokes parameters. According to Chipman, in the case where a system consists of weakly polarizing elements such as lens surfaces and mirror surfaces, the polarization properties are not zero due to the Fresnel equations, antireflection coatings, or mirrored surfaces, but the effects are often well below 5 percent [14]. For an  $m_{01}'$  and  $m_{02}'$  within  $\pm 5\%$  of zero and a horizontal input Stokes vector, the values for  $s_{1_m}$  range from 0.992 to 0.998 and  $s_{2_m}$  ranges from -0.0002 to 0.0002. These values correspond to a  $\pm 0.3\%$  error in  $s_{1_m}$  and a  $\pm 0.02\%$  error in  $s_{2_m}$ . In order to gain further

insight into what the  $m'_{01}$  and  $m'_{02}$  elements of the system Mueller matrix physically mean, the system itself is treated as a weak diattenuator which means that its Mueller matrix is given by Equation (92). Since the off-axis elements in Equation (92) are assumed to be small, the first-order Taylor series expansion can be taken. After normalizing the Mueller matrix, this gives

$$\mathbf{M}' \approx \begin{pmatrix} 1 & D'_H & D'_{45} & D'_R \\ D'_H & 1 & 0 & 0 \\ D'_{45} & 0 & 1 & 0 \\ D'_R & 0 & 0 & 1 \end{pmatrix} \quad (104)$$

where  $m'_{01} \approx D'_H$  determines the transmission of a horizontal/vertical input state and  $m'_{02} \approx D'_{45}$  determines the transmission of a  $45^\circ/135^\circ$  input state. In other words, the  $m'_{01}$  and  $m'_{02}$  elements determine the diattenuation of the HSI instrument itself.

### ***Determination of the HSI System Diattenuation***

Now, using the actual measured response of the system for the 12 different input Stokes vectors, the system model can be used to solve for the  $m'_{01}$  and  $m'_{02}$  elements of the HSI system's Mueller matrix. This will then allow for the calculation of the HSI system's diattenuation. As a reminder, when referring to the HSI system, the polarizer is being excluded. Equations (96) and (97) are re-stated here for reference:

$$s_{1m} = \frac{-(q-r)\left((m'^2_{01}-1)(q+r)s_1 + 2m'_{01}m'_{02}\sqrt{qr}s_2\right)}{(q+r)^2 - m'^2_{01}(q-r)^2 + 4m'_{01}qrs_1 + 2m'_{02}q\sqrt{qr}s_2 + 2m'_{02}r\sqrt{qr}s_2}$$

$$s_{2m} = \frac{-(q-r)\left((m'^2_{02}-1)(q+r)s_2 + 2m'_{01}m'_{02}\sqrt{qr}s_1\right)}{(q+r)^2 - m'^2_{02}(q-r)^2 + 4m'_{02}qrs_2 + 2m'_{01}q\sqrt{qr}s_1 + 2m'_{01}r\sqrt{qr}s_1}$$

where  $s_{1_m}$  and  $s_{2_m}$  are the measured Stokes parameters for a given input  $s_1$  and  $s_2$ . Also recall that these equations were derived using the Pickering method whereas the same equations derived using the Modified Pickering method are similar but longer and more complicated. The results described in this section use the Modified Pickering method equations. To find the best solution for  $m'_{01}$  and  $m'_{02}$ , the Nelder-Mead simplex direct search algorithm was implemented to minimize the error between the true measured values for  $s_{1_m}$  and  $s_{2_m}$  and the values generated with above equations while allowing  $m'_{01}$  and  $m'_{02}$  to range from -1 to 1. The results give a value of  $m'_{01} = 0.14$  and  $m'_{02} = -0.41$ . According to Chipman [14], a diattenuation parameter set,  $d$ , can be defined for linearly polarized light as

$$d = \frac{\{m_{01} \ m_{02}\}}{m_{00}} = \{m'_{01} \ m'_{02}\} = \{d_H \ d_{45}\}, \quad (105)$$

which characterizes the dependence of the transmission on the incident polarization state. The linear diattenuation of any Mueller matrix is then given by

$$D(\mathbf{M}) = \frac{\tau_{\max} - \tau_{\min}}{\tau_{\max} + \tau_{\min}} = \sqrt{m'^2_{01} + m'^2_{02}}. \quad (106)$$

Utilizing this to determine the linear diattenuation of the HSI system based on the calculated values of  $m'_{01}$  and  $m'_{02}$  gives

$$D(\mathbf{M}_{HSI}) = \sqrt{(0.14)^2 + (-0.41)^2} = 0.43. \quad (107)$$

The extinction ratio of the HSI system can also be determined with

$$ER = \frac{1+D}{1-D} = \frac{1+0.43}{1-0.43} = 2.51. \quad (108)$$

To visualize how well the calculated values of  $s_{1m}$  and  $s_{2m}$  match the measured values,

Figure 53 plots them together.

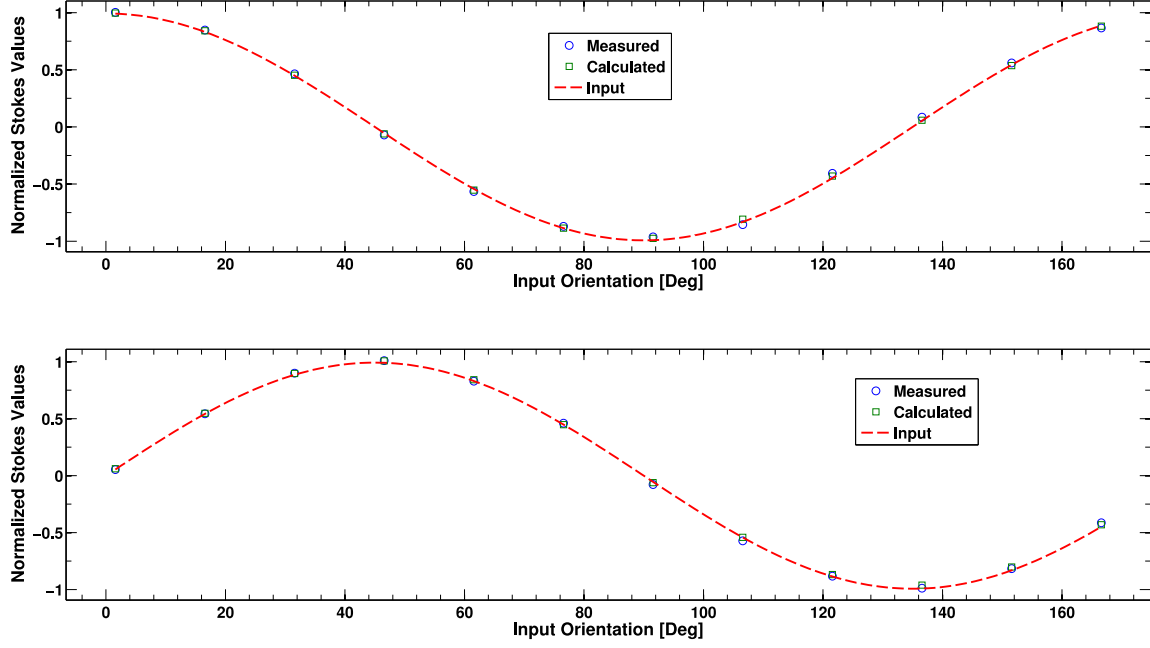


**Figure 53.** The measured values of  $s_{1m}$  and  $s_{2m}$  for the 12 input Stokes vectors are plotted with circles and the calculated values for  $s_{1m}$  and  $s_{2m}$  are plotted with squares. The input curve is plotted as a dashed line.

## VI. Conclusions

Polarimetric-hyperspectral remote sensing is a promising field that brings two traditionally independent modalities together to enhance scene characterization capabilities. The Telops P-HSI instrument combines these technologies in a way that has never been done before and provides a combined imaging and spectral capability that is considered state-of-the art. The Defense Threat Reduction Agency (DTRA) funded research at AFIT to leverage this capability to better inform radiation transport models that will allow for more effective location of ionizing radiation sources within the scene.

The desire for highly accurate data requires careful calibration of the instrument. In this thesis, a mathematical calibration framework was developed that links standard Fourier transform spectrometer (FTS) calibration with standard polarimetric calibration in a simple, straightforward manner. Building this framework was key for two reasons. First, it was essential for ensuring the calibration methodology was sound and it provided a framework for understanding the influence of various instrument parameters (both ideal and non-ideal) on ultimate calibration performance. Second, this development makes it easy for both FTS and polarimetric experts to understand, and paves the way for use of this method for similar instruments in the future.

Due to the complexities of the system and operation in LWIR waveband, three different types of calibration are required. These are: radiometric calibration, off-axis spectral calibration, and polarimetric calibration. As a result of this thesis, all three calibrations are now successfully accomplished. This means that highly accurate radiometric, spectral, and polarimetric data can be generated with the Telops instrument.



This will enable more accurate scene characterization, which will provide more accurate information to the radiation models developed under DTRA sponsorship.

While all three types of calibration were demonstrated in this thesis, the primary focus was on polarimetric calibration. This was the first time the Telops instrument has been used with the additional polarimetric capability, and therefore, this is the first time polarimetric calibration has been performed on the instrument. The polarimetric calibration effort showed that by taking calibration blackbody data at each of the four polarizer angles, and solving for the spectro-polarimetric gain and offset at each angle, the full polarimetric calibration is achieved with the only assumption being that the polarizer is ideal, *i.e.*, it has a diattenuation of one. The polarimetric calibration was then expanded to include the more general case of a non-ideal polarizer and the methodology necessary to correct for and quantify the non-ideality was developed. This involved experimental determination of the system matrix, data reduction matrix, and Mueller deviation matrix for each pixel at each waveband.

The polarimetric calibration was then performed, first assuming an ideal polarizer, and then making the additional correction for a non-ideal polarizer. The additional correction for a non-ideal polarizer was difficult considering the fact that the diattenuation of the instrument polarizer is approximately 0.995, and therefore, the necessary correction is only roughly 0.5%. The results showed that the correction did improve the error by 0.56% or less on average. The results also showed, however, that there was some residual error left over after the correction and that the correction is ultimately limited by the noise in the measurements, the non-linearity of the detector, and the accuracy of the experimental setup. Each of these limitations were discussed and the

noise statistics of the measurements were explored. Since the correction is required on a pixel-by-pixel and band-by-band basis, the noise was determined on a pixel-by-pixel and band-by-band basis. It was shown that some of the residual error in the polarized data can be attributed to noise in the measurements. It was also shown that a primary source of the residual error in the data was likely due to the thermal stability of the 6-inch blackbody source. Additionally, it was shown that there is currently a fundamental limitation on all data sets which is caused by the non-linearity of the detector. This causes a checker board pattern on all images with low signal levels. This same checker board pattern shows up in the Mueller deviation matrix which represents the non-idealities of the system. Determining the exact cause and proper correction for this checker board pattern is a subject of on-going research.

In the process of deriving the full spectro-polarimetric calibration methodology for the instrument, a polarimetric system model was developed. This system model maps an input scene Stokes vector to the Stokes vector that is actually measured by the instrument as a function of the extinction ratio of the instrument polarizer, the diattenuation of the HSI system (not including the polarizer), and the input stokes parameters. This allowed the system performance to be simulated as a function of the polarimetric system parameters and gave insight into how each parameter affects the accuracy of measured data. It was shown that in the case of a small HSI system diattenuation, the measured data was accurate and the primary limitation was imposed by the polarizer extinction ratio. A large system diattenuation, however, imposed error on the measured data which must be corrected with the calibration methods described in this thesis. The actual diattenuation of the HSI system (not including the polarizer) was then

determined using the system model and the measured data from the experiment. The diattenuation of the system was found to be 0.43 which corresponds to an extinction ratio of 2.51. This is small compared with the polarizer's extinction ratio of 400; however, it must be calibrated out to achieve the most accurate data from the instrument. This thesis demonstrated the methodology required to calibrate this effect out.

In addition to calibration, several figures of merit were determined for the system. These included the NESR and NESDoLP for both unpolarized and polarized light. For unpolarized light, the NESR was reported at four instrument polarizer angles ( $0^\circ$ ,  $45^\circ$ ,  $90^\circ$ ,  $135^\circ$ ). The results showed that the NESR at  $45^\circ$  and  $135^\circ$  were equal across the band, whereas the NESR for  $0^\circ$  was lower and the NESR for  $90^\circ$  was higher. The values reported are for a spectral resolution of  $16 \text{ cm}^{-1}$ , viewing a  $55^\circ\text{C}$  blackbody source with a  $200 \mu\text{s}$  integration time. The band-averaged values were  $30.6 \text{ nW}/(\text{cm}^2\text{sr}) \text{ cm}^{-1}$ ,  $33.6 \text{ nW}/(\text{cm}^2\text{sr}) \text{ cm}^{-1}$ ,  $33.6 \text{ nW}/(\text{cm}^2\text{sr}) \text{ cm}^{-1}$ , and  $36.9 \text{ nW}/(\text{cm}^2\text{sr}) \text{ cm}^{-1}$  for the  $0^\circ$ ,  $45^\circ$ ,  $135^\circ$ , and  $90^\circ$  measurements respectively. This result verified that the system was operating within the specifications provided by the manufacturer. The fact that the NESR for the  $0^\circ$  and  $90^\circ$  measurements were split while the NESR for the  $45^\circ$  and  $135^\circ$  were equal is indicative of the diattenuation of the HSI system after the light passes through the polarizer. The band-averaged NESDoLP for the unpolarized source was 0.39%. The actual calculated DoLP for the unpolarized source was 0.51%. This indicates that a residual error or bias of 0.12% remained in the data after calibration. This residual error was attributed to either thermal drift in the reference source or detector non-linearity. The band-averaged NESR for the polarized source was  $29.8 \text{ nW}/(\text{cm}^2\text{sr}) \text{ cm}^{-1}$ ,  $31.8 \text{ nW}/(\text{cm}^2\text{sr})$ ,  $39.1 \text{ nW}/(\text{cm}^2\text{sr})$ , and  $41.0 \text{ nW}/(\text{cm}^2\text{sr})$  for the  $45^\circ$ ,  $90^\circ$ ,  $0^\circ$ , and  $135^\circ$

measurements respectively. This again was within the specifications provided by the manufacturer. The measured DoLP for the polarized source was 100.48% before correction for the non-ideal polarizer and 99.92% after correction. The DoLP above 100% was attributed to noise in the measurements as well as the possible thermal drift of the reference blackbody source. In this case, the correction improved the accuracy of the DoLP measurement by 0.56%, but left a residual error of 0.62%.

Ultimately, this thesis provides solid evidence that the Telops instrument is performing as expected from a polarimetric standpoint and this is something that can be presented to the polarimetric community for critique. This will then allow future researchers to have confidence in their results while focusing more on the applications of the data such as material identification, target detection, anomaly detection, disturbed earth detection, and 3-D scene reconstruction. All of which are important capabilities that the DoD and IC wish to develop and improve upon. With a few simple improvements to the experimental setup, the residual errors reported in this thesis should be reduced to negligible values. The next section discusses recommendations to improve the setup for future calibration efforts in order to achieve the best results.

## **Future Recommendations**

Three iterations of the calibration experiment were completed, each one improving results over its predecessor. The final experiment was done in a way that minimized errors due to the setup as much as possible within the limitations of the available equipment at the time. After a thorough analysis of the data and a better understanding of the sources of residual error, there are still several measures that can be

taken to improve the accuracy of the calibration. Since the error introduced by assuming an ideal instrument polarizer is so small, the experimental setup must achieve extremely high accuracy in order to provide the additional correction for the non-ideal nature of the polarizer. Here are several recommendations for achieving higher accuracy with the experimental setup and thus better results from the calibration.

First, it is necessary to know the input Stokes vectors with very high accuracy. If a linear wire-grid polarizer is used as in the above experiment, this means careful characterization of the spectral diattenuation of the polarizer and high confidence that there are no blemishes in the surface of the polarizer that affect it spatially. For this thesis, the manufacturer's data sheet was used for determination of the spectral diattenuation; however, this characterization could be done experimentally, right before the calibration. Additionally, use of an accurate, motor driven rotation stage would be useful for decreasing the uncertainty in the external polarizer orientation and increasing the accuracy of the input Stokes vectors.

Second, the 6-inch blackbody should be eliminated from the setup due to its poor thermal stability performance ( $\pm 0.5$  °C). This is an unacceptable thermal drift, which is likely the primary source of the residual error seen in the data. The 6-inch blackbody was used to ensure that the entire FOV of the polarizer was filled by the blackbody, however, with careful setup procedures, the 6-inch blackbody could be replaced with a more stable 2-inch blackbody ( $\pm 0.003$  °C).

Third, to improve the noise statistics, it would have been good to increase the difference between the hot and cold data sets. That way, when they are differenced, the SNR is better. This combined with a larger number of frame averages would improve the

calibration. Since the system matrix was shown to be flat spectrally, a lower spectral resolution could be used to help increase SNR as well.

Fourth, the external polarizer could be moved much closer to the Telops instrument. In this thesis, the external polarizer was placed at a range that would allow the polarizer to be in focus. This isn't necessary however, and by moving it closer to the instrument, there is a smaller possibility of the target blackbodies causing thermal effects on the external polarizer. Moving it closer would also allow more pixels on the FPA to be calibrated at one time.

Finally, a method should be developed to perform the polarimetric calibration on the entire FPA. This capability is limited by the small extent of the external polarizer, which prevents it from filling the entire FOV of the system. One suggestion would be to perform the calibration on one region of the FPA at a time until the entire FPA is mapped. The system matrix is not expected vary much in the spatial dimension and so it should not be hard to map the entire FPA with this method.

## References

- [1] D. Manolakis, *Detection Algorithms for Hyperspectral Imaging Applications*. Report Number ESC-TR-2001-044. MIT Lincoln Laboratory, Lexington, 2002.
- [2] M. T. Eismann, "Fourier Transform Spectrometer Design and Analysis," in *Hyperspectral Remote Sensing*. Bellingham: SPIE Press, 2012, pp. 363-393.
- [3] V. Farley, A. Vallieres, M. Chamberland, A. Villemaire and J.-F. Legault, "Performance of the FIRST, a Longwave Infrared Hyperspectral Imaging Sensor," *Proc. SPIE 6398, Optically Based Biological and Chemical Detection for Defence III*. 63980T, Stockholm, 2006.
- [4] M. C. Abrams, J. W. Brault and S. P. Davis, *Fourier Transform Spectrometry*, San Diego: Academic Press, 2001.
- [5] O. Sandus, "A Review of Emission Polarization," *Applied Optics*, vol. 4, no. 12, pp. 1634-1642, 1965.
- [6] D. A. LeMaster and M. T. Eismann, "Passive Polarimetric Imaging (in press)," in *Multi-dimensional Imaging*, B. Javidi, E. Tajahuerce and P. Andres, Eds., John Wiley & Sons, Ltd.
- [7] M. Felton, K. P. Gurton, J. L. Pezzaniti, D. B. Chenault and L. E. Roth, "Measured comparison of the crossover periods for mid- and long-wave IR (MWIR and LWIR) polarimetric and conventional thermal imagery," *Optics Express*, vol. 18, no. 15, pp. 15704-15713, 2010.
- [8] G. G. Stokes, "On the composition and resolution of streams of polarized light from different sources," *Transactions of the Cambridge Philosophical Society (reprinted in Mathematical and Physical Papers, Vol. III, Cambridge University Press, Cambridge, 1901)*, vol. 9, pp. 399-416, 1852.
- [9] J. R. Schott, *Fundamentals of Polarimetric Remote Sensing*, Bellingham: SPIE Press, 2009.

- [10] H. Mueller, "Memorandum on the polarization of optics of the photo-elastic shutter.," *Report Number 2 of the OSRD project OEMSr 576*.
- [11] E. Collett, *Polarized Light: Fundamentals and Applications*, New York: Marcel Dekker, Inc., 1993.
- [12] D. H. Goldstein, *Polarized Light*, New York: Marcel Dekker, Inc., 2003.
- [13] R. A. Chipman, "Polarimetry," in *Handbook of Optics*, vol. 2, New York: McGraw-Hill, 1995.
- [14] R. A. Chipman, "Mueller Matrices," in *Handbook of Optics*, vol. 2, New York: McGraw-Hill, 1995.
- [15] E. Hecht, *Optics*, 4th ed., San Francisco: Addison-Wesley, 2002.
- [16] R. Walraven, "Polarization imagery," *Optical Engineering*, vol. 20, no. 1, pp. 14-18, 1981.
- [17] J. E. Solomon, "Polarization imaging," *Applied Optics*, vol. 20, no. 9, pp. 1537-1544, 1981.
- [18] J. R. Schott, *Remote Sensing: The Image Chain Approach*, 2nd ed., New York: Oxford University Press, 2007.
- [19] M. T. Eismann, "Spectrometer Calibration," in *Hyperspectral Remote Sensing*, Bellingham: SPIE Press, 2012, pp. 417-449.
- [20] C. M. Persons, M. W. Jones, C. A. Farlow, D. L. Morell, M. G. Gulley and K. D. Spradley, "A proposed standard method for polarimetric calibration and calibration verification," *Proc. SPIE 6682, Polarization Science and Remote Sensing III*. 66820K, San Diego, 2007.
- [21] M. W. Kudenov, J. L. Pezzaniti and G. R. Gerhard, "Microbolometer-infrared imaging Stokes polarimeter," *Optical Engineering*, vol. 48(6), no. 063201, 2009.
- [22] M. H. Smith, M. A. Miller, R. V. Blumer, M. A. Stevens, D. M. Teale and J. D. Howe, "Infrared Stokes polarimeter calibration," *Proc. SPIE 4133, Polarization*



*Analysis, Measurement, and Remote Sensing III.* pp. 55-64, San Diego, 2000.

- [23] R. V. Blumer, M. A. Miller, J. D. Howe and M. A. Stevens, "LWIR Polarimeter Calibration," *Proc. SPIE 4481, Polarization Analysis, Measurement, and Remote Sensing IV.* pp. 37-49, San Diego, 2002.
- [24] D. L. Bowers, J. K. Boger, L. D. Wellems, W. T. Black, S. E. Ortega, B. M. Ratliff, M. P. Fetrow, J. E. Hubbs and J. S. Tyo, "Evaluation and Display of Polarimetric Image Data Using Long-Wave Cooled Microgrid Focal Plane Arrays," *Proc. SPIE 6240, Polarization Measurement, Analysis, and Remote Sensing VII.* 62400F, San Diego, 2006.
- [25] D. L. Bowers, J. K. Boger, L. D. Wellems, S. E. Ortega, M. P. Fetrow, J. E. Hubbs, W. T. Black, B. M. Ratliff and J. S. Tyo, "Unpolarized calibration and nonuniformity correction for long-wave infrared microgrid imaging polarimeters," *Optical Engineering*, vol. 47(4), no. 046403, 2008.
- [26] J. E. Hubbs, M. E. Gramer, D. Maestas-Jepson, G. A. Dole, M. Fetrow, D. Bowers and J. Boger, "Measurement of the radiometric and polarization characteristics of a microgrid polarizer infrared focal plane array," *Proc. SPIE 6295, Infrared Detectors and Focal Plane Arrays VIII.* 62950C, San Diego, 2006.
- [27] M. W. Jones and C. M. Persons, "Performance Predictions for Micro-Polarizer Array Imaging Polarimeters," *Proc. SPIE 6682, Polarization Science and Remote Sensing III.* 668208, San Diego, 2007.
- [28] E. L. Dereniak and G. D. Boreman, *Infrared Detectors and Systems*, New York: John Wiley & Sons, INC., 1996.
- [29] J. K. Boger, J. S. Tyo, B. M. Ratliff, M. P. Fetrow, W. T. Black and R. Kumar, "Modeling Precision and Accuracy of a LWIR Microgrid Array Imaging Polarimeter," *Proc. SPIE 5888, Polarization Science and Remote Sensing II.* 58880U, San Diego, 2005.
- [30] B. M. Ratliff, Kumar R, J. S. Tyo and M. M. Hayat, "Combatting infrared focal plane array nonuniformity noise in imaging polarimeters," *Proc. SPIE 5888, Polarization Science and Remote Sensing II.* 58880J, San Diego, 2005.

- [31] B. M. Ratliff, M. P. Fetrow, J. S. Tyo and J. K. Boger, "The effect of fixed pattern noise on imaging stokes vector microgrid polarimeters," *Proc. of 2000 CALCON Technical Conference*, Logan, 2005.

<b>REPORT DOCUMENTATION PAGE</b>				Form Approved OMB No. 074-0188	
<p>The public reporting burden for this collection of information is estimated to average 1 hour per response, including the time for reviewing instructions, searching existing data sources, gathering and maintaining the data needed, and completing and reviewing the collection of information. Send comments regarding this burden estimate or any other aspect of the collection of information, including suggestions for reducing this burden to Department of Defense, Washington Headquarters Services, Directorate for Information Operations and Reports (0704-0188), 1215 Jefferson Davis Highway, Suite 1204, Arlington, VA 22202-4302. Respondents should be aware that notwithstanding any other provision of law, no person shall be subject to a penalty for failing to comply with a collection of information if it does not display a currently valid OMB control number.</p> <p><b>PLEASE DO NOT RETURN YOUR FORM TO THE ABOVE ADDRESS.</b></p>					
<b>1. REPORT DATE (DD-MM-YYYY)</b> 28-03-2014		<b>2. REPORT TYPE</b> Master's Thesis		<b>3. DATES COVERED (From – To)</b> Sep 2012 - Mar 2014	
<b>4. TITLE AND SUBTITLE</b>  Polarimetric Calibration and Characterization of the Telops Field Portable Polarimetric-Hyperspectral Imager				<b>5a. CONTRACT NUMBER</b>	
				<b>5b. GRANT NUMBER</b> 2437-M (Polarimetric HSI)	
				<b>5c. PROGRAM ELEMENT NUMBER</b>	
<b>6. AUTHOR(S)</b>  Holder, Joel G, Captain, USAF				<b>5d. PROJECT NUMBER</b>	
				<b>5e. TASK NUMBER</b>	
				<b>5f. WORK UNIT NUMBER</b>	
<b>7. PERFORMING ORGANIZATION NAMES(S) AND ADDRESS(S)</b> Air Force Institute of Technology Graduate School of Engineering and Management (AFIT/EN) 2950 Hobson Way WPAFB OH 45433-7765				<b>8. PERFORMING ORGANIZATION REPORT NUMBER</b>  AFIT-ENP-14-M-14	
<b>9. SPONSORING/MONITORING AGENCY NAME(S) AND ADDRESS(ES)</b> Defense Threat Reduction Agency Dave Petersen, <a href="mailto:david.petersen@dtra.mil">david.petersen@dtra.mil</a> , (703) 767-3164 8725 John J. Kingman Road Fort Belvoir, VA 22060				<b>10. SPONSOR/MONITOR'S ACRONYM(S)</b> DTRA	
				<b>11. SPONSOR/MONITOR'S REPORT NUMBER(S)</b>	
<b>12. DISTRIBUTION/AVAILABILITY STATEMENT</b> DISTRIBUTION STATEMENT A: APPROVED FOR PUBLIC RELEASE; DISTRIBUTION UNLIMITED.					
<b>13. SUPPLEMENTARY NOTES</b> This material is declared a work of the U.S. Government and is not subject to copyright protection in the United States.					
<b>14. ABSTRACT</b> The Telops polarimetric-hyperspectral imager combines polarimetric and hyperspectral technologies to enable enhanced scene characterization. The Defense Threat Reduction Agency funded research at AFIT to leverage this capability to provide more accurate scene information to radiation transport models that will allow for more effective location of radiation sources within a region of interest. To support the objectives of the DTRA effort, there is a requirement for highly accurate radiometric, polarimetric, and spectral data on a pixel-by-pixel basis. The complex nature of the Telops instrument combined with working in the thermal IR waveband makes achieving this accuracy a challenge. This thesis develops a calibration methodology that enables high data accuracy in all three domains. In the process, a mathematical calibration framework was developed that links standard Fourier transform spectrometer (FTS) calibration with standard polarimetric calibration in a straightforward manner. This provided a framework for understanding the influence of various instrument parameters (both ideal and non-ideal) on ultimate calibration performance. The framework developed is utilized to quantify the non-idealities of the system and to characterize the performance of the spectro-polarimetric calibration. Additionally, fundamental performance limits are characterized including the noise equivalent spectral radiance and noise equivalent degree of linear polarization of the system.					
<b>15. SUBJECT TERMS</b> Remote sensing, calibration, polarimetry, hyperspectral imaging, polarimetric calibration, radiometry, spectral calibration, radiometric calibration, material identification					
<b>16. SECURITY CLASSIFICATION OF:</b>			<b>17. LIMITATION OF ABSTRACT</b>  UU	<b>18. NUMBER OF PAGES</b>  139	<b>19a. NAME OF RESPONSIBLE PERSON</b> Dr. Kevin Gross, AFIT/ENP
<b>REPORT</b> U	<b>ABSTRACT</b> U	<b>c. THIS PAGE</b> U			<b>19b. TELEPHONE NUMBER (Include area code)</b> (937)-255-3636 x4558, kevin.gross@afit.edu